INTERACTIONS BETWEEN MICROORGANISMS AND CLAY-RICH SEDIMENTS DURING EARLY BURIAL AND DIAGENESIS

A Dissertation

by

NICHOLAS TANNER MILLS

Submitted to the Graduate and Professional School of
Texas A&M University
in partial fulfillment of the requirements for the degree of

DOCTOR OF PHILOSOPHY

Chair of Committee,	Julia Reece
Committee Members,	Michael Tice
	Franco Marcantonio
	Jason Sylvan
Head of Department,	Julie Newman

December 2021

Major Subject: Geology

ABSTRACT

The purpose of this dissertation was to understand interactions between microorganisms and fine-grained sediments during the early stages of burial and diagenesis. Despite the abundance of research on sediment diagenesis, there remain many overlooked and understudied relationships between microorganisms and sediments. We investigated interactions between (1) clay minerals and sediment pore fluids, (2) microorganisms and fine-grained sediments, and (3) microorganisms, clay transformations, and carbonate precipitation. We employed an integrated program of numerical modeling as well as experimental and analytical techniques using natural marine sediments and iron-reducing bacteria to study these interactions. We found that clay minerals modulate sediment pore fluid pH and carbonate mineral saturation, that the effectiveness of microorganisms at altering permeability and compression properties is dependent on burial depth (porosity as a function of vertical effective stress) and the grain size, pore and pore throat size, and specific surface area of a sediment, and that microorganisms can induce clay mineral transformations (smectite to illite) and carbonate precipitation during the early stages of diagenesis. These results are of importance for carbon and elemental cycling throughout Earth history, fluid flow and overpressure generation in the subsurface, friction properties on faults, and oil and gas exploration.

DEDICATION

To Chloe.

ACKNOWLEDGEMENTS

First, I would like to thank my mentor, Julia Reece, for her help and patience over the years. She taught me to think critically and ultimately how to be a scientist. I will be forever grateful for her guidance. Thanks go to Mike Tice for his countless contributions to this work and for answering my many, many questions. I thank Jason Sylvan for his assistance in guiding this research and for allowing me to use his lab. I appreciate Franco Marcantonio for his willingness to assist in this research and for always making me feel welcome in the department.

A special thanks go out to my office mates and fellow graduate students Ryan Elmore, Autumn Eakin, and Wyatt Scott for their support, feedback, and discussions. I also thank Melanie Bowen, Lucky Marchelino, Jesse Yeon, Tate Ryan, Gunner Boler, and Andrew Robertson for their help working in the lab.

I'm grateful for all of the analytical help I have received from the greater Texas A&M community. I thank Dr. Youjun Deng, Bidemi Fashina, and Juan-Carlos Laya for their help with X-ray diffraction analysis, Dr. Stanislav Vitha for his help with scanning electron microscopy work in the Microscopy and Imaging Center, Hamidreza Samouei for his help with titrations, Andrew Mott for his help with the electron microprobe analyses in the Material Characterization facility, Charles Holmes for their help with cell counts, and Mike Tice and Marion Nachon for their help with μXRF analyses.

I am especially thankful for my family and all the support they have given me. Thank you to my parents and in-laws for continually encouraging me during my time in

graduate school. Thanks to Christopher and Jane for reminding me daily of what is most important in life. Finally, thank you to my beautiful wife, Chloe, for her support, patience, and love.

CONTRIBUTORS AND FUNDING SOURCES

Contributors

This work was supervised by a dissertation committee consisting of Professors Julia Reece (committee chair), Mike Tice, and Franco Marcantonio from the Department of Geology and Geophysics and Professor Jason Sylvan from the Department of Oceanography.

The work for this dissertation was completed by Tanner Mills under the advisement of Professors Julia Reece and Mike Tice from the Department of Geology and Geophysics and Professor Jason Sylvan from the Department of Oceanography.

Funding Sources

The sediment samples used in this research were provided by the International Ocean Discovery Program (IODP). Funding for this research was provided to Julia Reece by the American Chemical Society – Petroleum Research Fund (grant #55617-DNI8) and to Tanner Mills by the American Association of Petroleum Geologists Grants-in-Aid Program and by a graduate fellowship from Aramco.

TABLE OF CONTENTS

Page

LIST OF FIGURES

Page

LIST OF TABLES

Page

1. INTRODUCTION

Microorganisms (bacteria and archaea) are ever-present in marine sediments (Delgado-Baquerizo et al., 2018; Finlay and Clarke, 1999; Francis et al., 2005). This is especially true for fine-grained siliciclastic sediments where deposition brings together the nutrients needed for microbial respiration, including organic matter, O_2, Fe^{3+}, SO_4^{2-}, and H_2 (Canfield et al., 1993; Lovley, 1991; Macquaker et al., 2014). Active microbial cells have been found to thrive in sediments down to burial depths of a few thousand meters (Inagaki et al., 2015). However, in general, the concentration of microbial cells is highest near the sediment-water interface and decreases with increasing depth (D'Hondt et al., 2004; Parkes et al., 1994). Thus, any interactions between microorganisms and sediments are limited at greater depths and stresses (Rebata-Landa & Santamarina, 2006).

Clay minerals are ubiquitous (Dutkiewicz et al., 2015; Griffin et al., 1968) and commonly dominate the mineralogy of fine-grained sediments (Lazar et al., 2015), which comprise the majority of sedimentary basin fill (Dewhurst et al., 1998). Clay minerals—such as smectite, illite, and kaolinite—are μm sized, layered aluminosilicates that are highly reactive (Sposito et al., 1999). This reactivity is due to their high surface area and unbalanced charge sites on their basal and edge surfaces (Mitchell and Soga, 2005; Sposito et al., 1999). In fact, these basal and edge charged sites can exchange H^+ with aqueous solutions such as sediment pore fluids (Avena et al., 2003; Gu and Evans, 2008).

In fine-grained sediments, microorganisms drive sediment pore fluid chemistry changes during early diagenesis (Canfield et al., 1993; Coleman, 1985; Irwin et al., 1977). As microorganisms oxidize organic carbon, they utilize various electron acceptors in the preferred order of O_2, Fe^{3+}, and SO_4^{2-} before they produce CH_4 (Froelich et al., 1979). All of these reactions alter sediment pore fluid pH and dissolved inorganic carbon concentrations and either promote dissolution or authigenic precipitation of carbonate minerals within sediments (Aller, 1982; Raiswell and Fisher, 2000; Zeng and Tice, 2014). Authigenic carbonate precipitation has likely acted as a significant carbon sink throughout Earth history during times of ocean anoxia (Schrag et al., 2013; Sun and Turchyn, 2014). However, the acid-base properties of clay minerals have never been studied in conjunction with sediment pore fluid pH and carbonate mineral saturation changes caused by these biogeochemical reactions.

Porosity, permeability, and compressibility of fine-grained sediments have been extensively studied by the geological and geotechnical engineering communities (Hart et al., 1995; Neuzil, 2019; Reece, 2021; Rubey and Hubbert, 1959; Skempton, 1970; Terzaghi, 1943). This is because the consolidation behavior of fine-grained sediments controls fluid flow (Dugan and Flemings, 2000), overpressure generation (Broichhausen et al., 2005; Long et al., 2011; Schneider et al., 2009), submarine landslide development (Dugan and Flemings, 2000), and the strength of faults (Hubbert and Rubey, 1959) in sedimentary basins. In fact, fine-grained sediments are more compressible than coarser-grained sediments (Dewhurst et al., 1998; Reece, 2021) and exhibit a rapid decline in porosity within the first several hundred meters of burial followed by a gradual decline

through deeper burial (Dzevanshir et al., 1986; Ingebritsen et al., 2006; Mondol et al., 2007). This loss in porosity during burial results in a decrease in permeability, as porosity and permeability are commonly observed to have a log-linear relationship (Neuzil, 1994, 2019; Reece et al., 2012; Schneider et al., 2011). Both the compressibility and permeability of sediments are dependent on various factors; the most important ones being grain size, grain shape, clay mineralogy, and stress history. However, the effects of microorganisms on the compression and permeability behavior of fine-grained sediments during burial are unexplored.

The alteration of clay minerals, specifically the smectite-to-illite transformation, can occur during burial of these fine-grained sediments (Eberl and Hower, 1976; Hower et al., 1976). The smectite-to-illite reaction has long been thought to only occur due to increased temperature, pressure, and time (Ahn and Peacor, 1989; Eberl and Hower, 1976; Hower et al., 1976). However, recent work has shown that this reaction can be induced by microorganisms at ambient temperatures and pressures and in short time periods (Kim et al., 2004; Koo et al., 2014; Koo et al., 2016; Zhang et al., 2007). This occurs as microorganisms reduce Fe^{3+} bound in the smectite structure (Kostka et al., 2002; Kostka et al., 1999; Kostka et al., 1996), which partially dissolves the smectite lattice (Dong et al., 2003). Despite showing microbial smectite-to-illite transformation using culture experiments with pure clay samples and nanometer scale observations (Kim et al., 2004; Koo et al., 2014; Koo et al., 2016), previous work has overlooked the importance of using natural marine sediments of various compositions in experimental work and multiple methods at different scales in analytical work. Moreover, recognition

of this reaction in natural environments is difficult and has yielded only speculative interpretations to date (Kim et al., 2019; Vorhies and Gaines, 2009).

The goals of this dissertation were to elucidate fundamental processes between microorganisms and clay-rich sediments during early burial and diagenesis. In Chapter 2, we utilized biogeochemical modeling that accounts for the acid-base properties of clay minerals to understand the effects of clay minerals on sediment pore fluid pH and carbonate saturation during early diagenesis. In Chapter 3, we performed resedimentation experiments with and without iron-reducing bacteria added to natural sediments to determine the effects of microorganisms on the porosity, permeability, and compressibility of fine-grained sediments during early burial. In Chapter 4, we utilize multiple analytical methods at multiple scales to measure the mineralogical and elemental compositions of natural sediments treated with and without iron-reducing bacteria to better understand the microbially driven smectite-to-illite reaction and carbonate diagenesis in natural sediments and at multiple scales.

1.1. References

Ahn, J. H., and Peacor, D. R., 1989, Illite/Smectite from Gulf Coast Shales: A Reappraisal of Transmission Electron Microscope Images: Clays and Clay Minerals, v. 37, p. 542-546, htpps://doi.org/10.1346/CCMN.1989.0370606.

Aller, R. C., 1982, Carbonate dissolutions in nearshore terrigenous muds: The role of physical and biological reworking: The Journal of Geology, v. 90, p. 79-95, https://doi.org/10.1086/628652.

Avena, M. J., Mariscal, M. M., and De Pauli, C. P., 2003, Proton binding at clay surfaces in water: Applied Clay Science, v. 24, p. 3-9, https://doi.org/10.1016/j.clay.2003.07.003.

Broichhausen, H. R., Littke, R., and Hantschel, T., 2005, Mudstone compaction and its influence on overpressure generation, elucidated by a 3D case study in the North Sea: International Journal of Earth Sciences, v. 94, p. 956-978, https://doi.org/10.1007/s00531-005-0014-1.

Canfield, D. E., Jørgensen, B. B., Fossing, H., Glud, R., Gundersen, J., Ramsing, N. B., Thamdrup, B., Hansen, J. W., Nielsen, L. P., and Hall, P. O. J., 1993, Pathways of organic carbon oxidation in three continental margin sediments: Marine Geology, v. 113, p. 27-40, https://doi.org/10.1016/0025-3227(93)90147-N.

Coleman, M. L., 1985, Geochemistry of diagenetic non-silicate minerals: kinetic considerations: Philosophical Transactions of the Royal Society of London A: Mathematical, Physical and Engineering Sciences, v. 315, p. 39-56, https://doi.org/10.1098/rsta.1985.0028.

D'Hondt, S., Jørgensen, B. B., Miller, D. J., Batzke, A., Blake, R., Cragg, B. A., Cypionka, H., Dickens, G. R., Ferdelman, T., Hinrichs, K.-U., Holm, N. G., Mitterer, R., Spivack, A., Wang, G., Bekins, B., Engelen, B., Ford, K., Gettemy, G., Rutherford, S. D., Sass, H., Skilbeck, C. G., Aiello, I. W., Guèrin, G., House, C. H., Inagaki, F., Meister, P., Naehr, T., Niitsuma, S., Parkes, R. J., Schippers, A., Smith, D. C., Teske, A., Wiegel, J., Padilla, C. N., and Acosta, J. L. S., 2004, Distributions of Microbial Activities in Deep Subseafloor Sediments: Science, v. 306, p. 2216, https://doi.org/10.1126/science.1101155.

Delgado-Baquerizo, M., Oliverio, A. M., Brewer, T. E., Benavent-González, A., Eldridge, D. J., Bardgett, R. D., Maestre, F. T., Singh, B. K., and Fierer, N., 2018, A global atlas of the dominant bacteria found in soil: Science, v. 359, p. 320, https://doi.org/10.1126/science.aap9516.

Dewhurst, D. N., Aplin, A. C., Sarda, J.-P., and Yang, Y., 1998, Compaction-driven evolution of porosity and permeability in natural mudstones: An experimental study: Journal of Geophysical Research: Solid Earth, v. 103, p. 651-661, https://doi.org/10.1029/97JB02540.

Dong, H., Kostka, J. E., and Kim, J., 2003, Microscopic Evidence for Microbial Dissolution of Smectite: Clays and Clay Minerals, v. 51, p. 502-512, 10.1346/CCMN.2003.0510504.

Dugan, B., and Flemings, P. B., 2000, Overpressure and fluid flow in the New Jersey continental slope: implications for slope failure and cold seeps: Science, v. 289, p. 288-291, https://doi.org/10.1126/science.289.5477.288.

Dutkiewicz, A., Müller, R. D., O'Callaghan, S., and Jónasson, H., 2015, Census of seafloor sediments in the world's ocean: Geology, v. 43, p. 795-798, https://doi.org/10.1130/G36883.1.

Dzevanshir, R. D., Buryakovskiy, L. A., and Chilingarian, G. V., 1986, Simple quantitative evaluation of porosity of argillaceous sediments at various depths of burial: Sedimentary Geology, v. 46, p. 169-175, https://doi.org/10.1016/0037-0738(86)90057-6.

Eberl, D., and Hower, J., 1976, Kinetics of illite formation: GSA Bulletin, v. 87, p. 1326-1330, 10.1130/0016-7606(1976)87<1326:KOIF>2.0.CO;2.

Finlay, B. J., and Clarke, K. J., 1999, Ubiquitous dispersal of microbial species: Nature, v. 400, p. 828-828, https://doi.org/10.1038/23616.

Francis, C. A., Roberts, K. J., Beman, J. M., Santoro, A. E., and Oakley, B. B., 2005, Ubiquity and diversity of ammonia-oxidizing archaea in water columns and sediments of the ocean: Proceedings of the National Academy of Sciences of the United States of America, v. 102, p. 14683, https://doi.org/10.1073/pnas.0506625102.

Froelich, P. N., Klinkhammer, G. P., Bender, M. L., Luedtke, N. A., Heath, G. R., Cullen, D., Dauphin, P., Hammond, D., Hartman, B., and Maynard, V., 1979, Early oxidation of organic matter in pelagic sediments of the eastern equatorial Atlantic: Suboxic diagenesis: Geochimica et Cosmochimica Acta, v. 43, p. 1075-1090, https://doi.org/10.1016/0016-7037(79)90095-4.

Griffin, J. J., Windom, H., and Goldberg, E. D., 1968, The distribution of clay minerals in the World Ocean: Deep Sea Research and Oceanographic Abstracts, v. 15, p. 433-459, https://doi.org/10.1016/0011-7471(68)90051-X.

Gu, X., and Evans, L. J., 2008, Surface complexation modelling of Cd(II), Cu(II), Ni(II), Pb(II) and Zn(II) adsorption onto kaolinite: Geochimica et Cosmochimica Acta, v. 72, p. 267-276, https://doi.org/10.1016/j.gca.2007.09.032.

Hart, B. S., Flemings, P. B., and Deshpande, A., 1995, Porosity and pressure: Role of compaction disequilibrium in the development of geopressures in a Gulf Coast Pleistocene basin: Geology, v. 23, p. 45-48, https://doi.org/10.1130/0091-7613(1995)023<0045:PAPROC>2.3.CO;2.

Hower, J., Eslinger, E. V., Hower, M. E., and Perry, E. A., 1976, Mechanism of burial metamorphism of argillaceous sediment: 1. Mineralogical and chemical evidence: GSA Bulletin, v. 87, p. 725-737, https://doi.org/10.1130/0016-7606(1976)87<725:MOBMOA>2.0.CO;2.

Hubbert, M. K., and Rubey, W. W., 1959, Role of fluid pressure in mechanics of overthrust faulting, Part 1. Mechanics of fluid-filled porous solids and its application to overthrust faulting: Geological Society of America Bulletin, v. 70, p. 115-166, https://doi.org/10.1130/0016-7606(1959)70[115:ROFPIM]2.0.CO;2.

Inagaki, F., Hinrichs, K. U., Kubo, Y., Bowles, M. W., Heuer, V. B., Hong, W. L., Hoshino, T., Ijiri, A., Imachi, H., Ito, M., Kaneko, M., Lever, M. A., Lin, Y. S., Methé, B. A., Morita, S., Morono, Y., Tanikawa, W., Bihan, M., Bowden, S. A., Elvert, M., Glombitza, C., Gross, D., Harrington, G. J., Hori, T., Li, K., Limmer, D., Liu, C. H., Murayama, M., Ohkouchi, N., Ono, S., Park, Y. S., Phillips, S. C., Prieto-Mollar, X., Purkey, M., Riedinger, N., Sanada, Y., Sauvage, J., Snyder, G., Susilawati, R., Takano, Y., Tasumi, E., Terada, T., Tomaru, H., Trembath-Reichert, E., Wang, D. T., and Yamada, Y., 2015, Exploring deep microbial life in coal-bearing sediment down to ~2.5 km below the ocean floor: Science, v. 349, p. 420-424, https://doi.org/10.1126/science.aaa6882.

Ingebritsen, S. E., Sanford, W. E., and Neuzil, C. E., 2006, Groundwater in Geologic Processes, 2nd Edition, Cambridge, UK, Cambridge University Press, 562 p.

Irwin, H., Curtis, C., and Coleman, M., 1977, Isotopic evidence for source of diagenetic carbonates formed during burial of organic-rich sediments: Nature, v. 269, p. 209-213, htpps://doi.org/10.1038/269209a0.

Kim, J., Dong, H., Seabaugh, J., Newell, S. W., and Eberl, D. D., 2004, Role of Microbes in the Smectite-to-Illite Reaction: Science, v. 303, p. 830-832,

Kim, J., Dong, H., Yang, K., Park, H., Elliott, W. C., Spivack, A., Koo, T.-h., Kim, G., Morono, Y., Henkel, S., Inagaki, F., Zeng, Q., Hoshino, T., and Heuer, V. B., 2019, Naturally occurring, microbially induced smectite-to-illite reaction: Geology, v. 47, p. 535-539, https://doi.org/10.1130/G46122.1.

Koo, T.-h., Jang, Y.-n., Kogure, T., Kim, J. H., Park, B. C., Sunwoo, D., and Kim, J.-w., 2014, Structural and chemical modification of nontronite associated with microbial Fe(III) reduction: Indicators of “illitization”: Chemical Geology, v. 377, p. 87-95, https://doi.org/10.1016/j.chemgeo.2014.04.005.

Koo, T.-h., Lee, G., and Kim, J.-w., 2016, Biogeochemical dissolution of nontronite by Shewanella oneidensis MR-1: Evidence of biotic illite formation: Applied Clay Science, v. 134, p. 13-18, https://doi.org/10.1016/j.clay.2016.03.030.

Kostka, J. E., Dalton, D. D., Skelton, H., Dollhopf, S., and Stucki, J. W., 2002, Growth of Iron(III)-Reducing Bacteria on Clay Minerals as the Sole Electron Acceptor and Comparison of Growth Yields on a Variety of Oxidized Iron Forms: Applied and Environmental Microbiology, v. 68, p. 6256-6262, 10.1128/aem.68.12.6256-6262.2002.

Kostka, J. E., Haefele, E., Viehweger, R., and Stucki, J. W., 1999, Respiration and Dissolution of Iron(III)-Containing Clay Minerals by Bacteria: Environmental Science & Technology, v. 33, p. 3127-3133, 10.1021/es990021x.

Kostka, J. E., Stucki, J. W., Nealson, K. H., and Wu, J., 1996, Reduction of structural Fe(III) in smectite by a pure culture of Shewanella Putrefaciens strain MR-1: Clays and Clay Minerals, v. 44, p. 522-529,

Lazar, O. R., Bohacs, K. M., Macquaker, J. H. S., Schieber, J., and Demko, T. M., 2015, Capturing Key Attributes of Fine-Grained Sedimentary Rocks In Outcrops, Cores, and Thin Sections: Nomenclature and Description Guidelines: Journal of Sedimentary Research, v. 85, p. 230-246, https://doi.org/10.2110/jsr.2015.11.

Long, H., Flemings, P. B., Germaine, J. T., and Saffer, D. M., 2011, Consolidation and overpressure near the seafloor in the Ursa Basin, deepwater Gulf of Mexico: Earth and Planetary Science Letters, v. 305, p. 11-20, https://doi.org/10.1016/j.epsl.2011.02.007.

Lovley, D. R., 1991, Dissimilatory Fe(III) and Mn(IV) reduction: Microbiological Reviews, v. 55, p. 259-287.

Macquaker, J. H. S., Taylor, K. G., Keller, M., and Polya, D., 2014, Compositional controls on early diagenetic pathways in fine-grained sedimentary rocks: Implications for Predicting unconventional reservoir attributes of mudstones: AAPG Bulletin, v. 98, p. 587-603.

Mitchell, J. K., and Soga, K., 2005, Fundamentals of Soil Behavior, 3rd Edition, John Wiley & Sons, Inc., 592 p.

Mondol, N. H., Bjørlykke, K., Jahren, J., and Høeg, K., 2007, Experimental mechanical compaction of clay mineral aggregates—Changes in physical properties of mudstones during burial: Marine and Petroleum Geology, v. 24, p. 289-311, https://doi.org/10.1016/j.marpetgeo.2007.03.006.

Neuzil, C. E., 1994, How permeable are clays and shales?: Water Resources Research, v. 30, p. 145-150, https://doi.org/10.1029/93WR02930.

Neuzil, C. E., 2019, Permeability of Clays and Shales: Annual Review of Earth and Planetary Sciences, v. 47, p. 247-273, https://doi.org/10.1146/annurev-earth-053018-060437.

Parkes, R. J., Cragg, B. A., Bale, S. J., Getlifff, J. M., Goodman, K., Rochelle, P. A., Fry, J. C., Weightman, A. J., and Harvey, S. M., 1994, Deep bacterial biosphere in Pacific Ocean sediments: Nature, v. 371, p. 410-413, https://doi.org/10.1038/371410a0.

Raiswell, R., and Fisher, Q. J., 2000, Mudrock-hosted carbonate concretions: A review of growth mechanisms and their influence on chemical and isotopic composition: Journal of the Geological Society, v. 157, p. 239-251, https://doi.org/10.1144/jgs.157.1.239.

Reece, J. S., 2021, The Impact of Grain Size on the Hydromechanical Behavior of Mudstones: Geochemistry, Geophysics, Geosystems, v. 22, p. 1-23, https://doi.org/10.1029/2021GC009732.

Reece, J. S., Flemings, P. B., Dugan, B., Long, H., and Germaine, J. T., 2012, Permeability-porosity relationships of shallow mudstones in the Ursa Basin, northern deepwater Gulf of Mexico: Journal of Geophysical Research: Solid Earth, v. 117, p. 1-13, https://doi.org/10.1029/2012JB009438.

Rubey, W. W., and Hubbert, M. K., 1959, Role of fluid pressure in mechanics of overthrust faulting, Part 2. Overthrust belt in geosynclinal are of western Wyoming in light of fluid-pressure hypothesis: Geological Society of America Bulletin, v. 70, p. 167-205, https://doi.org/10.1130/0016-7606(1959)70[167:ROFPIM]2.0.CO;2.

Schneider, J., Flemings, P. B., Day-Stirrat, R. J., and Germaine, J. T., 2011, Insights into pore-scale controls on mudstone permeability through resedimentation experiments: Geology, v. 39, p. 1011-1014, https://doi.org/10.1130/G32475.1.

Schneider, J., Flemings, P. B., Day-Stirrat, R. J., and Germaine, J. T., 2009, Overpressure and consolidation near the seafloor of Brazos-Trinity Basin IV, Northwest Deepwater Gulf of Mexico: Journal of Geophysical Research, v. 114, B05102, https://doi.org/10.1029/2008JB005922.

Schrag, D. P., Higgins, J. A., Macdonald, F. A., and Johnston, D. T., 2013, Authigenic carbonate and the history of the global carbon cycle: Science, v. 339, p. 540, https://doi.org/10.1126/science.1229578.

Skempton, A. W., 1970, The consolidation of clays by gravitational compaction: Quarterly Journal of the Geological Society of London, v. 125, p. 373-411, https://doi.org/10.1144/gsjgs.125.1.0373.

Sposito, G., Skipper, N. T., Sutton, R., Park, S.-h., Soper, A. K., and Greathouse, J. A., 1999, Surface geochemistry of the clay minerals: Proceedings of the National Academy of Sciences, v. 96, p. 3358-3364, https://doi.org/10.1073/pnas.96.7.3358.

Sun, X., and Turchyn, A. V., 2014, Significant contribution of authigenic carbonate to marine carbon burial: Nature Geoscience, v. 7, p. 201, https://doi.org/10.1038/ngeo2070.

Terzaghi, K., 1943, Theory of Consolidation, Theoretical Soil Mechanics, John Wiley & Sons, Inc., p. 265-296.

Vorhies, J. S., and Gaines, R. R., 2009, Microbial dissolution of clay minerals as a source of iron and silica in marine sediments: Nature Geoscience, v. 2, p. 221-225, https://doi.org/10.1038/ngeo441.

Zeng, Z., and Tice, M. M., 2014, Promotion and nucleation of carbonate precipitation during microbial iron reduction: Geobiology, v. 12, p. 362-371, https://doi.org/10.1111/gbi.12090.

Zhang, G., Dong, H., Kim, J., and Eberl, D. D., 2007, Microbial reduction of structural Fe3+ in nontronite by a thermophilic bacterium and its role in promoting the smectite to illite reaction: American Mineralogist, v. 92, p. 1411-1419, https://doi.org/10.2138/am.2007.2498.

2. CLAY MINERALS MODULATE EARLY CARBONATE DIAGENESIS[1]

2.1. Abstract

Early diagenetic precipitation of authigenic carbonate has been a globally significant carbon sink throughout Earth history. In particular, SO_4^{2-} and Fe^{3+} reduction and CH_4 production create conditions in pore fluids which promote carbonate mineral precipitation; however, these conditions may be modified by the presence of acid-base buffers such as clay minerals. We integrate the acid-base properties of clay minerals into a biogeochemical model that predicts the evolution of pore-water pH and carbonate mineral saturation during O_2, Fe^{3+}, and SO_4^{2-} reduction and CH_4 production. Key model inputs are obtained using two natural clay mineral–rich sediments from the Integrated Ocean Drilling Program as well as from literature. We found that clay minerals can enhance carbonate mineral saturation during O_2 and SO_4^{2-} reduction and moderate saturation during Fe^{3+} reduction and CH_4 production if the pore-fluid pH and clay mineral pK_a values are within ~2 log units of one another. We therefore suggest that clay minerals could modify significantly the environmental conditions and settings in which early diagenetic carbonate precipitation occurs. In Phanerozoic marine sediments—where O_2 and SO_4^{2-} have been the main oxidants of marine sedimentary organic

---

[1] Published article in *Geology*: Mills, N.T., Reece, J.S., and Tice, M.M., 2021, Clay minerals modulate early carbonate diagenesis: Geology, v. 49, p. 1015-1019, https://doi.org/10.1130/G48713.1.

carbon—clay minerals have likely inhibited carbonate dissolution and promoted precipitation of authigenic carbonate.

2.2. Introduction

Clay minerals are ubiquitous (Griffin et al., 1968) and chemically reactive (Sposito et al., 1999). As a result, they participate in many diagenetic reactions in marine sediments, such as the smectite-to-illite transformation or clay mineral authigenesis (e.g., Eberl and Hower, 1976; Michalopoulos and Aller, 1995). However, when considering the effects of clay minerals on sediment diagenesis, their acid-base properties have previously been overlooked.

The edge and basal surfaces of clay minerals contain charged sites that can exchange H^+ with aqueous solutions such as sediment pore fluids (Gu and Evans, 2008). The exchange of H^+ on edge sites is an amphoteric, pH dependent process (Equation 2.1; Avena et al., 2003), while H^+ exchange on the permanent negatively charged basal sites depends on the relative aqueous activities of H^+ and other cations (Equation 2.2; where Me^{n+} is a given metal cation; Barbier et al., 2000; Schoonheydt and Johnston, 2013). These reversible protonation and deprotonation properties allow clay minerals to buffer changes in pore fluid pH.

$$\text{clay:OH} \leftrightarrow \text{clay:}\,O^- + H^+ \,, \qquad \text{(Eq. 2.1)}$$

$$\text{clay:}^-\cdot\, H^+ + Me^{n+} \leftrightarrow \text{clay:}^-\cdot\, Me^{n+} + H^+ \,. \qquad \text{(Eq. 2.2)}$$

Previous research concerning early sediment diagenesis has focused on biogeochemical reactions as the primary driver of pore-fluid chemistry changes (e.g., Canfield et al., 1993; Coleman, 1985; Irwin et al., 1977). As microorganisms oxidize

organic C they utilize various electron acceptors in the preferred order of O_2, Fe^{3+}, and SO_4^{2-} before they produce CH_4 (Froelich et al., 1979). All of these reactions alter sediment pore-fluid pH and the concentration of dissolved inorganic C (DIC), which is exemplified by the respective stoichiometries of O_2, Fe^{3+}, and SO_4^{2-} reduction and hydrogenotrophic CH_4 production:

$$CH_2O + O_2 \rightarrow CO_2 + H_2O \text{ ,} \quad \text{(Eq. 2.3)}$$

$$CH_2O + 4Fe(OH)_3 + 7H^+ \rightarrow HCO_3^- + 4Fe^{2+} + 10H_2O \text{ ,} \quad \text{(Eq. 2.4)}$$

$$2CH_2O + SO_4^{2-} \rightarrow 2HCO_3^- + HS^- + H^+ \text{ ,} \quad \text{(Eq. 2.5)}$$

$$HCO_3^- + 4H_2 + H^+ \rightarrow CH_4 + 3H_2O \text{ .} \quad \text{(Eq. 2.6)}$$

Therefore, these reactions can promote either dissolution or authigenic precipitation of carbonate minerals within sediments (e.g., Aller, 1982; Raiswell and Fisher, 2000; Zeng and Tice, 2014). Authigenic carbonate precipitation has likely acted as a significant C sink throughout Earth history during times of ocean anoxia (Schrag et al., 2013; Sun and Turchyn, 2014).

Given that these biogeochemical reactions alter pore-fluid pH and carbonate saturation, and that organic C and clay minerals are commonly co-deposited in marine sediments, we postulate that the acid-base properties of clay minerals may be able to moderate these changes during the earliest stages of sediment diagenesis. Here, we test this hypothesis by using a biogeochemical model that accounts for these clay mineral properties. Finally, we explore realistic conditions in which clay minerals likely buffer pore-fluid pH and carbonate saturation as well as explore links between clay minerals and the C cycle.

2.3. Biogeochemical Model and Materials

We developed a biogeochemical model for O_2, Fe^{3+}, and SO_4^{2-} reduction and CH_4 production that accounts for the acid-base reactions of clay minerals (model details are in Appendix A and Python code is in Appendix B). The model predicts the evolution of sediment pore-fluid pH and carbonate saturation (*SI*) as a function of the oxidants consumed (O_2, Fe^{3+}, SO_4^{2-}) or CH_4 produced in a closed system. We assumed a pore-fluid composition that is similar to modern seawater and the model uses effective speciation terms appropriate for seawater composition and ionic strength. Ion pairs found to have an insignificant effect on modeled pore-fluid pH and *SI* were dropped from our calculations. We also assumed that all clay mineral effective charge sites are available for H^+ exchange. Initial conditions are the initial pH (pH_0) and saturation index (SI_0); model parameters are the acid dissociation constants (pK_a) and the total acidity values of the clay minerals (concentration of sites that can be protonated or deprotonated).

Natural clay mineral–rich sediments were used to provide clay acid-base properties for model calculations. Two bulk sediment powders were created using homogenized sediments collected from Integrated Ocean Drilling Program (IODP) sediment cores. They include the Nankai (Japan) sediment from IODP Expedition 322 and the Gulf of Mexico sediment from IODP Expedition 308 (Figure 2.1; see Appendix A for sediment details). The Nankai and Gulf of Mexico sediments are composed of 56% and 59% clay-size (<2μm) particles, respectively (Table A1). By mineralogy, the bulk Nankai and Gulf of Mexico sediments are composed of 48 wt.% and 34 wt.% clay

minerals, respectively (Table A2), and both sediments contain a mixture of smectite, illite, and kaolinite, which dominate the <2μm fraction (Table A3).

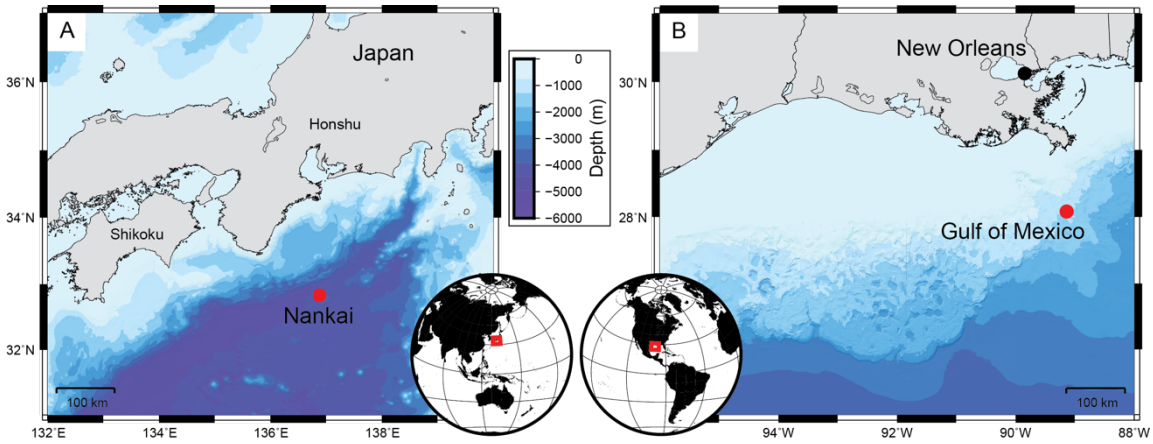

Figure 2.1 Bathymetric maps showing the locations of (A) the Nankai sediment and (B) the Gulf of Mexico sediment.

Potentiometric titrations were performed on the <2μm fraction of both samples to determine their pK_a and clay acidity values using a Metrohm Titrando 907 autotitrator (see the Appendix A for details). Samples were titrated up, down, and back up in a pH range of 3.5–11 and in a 0.56 M NaCl solution (seawater ionic strength). Prior to titrations, each sediment sample was prepared by removing calcite and organic matter, obtaining the <2μm fraction, and saturating the clay minerals with Na. To prevent CO_2 contamination, the solutions were bubbled with N_2 prior to and during each titration in a sealed container. Because both sediment samples consist of three clay mineral types, we determine effective pK_a values (Davranche et al. 2003; Stumm, 1992) for seawater

conditions without attempting to distinguish between clay minerals and the type of charged sites.

Our titrations yielded pK_a values of 4.26, 6.65, and 8.75 and respective acidity values of 0.18 mmol g^{-1}, 0.05 mmol g^{-1}, and 0.07 mmol g^{-1} for the Nankai sediment, and pK_a values of 4.86, 6.93, and 8.92 and respective acidity values of 0.04 mmol g^{-1}, 0.03 mmol g^{-1}, and 0.05 mmol g^{-1} for the Gulf of Mexico sediment (Table A4). For comparison, we gather model inputs for a Cretaceous montmorillonite from Wyoming—the SWy-2 sample from Tombácz et al. (2004)—that has an edge site pK_a value of 7.9 and clay acidity value of 0.04 mmol g^{-1} (basal site pK_a is outside the pH range of interest and is unused).

2.4. Model Results

We present our model results for aerobic (sequential O_2, Fe^{3+}, and SO_4^{2-} reduction and CH_4 production), ferruginous (Fe^{3+} and SO_4^{2-} reduction and CH_4 production), and sulfidic (SO_4^{2-} reduction and CH_4 production) water-column scenarios (Figure 2.2, left to right). In each scenario, the model predicts the evolution of pore-fluid pH and *SI* with (simulated sediment pore fluid) and without (unbuffered pore fluid) clay mineral–rich sediment buffers as well as the evolution of DIC. We define the terms ΔpH and Δ*SI* as the differences between the respective pH and *SI* curves with and without a clay buffer, where positive (negative) values indicate that the pH and *SI* in the presence of a clay buffer are higher (lower) than they would be without a clay buffer.

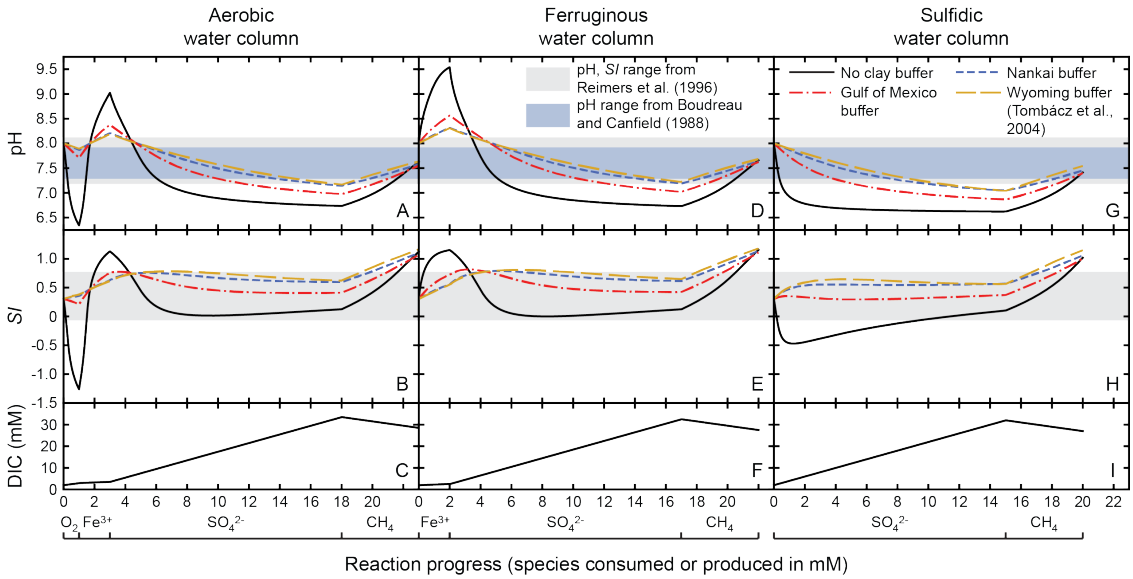

Figure 2.2 Modeled evolution of pore-fluid pH, carbonate saturation index (SI), and dissolved inorganic carbon (DIC) under aerobic (A-C), ferruginous (D-F), and sulfidic (G-I) conditions for circumstances with and without clay mineral–rich buffer. Gray and blue shaded areas in pH and SI plots represent measured pH and SI values in marine sediments from Reimers et al. (1996) and Boudreau and Canfield (1988; and references therein), respectively.

In the aerobic water-column scenario, the simulated Gulf of Mexico pore fluids displayed higher pH and *SI* values at the end of O_2 reduction than pore fluids without a sediment buffer (ΔpH=1.4; Δ*SI*=1.5; Figures 2.2A and 2.2B), predicting less carbonate dissolution during O_2 reduction than in unbuffered sediments. The simulated Nankai and Wyoming pore-fluid pH values were buffered so effectively that *SI* increased during O_2 reduction, implying that carbonate precipitation could occur (ΔpH and Δ*SI* values all >1.52; Figures 2.2A and 2.2B). Later in the reaction progress, all three sediments continued to buffer pore fluids, even at high DIC values, by partially inhibiting carbonate mineral saturation during Fe^{3+} reduction (ΔpH and Δ*SI* values all <–0.3) and

CH_4 production (rate of unbuffered pore-fluid pH and *SI* increase > the clay-buffered pore fluids) and increasing carbonate mineral saturation during SO_4^{2-} reduction (ΔpH and Δ*SI* values all >0.2; Figures 2.2A-2.2C).

In the ferruginous water-column scenario, the simulated Nankai, Gulf of Mexico, and Wyoming pore fluids displayed lower pH and *SI* values during Fe^{3+} reduction (ΔpH and Δ*SI* values all <–0.4) and higher pH and *SI* values during SO_4^{2-} reduction (ΔpH and Δ*SI* values all >0.3) than the unbuffered pore fluids, even at high DIC values, implying that carbonate precipitation is partially moderated during Fe^{3+} reduction and promoted during SO_4^{2-} reduction (Figures 2.2D-2.2F). During CH_4 production, all three sediments continued to buffer the simulated pore fluids by partially inhibiting the rise in pH and *SI* values (Figures 2.2D and 2.2E).

In the sulfidic water-column scenario, the simulated Nankai, Gulf of Mexico, and Wyoming pore fluids displayed higher pH and *SI* values during SO_4^{2-} reduction than the unbuffered pore fluids (ΔpH and Δ*SI* values all >0.3; Figures 2.2G and 2.2H). The simulated Nankai and Wyoming pore fluids both displayed an increase in *SI* from the onset of SO_4^{2-} reduction, implying that carbonate precipitation could occur even at the earliest stages of SO_4^{2-} reduction due to increased DIC and buffered pH (Figures 2.2G-2.2I). At higher DIC values, during CH_4 production, the three sediments continued to buffer the simulated pore fluids by partially inhibiting the rise in pH and *SI* values (Figures 2.2G-2.2I).

2.5. Discussion

The pH of a fluid is most difficult to change when pH is close to the pK_a value of a buffer and when that buffer has a high capacity. For example, the Wyoming sediment has the greatest buffering capacity, while having a modest clay acidity value, because its one relevant pK_a value is nearly identical to the pH_0 of each water-column scenario (7.9 and 8, respectively). The Nankai and Gulf of Mexico sediments are less effective buffers, despite having slightly higher clay acidity values, because each of their two relevant pK_a values are ~1–2 log units from the pH_0 value. Of these two sediments, the Nankai is a better buffer due to its higher clay acidity values. For these reasons, all three sediment samples adequately buffered pore-fluid pH and *SI* in our model. In fact, the modeled pore-fluid pH and *SI* values for the three sediment samples better approximate real-world, measured pH and *SI* values from marine sediments (Figure 2.2; shaded areas) than our unbuffered model as well as other models that do not include clay minerals (e.g., Meister, 2013).

The effects of pH_0, clay mineral pK_a, and clay acidity on the buffering capacity of clay minerals are further explored by performing a sensitivity study. We plotted the greatest ΔSI values at specific sets of pH_0 and pK_a values for a claystone and siltstone, i.e., high and low clay acidity values, respectively (Figure 2.3; a similar plot of ΔpH values shown in Figure A2). Significantly, the greatest ΔSI values occur when pH_0 and clay mineral pK_a values are close (within ~2 log units; Figure 2.3). In marine sediments, feasible pore-fluid pH values could range from 6.5 to 9 (Ben-Yaakov, 1973). Our titrations yielded clay mineral pK_a values from 4.2 to 8.9, consistent with published clay

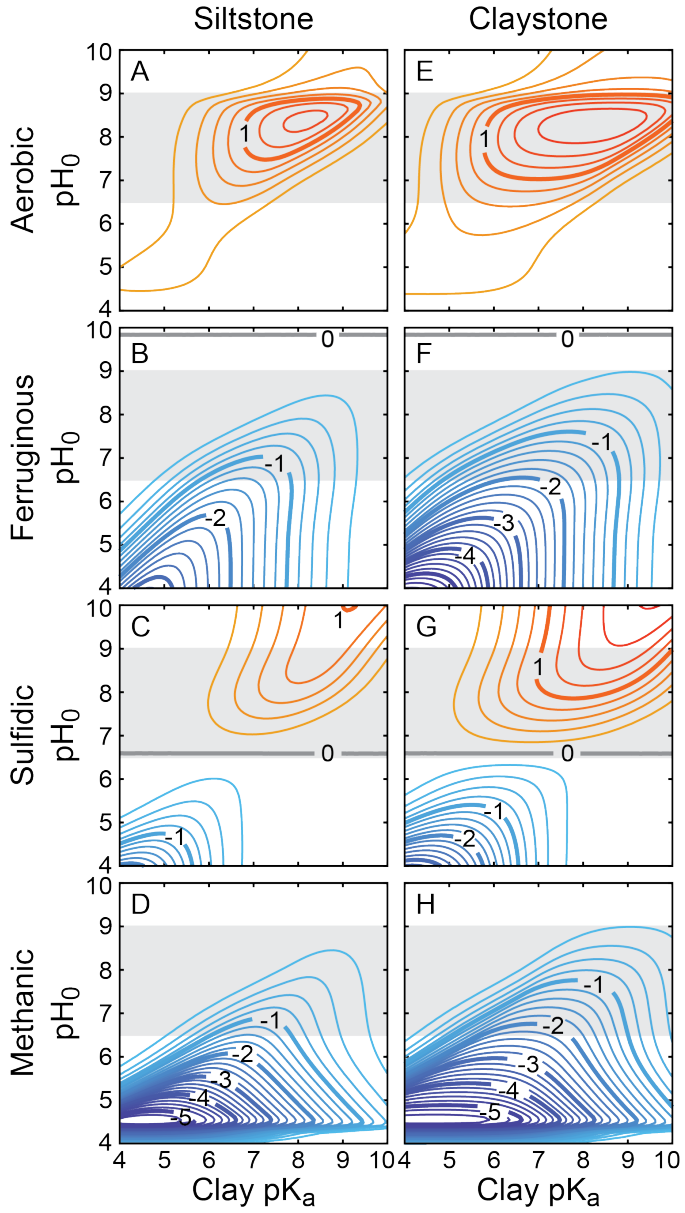

Figure 2.3 Effects of initial pH and clay pK_a on pore-fluid evolution. Siltstone (A-D; ~10 wt.% clay minerals) and claystone (E-H; ~70% clay minerals) sediments could buffer pore-fluid carbonate saturation (*SI*) at a wide range of initial pH (pH_0) and clay mineral pK_a values under aerobic, ferruginous, sulfidic, and methanic conditions. Contours represent greatest ΔSI values for set of particular pK_a and pH_0 values. Shaded areas represent likely pore-fluid pH values found in marine sediments (6.5–9; Ben-Yaakov, 1973) and clay mineral pK_a values found in nature (4–10; Duc et al., 2005). ΔSI is difference between *SI* curves with and without clay buffer, where positive values indicate increased *SI*, and negative values indicate decreased *SI*.

mineral (smectite, illite, and kaolinite) pK_a values that range from 4 to 10 (e.g., Duc et al., 2005; Kriaa et al., 2009; Liu et al., 2018). Thus, in typical marine pore fluids (pH = 6.5–9) and for typical clay minerals (pK_a = 4–10; shaded areas in Figure 2.3), clay buffering effectively moderates changes in sediment pore-fluid pH and *SI*. During O_2 and SO_4^{2-} reduction, carbonate mineral saturation is greater than without clay buffers and carbonate minerals could potentially be precipitated in clay-rich sediments via buffered pH and increased DIC (Figures 2.3E and 2.3G). Conversely, clay buffering during the rise in pH created by Fe^{3+} reduction and CH_4 production limits carbonate mineral saturation, potentially reducing the amount of precipitation in clay-rich sediments (Figures 2.3F and 2.3H). While not modeled here, adsorption of Fe^{2+} (produced during Fe^{3+} reduction) onto clay minerals would also limit the rise of pH and *SI*. For a siltstone, the effects of clay minerals on pore-fluid *SI* are diminished (Figures 2.3A-2.3D). Given that clay minerals may buffer pore-fluid *SI* for common natural pH and pK_a values, it is likely that this previously ignored attribute of clay minerals may have an impact on global authigenic carbonate precipitation in marine sediments.

In areas of the modern seafloor dominated by clay minerals (Dutkiewicz et al., 2015) and below oxygen minimum zones (low dissolved O_2 concentrations 400 m below the sea surface; Garcia et al., 2018), authigenic carbonates are being precipitated at higher rates (Figure 2.4; Sun and Turchyn, 2014). This is especially true off the western coast of South, Central, and North America and off the western coast of Central Africa (Figure 2.4). The global distribution of authigenic carbonate minerals in marine sediments is likely a result of alkalinity created by microbial SO_4^{2-} reduction via organic

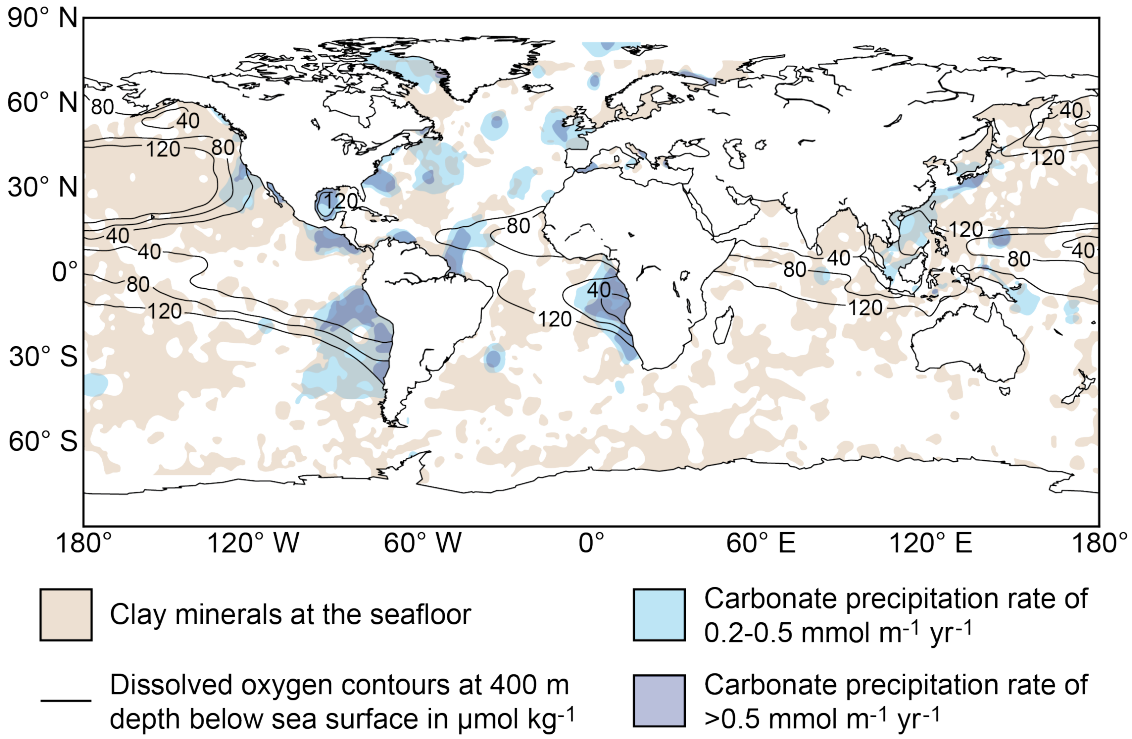

Figure 2.4 Global marine distributions of clay minerals at seafloor (Dutkiewicz et al., 2015), authigenic carbonate precipitation (Sun and Turchyn, 2014), and dissolved oxygen concentrations 400 m below the sea surface (oxygen minimum zones; annual climatological mean; Garcia et al., 2018). In areas west of South, Central, and North America and west of Central Africa, sediments are dominated by clay minerals, deposited in low-oxygen conditions, and they have higher rates of authigenic carbonate precipitation.

C oxidation (Equation 2.5) or anaerobic methane oxidation (Equation 2.7; Sun and Turchyn, 2014).

$$CH_4 + SO_4^{2-} \rightarrow HCO_3^- + HS^- + H_2O\,. \qquad \text{(Eq. 2.7)}$$

Interestingly, during clay-unbuffered SO_4^{2-} reduction paired with organic C oxidation (or in circumstances where ≤80% of SO_4^{2-} reduction is paired with anaerobic methane oxidation; Meister, 2013) an initial drop in pore-fluid pH occurs until bicarbonate protonation buffers further change; this causes the pore-fluid *SI* to initially

drop but then gradually rise as bicarbonate accumulates. The initial drop in carbonate mineral saturation makes SO_4^{2-} reduction a poor driver of new carbonate precipitation in clay-poor sediments (Meister, 2013). In contrast, our analysis suggests that the initial decrease in pH and *SI* caused by SO_4^{2-} reduction is often buffered by clay minerals in clay-rich sediments. Consequently, authigenic carbonate precipitation would be promoted where low-oxygen conditions coincide with widespread areas of clay deposition, such as west of South, Central, and North America and west of Central Africa (Figure 2.4).

For most of the Phanerozoic, O_2 and SO_4^{2-} have been the primary global oxidants of marine sedimentary organic C (e.g., Canfield and Farquhar, 2009; Loyd et al., 2012). Authigenic carbonate precipitation may therefore have been promoted throughout that time during intervals of increased clay mineral deposition and widespread ocean deoxygenation, e.g., the Cretaceous (Jenkyns, 1980). In contrast, prior to the initial increase of SO_4^{2-} in the oceans during the Paleoproterozoic (Farquhar et al., 2000), Fe^{3+} reduction may have played a greater role in authigenic carbonate precipitation. At that time, clay minerals would have diminished the authigenic C sink. Ultimately, clay minerals may have played critical roles in moderating or enhancing C cycling from sediments back into the ocean-atmosphere system by buffering pore fluids during carbonate cement authigenesis.

2.6. References

Aller, R. C., 1982, Carbonate dissolutions in nearshore terrigenous muds: The role of physical and biological reworking: The Journal of Geology, v. 90, p. 79-95, https://doi.org/10.1086/628652.

Avena, M. J., Mariscal, M. M., and De Pauli, C. P., 2003, Proton binding at clay surfaces in water: Applied Clay Science, v. 24, p. 3-9, https://doi.org/10.1016/j.clay.2003.07.003.

Barbier, F., Duc, G., and Petit-Ramel, M., 2000, Adsorption of lead and cadmium ions from aqueous solution to the montmorillonite/water interface: Colloids and Surfaces A: Physiochemical and Engineering Aspects, v. 166, p. 153-159, https://doi.org/10.1016/S0927-7757(99)00501-4.

Ben-Yaakov, S., 1973, pH buffering of pore water of recent anoxic marine sediments: Limnology and Oceanography, v. 18, p. 86-94, https://doi.org/10.4319/lo.1973.18.1.0086.

Boudreau, B.P., and Canfield, D.E., 1988, A provisional diagenetic model for pH in anoxic porewaters: application to the FOAM site: Journal of Marine Research, v. 46, p. 429-455, https://doi.org/10.1357/002224088785113603.

Canfield, D. E., and Farquhar, J., 2009, Animal evolution, bioturbation, and the sulfate concentration of the oceans: Proceedings of the National Academy of Sciences, v. 106, p. 8123-8127, https://doi.org/10.1073/pnas.0902037106.

Canfield, D. E., Jørgensen, B. B., Fossing, H., Glud, R., Gundersen, J., Ramsing, N. B., Thamdrup, B., Hansen, J. W., Nielsen, L. P., and Hall, P. O. J., 1993, Pathways of organic carbon oxidation in three continental margin sediments: Marine Geology, v. 113, p. 27-40, https://doi.org/10.1016/0025-3227(93)90147-N.

Coleman, M. L., 1985, Geochemistry of diagenetic non-silicate minerals: kinetic considerations: Philosophical Transactions of the Royal Society of London A: Mathematical, Physical and Engineering Sciences, v. 315, p. 39-56, https://doi.org/10.1098/rsta.1985.0028.

Davranche, M., Lacour, S., Bordas, F., and Bollinger, J.C., 2003, An easy determination of the surface chemical properties of simple and natural solids: Journal of Chemical Education, v. 80, p. 76-78, https://doi.org/10.1021/ed080p76.

Duc, M., Gaboriaud, F., and Thomas, F., 2005, Sensitivity of the acid–base properties of clays to the methods of preparation and measurement: 1. Literature review: Journal of Colloid and Interface Science, v. 289, p. 139-147, https://doi.org/10.1016/j.jcis.2005.03.060.

Dutkiewicz, A., Müller, R. D., O'Callaghan, S., and Jónasson, H., 2015, Census of seafloor sediments in the world's ocean: Geology, v. 43, p. 795-798, https://doi.org/10.1130/G36883.1.

Eberl, D., and Hower, J., 1976, Kinetics of illite formation: Geological Society of America Bulletin, v. 87, p. 1326-1330, https://doi.org/10.1130/0016-7606(1976)87<1326:KOIF>2.0.CO;2.

Farquhar, J., Bao, H., and Thiemens, M., 2000, Atmospheric influence of Earth's earliest sulfur cycle: Science, v. 289, p. 756-758, https://doi.org/10.1126/science.289.5480.756.

Froelich, P. N., Klinkhammer, G. P., Bender, M. L., Luedtke, N. A., Heath, G. R., Cullen, D., Dauphin, P., Hammond, D., Hartman, B., and Maynard, V., 1979, Early oxidation of organic matter in pelagic sediments of the eastern equatorial Atlantic: Suboxic diagenesis: Geochimica et Cosmochimica Acta, v. 43, p. 1075-1090, https://doi.org/10.1016/0016-7037(79)90095-4.

Garcia, H.E., Weathers, K., Paver, C.R., Smolyar, I., Boyer, T.P., Locarnini, R.A., Zweng, M.M., Mishonov, A.V., Baranova, O.K., Seidov, D., and Reagan, J.R., 2018, World ocean atlas 2018, volume 3: dissolved oxygen, apparent oxygen utilization, and oxygen saturation, *in* Mishonov, A., ed., NOAA Atlas NESDIS 83: Silver Spring, MD, 38 p.

Griffin, J.J., Windom, H., and Goldberg, E.D., 1968, The distribution of clay minerals in the World Ocean: Deep Sea Research and Oceanographic Abstracts, v. 15, p. 433-459, https://doi.org/10.1016/0011-7471(68)90051-x.

Gu, X., and Evans, L.J., 2008, Surface complexation modelling of Cd(II), Cu(II), Ni(II), Pb(II) and Zn(II) adsorption onto kaolinite: Geochimica et Cosmochimica Acta, v. 72, p. 267-276, https://doi.org/10.1016/j.gca.2007.09.032.

Irwin, H., Curtis, C., and Coleman, M., 1977, Isotopic evidence for source of diagenetic carbonates formed during burial of organic-rich sediments: Nature, v. 269, p. 209, https://doi.org/10.1038/269209a0.

Jenkyns, H. C., 1980, Cretaceous anoxic events: from continents to oceans: Journal of the Geological Society, v. 137, p. 171, https://doi.org/10.1144/gsjgs.137.2.0171.

Kriaa, A., Hamdi, N., and Srasra, E., 2009, Proton adsorption and acid-base properties of Tunisian illites in aqueous solution: Journal of Structural Chemistry, v. 50, p. 273-287, https://doi.org/10.1007/s10947-009-0039-6.

Liu, Y., Alessi, D.S., Flynn, S.L., Alam, M.S., Hao, W., Gingras, M., Zhao, H., and Konhauser, K.O., 2018, Acid-base properties of kaolinite, montmorillonite and illite at marine ionic strength: Chemical Geology, v. 483, p. 191-200, https://doi.org/10.1016/j.chemgeo.2018.01.018.

Loyd, S. J., Marenco, P. J., Hagadorn, J. W., Lyons, T. W., Kaufman, A. J., Sour-Tovar, F., and Corsetti, F. A., 2012, Sustained low marine sulfate concentrations from the Neoproterozoic to the Cambrian: Insights from carbonates of northwestern Mexico and eastern California: Earth and Planetary Science Letters, v. 339-340, p. 79-94, https://doi.org/10.1016/j.epsl.2012.05.032.

Meister, P., 2013, Two opposing effects of sulfate reduction on carbonate precipitation in normal marine, hypersaline, and alkaline environments: Geology, v. 41, p. 499-502, https://doi.org/10.1130/g34185.1.

Michalopoulos, P., and Aller, R. C., 1995, Rapid Clay Mineral Formation in Amazon Delta Sediments: Reverse Weathering and Oceanic Elemental Cycles: Science, v. 270, p. 614, https://doi.org/10.1126/science.270.5236.614.

Raiswell, R., and Fisher, Q. J., 2000, Mudrock-hosted carbonate concretions: A review of growth mechanisms and their influence on chemical and isotopic composition: Journal of the Geological Society, v. 157, p. 239-251, https://doi.org/10.1144/jgs.157.1.239.

Reimers, C.E., Ruttenberg, K.C., Canfield, D.E., Christiansen, M.B., and Martin, J.B., 1996, Porewater pH and authigenic phases formed in the uppermost sediments of the Santa Barbara Basin: Geochimica et Cosmochimica Acta, v. 60, p. 4037-4057, https://doi.org/10.1016/S0016-7037(96)00231-1.

Schoonheydt, R.A., and Johnston, C.T., 2013, Surface and interface chemistry of clay minerals, *in* Faiza, B., and Gerhard, L., eds., Developments in Clay Science: Handbook of Clay Science, Elsevier, p. 139-172, https://doi.org/10.1016/B978-0-08-098258-8.00005-5.

Schrag, D. P., Higgins, J. A., Macdonald, F. A., and Johnston, D. T., 2013, Authigenic carbonate and the history of the global carbon cycle: Science, v. 339, p. 540, https://doi.org/10.1126/science.1229578.

Sposito, G., Skipper, N. T., Sutton, R., Park, S.-h., Soper, A. K., and Greathouse, J. A., 1999, Surface geochemistry of the clay minerals: Proceedings of the National Academy of Sciences, v. 96, p. 3358-3364, https://doi.org/10.1073/pnas.96.7.3358.

Stumm, W., 1992, Chemistry of the Solid-Water Interface: Processes at the Mineral-Water and Particle-Water Interface in Natural Systems, John Wiley & Sons, Inc., 448 p.

Sun, X., and Turchyn, A. V., 2014, Significant contribution of authigenic carbonate to marine carbon burial: Nature Geoscience, v. 7, p. 201, https://doi.org/10.1038/ngeo2070.

Tombácz, E., Nyilas, T., Libor, Z., and Csanaki, C., 2004, Surface charge heterogeneity and aggregation of clay lamellae in aqueous suspensions, *in* Zrinyi, M., and Horvolgyi, Z.D., eds., From Colloids to Nanotechnology: Progress in Colloid and Polymer Science: Berlin, Heidelberg, Springer, p. 206-215, https://doi.org/10.1007/978-3-540-45119-8_35.

Zeng, Z., and Tice, M. M., 2014, Promotion and nucleation of carbonate precipitation during microbial iron reduction: Geobiology, v. 12, p. 362-371, https://doi.org/10.1111/gbi.12090.

3. HYDROMECHANICAL EFFECTS OF MICROORGANISMS ON FINE-GRAINED SEDIMENTS DURING EARLY BURIAL

3.1. Abstract

Microorganisms are known to change fluid flow and permeability processes in subsurface environments, but this has only been demonstrated for coarse-grained sediments and fractures. For fine-grained sediments (mudstones), little is known about the effects of microorganisms on hydromechanical properties. Here, we investigated the influence of microorganisms on the porosity, permeability, and compressibility of fine-grained sediments. We performed resedimentation experiments with and without microorganisms added to two reconstituted, fine-grained sediment samples. These sediments were collected from the Ursa and Brazos-Trinity Basins in the Gulf of Mexico during Integrated Ocean Drilling Program Expedition 308. Microorganisms caused a systematic, yet small increase in compression index for both sediments. Changes to permeability caused by microorganisms, while relatively minor, were greater for the Ursa sediment than the Brazos-Trinity sediment. Additionally, the effect of microorganisms on permeability is greater at higher porosities and lower vertical effective stresses. Differences in permeability behavior between the two sediments are likely due to differences in sediment properties and nutrients for microbial growth. We therefore suggest that the effectiveness of microorganisms at altering fluid flow in fine-grained sediments is dependent on burial depth (porosity as a function of vertical effective stress) and the grain size, pore and pore throat size, and specific surface area of

a sediment. Characterizing the effects of microorganisms on the hydromechanical properties of fine-grained sediments can further our understanding of the controls on pore pressure near the sediment-water interface in marine environments and aid in bioclogging practices around contaminated sites in terrestrial environments.

3.2. Introduction

Microorganisms (bacteria and archaea) are ubiquitous in marine and terrestrial sediments (e.g., Delgado-Baquerizo et al., 2018; Francis et al., 2005). In fact, active microbial cells have been found to thrive in sediments at burial depths down to a few thousand meters (Inagaki et al., 2015; Onstott et al., 1998). However, in general, the concentration of microbial cells is highest near the sediment-water interface in marine sediments or the sediment-air interface in terrestrial sediments and decreases with increasing depth (D'Hondt et al., 2004; Parkes et al., 1994; Pedersen et al., 1996). Thus, any interactions between microorganisms and sediments are decreased at greater depths and stresses (Rebata-Landa & Santamarina, 2006).

In sediments and fractures, microorganisms produce biofilms composed of cells and extracellular polymeric substance (EPS; Flemming & Wingender, 2010), which can affect fluid flow properties by clogging pore space (e.g., Ivanov & Chu, 2008). Biofilms have been shown to decrease permeability or hydraulic conductivity—which is directly proportional to permeability assuming constant fluid density and viscosity—by one to three orders of magnitude in coarse-grained sediments such as sands and silts (Brydie et al., 2005; Taylor & Jaffé, 1990; Zhong & Wu, 2013) and fractures (Cheng et al., 2021; Hill & Sleep, 2002; Ross et al., 2001). While these previous studies from the

geotechnical engineering community have focused on bioclogging in sand-size sediments, the incorporation of clay-size particles into bioclogging studies has only been performed with subordinate amounts of clay-size particles (<15 wt.%) in sediments dominated by the sand-size fraction (e.g., Glatstein & Francisca, 2014; Seki et al., 1998).

The geological and geotechnical engineering communities have extensively studied the compression and permeability behaviors of fine-grained sediments, such as mudstones (Hart et al., 1995; Neuzil, 2019; Reece, 2021; Rubey & Hubbert, 1959; Skempton, 1970; Terzaghi, 1943; Yang & Aplin, 2004). Mudstones exhibit a dramatic decline in porosity within the first several hundred meters of burial followed by a gradual decline through deeper burial (Dzevanshir et al., 1986; Ingebritsen et al., 2006; Mondol et al., 2007). Additionally, the compressibility (rate of porosity loss with effective stress) of a mudstone is dependent on its grain size, grain shape, stress history, and clay mineralogy, with clay-rich mudstones being more compressible (more porosity loss) than silt-rich mudstones (Dewhurst et al., 1998; Reece, 2021). This decrease in porosity with progressive burial results in a decrease in mudstone permeability, where porosity and permeability have a log-linear relationship (e.g., Neuzil, 1994, 2019; Reece et al., 2012; Schneider et al., 2011). However, the effects of microorganisms on the compression behavior of fine-grained sediments are poorly constrained (Daniels et al., 2009) and their effects on the permeability of fine-grained sediments are unexplored.

Here, we investigate the influence of microorganisms on the compression and permeability behavior of fine-grained sediments (mudstones). This is done by performing resedimentation experiments where we measure porosity, permeability, and

compressibility as a function of vertical effective stress for fine-grained sediments of varying compositions with and without added microorganisms. We show that, in contrast to coarse-grained (sandy) sediments, microorganisms do not greatly affect porosity, permeability, and compressibility in fine-grained sediments. Moreover, the relative effects of microorganisms on sediment permeability are dependent on sediment porosity, grain size, pore and pore throat size, and specific surface area. Our results are of importance to both the geological and geotechnical engineering communities as we expand the known controls on the effectiveness of microorganisms to affect fluid flow in marine and terrestrial environments.

3.3. Geologic Background

The sediment samples used in this study were collected from the Gulf of Mexico during Integrated Ocean Drilling Program (IODP) Expedition 308, which sailed in 2005. Two regions of the Gulf of Mexico were sampled and logged during this expedition (Figure 3.1) in order to characterize subsurface fluid flow and overpressure on the continental slope (Flemings et al., 2006). These regions include the Ursa Basin located ~230 km south-southeast of New Orleans, Louisiana and the Brazos-Trinity Basin IV located ~250 km south-southeast of Houston, Texas (Figure 3.1; Flemings et al., 2006). Three sites were drilled each in the Ursa Basin (U1322, U1323, and U1324) and in the Brazos-Trinity Basin IV (U1319, U1320, and U1321; Flemings et al., 2006). This study focuses only on sediments from Sites U1324 (Hole B) and U1319 (Hole A).

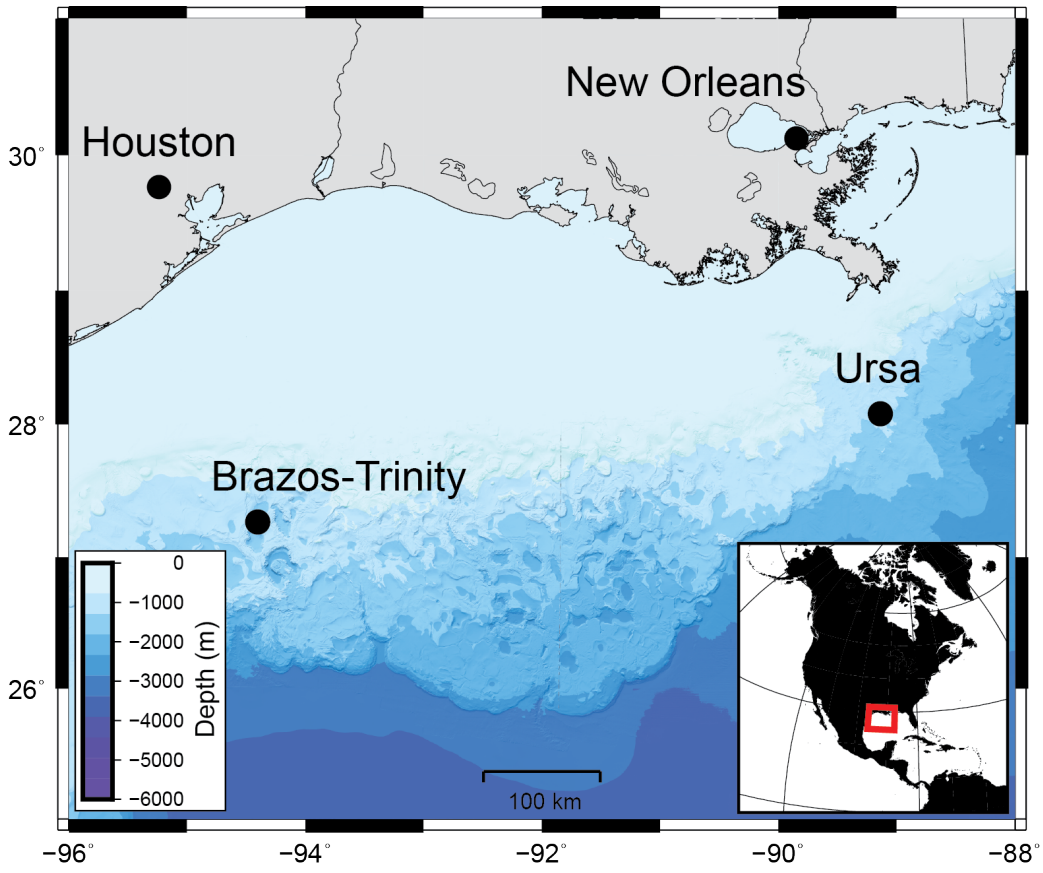

Figure 3.1 Bathymetry map showing the locations of the Ursa and Brazos-Trinity sediments obtained from the Gulf of Mexico during IODP Expedition 308.

At Site U1324 (Ursa Basin), two lithostratigraphic units are present. Unit I is composed of hemipelagic and turbidite levee clay and mud with intervals of mass transport deposits between 0–364.7 m below sea floor (mbsf; Holocene–late Pleistocene) and unit II is composed of interbedded sand and silt mass transport deposits with mud overbank deposits between 364.7–600.8 mbsf (late Pleistocene; Flemings et al., 2006). Cell counts of microorganisms are highest ($2x10^5$ cells/cm^3_{total}; at a porosity of 0.75) near the seafloor, decrease to $1x10^4$ cells/cm^3_{total} (at a porosity of 0.50) at 100 mbsf, and

are below the detection limits used at the time of sampling for the remainder of the cored profile (Flemings et al., 2006).

At Site U1319 (Brazos-Trinity IV Basin), six lithostratigraphic units are present: (1) unit I, foraminifera-bearing hemipelagic clays between 0–3.3 mbsf (Holocene–late Pleistocene); (2) unit II, hemipelagic muds and thin turbidite and mass transport deposits between 3.3–17.3 mbsf (late Pleistocene); (3) unit III, hemipelagic microfossil-bearing clays between 17.3–23.5 mbsf (late Pleistocene); (4) unit IV, hemipelagic clay and fine sand turbidite deposits between 23.5–29.5 mbsf (late Pleistocene); (5) unit V, hemipelagic nannofossil- and foraminifera-bearing clays between 29.5–31.0 mbsf (late Pleistocene); and (6) unit VI, bioturbated clays deposited by muddy plumes or nepheloid layers between 31.0–155.8 mbsf (late Pleistocene; Flemings et al., 2006). Cell counts of microorganisms near the seafloor of Site U1319 are one order of magnitude higher ($1.2x10^6$ cells/cm^3_{total}; at a porosity of 0.78) than at Site U1324, but then also decrease to $1x10^4$ cells/cm^3_{total} (at a porosity of 0.50) at ~100 mbsf, and are below the detection limits used at the time of sampling for the remainder of the cored profile (Flemings et al., 2006).

3.4. Materials and Methods

3.4.1. Materials

Two natural bulk mudstone powders were prepared using IODP sediments collected from the Ursa Basin (Site U1324) and the Brazos-Trinity Basin IV (Site U1319). We refer to these homogenized sediments as either the Ursa sediment or the Brazos-Trinity sediment, respectively. The Ursa sediment comes from two distinct

lithostratigraphic units: (1) 1.2 kg of hemipelagic muds from lithostratigraphic unit I (subunit IA) at depths of 4–32 mbsf and (2) 0.8 kg of silt and mud overbank deposits from lithostratigraphic unit II (subunit IIC) at depths of 493–502 mbsf (Appendix C). The Brazos-Trinity sediment comes from lithostratigraphic unit II (subunits IIA, IIB, and IIC) and is composed of 1.9 kg of hemipelagic muds with thin turbidite and mass transport deposits at depths of 4–13 mbsf. After collection, the samples were individually air-dried, disaggregated into clay- and silt-size particles, and homogenized into these two distinct bulk mudstone powders.

3.4.2. Material Characterization

We characterized the dry bulk sediment powders by determining Atterberg limits, particle size distribution, and mineralogy. The Atterberg limits are known as consistency limits and are used to describe the plasticity and mechanical strength of a soil or unconsolidated mudstone. The plastic limit (*PL*) is the critical water content at which the soil or sediment changes from the semi-solid to the plastic state, and is determined using the hand roll method as specified in ASTM D4318-17 (ASTM International, 2017). The liquid limit (*LL*) is the critical water content that marks the boundary between the plastic and liquid states, and it is determined using the Casagrande cup and multipoint method as specified in ASTM D4318-17 (ASTM International, 2017). The plasticity index (*PI*) is defined as the difference between the *LL* and the *PL* and defines the range of water contents over which the unconsolidated fine-grained sediment or soil behaves plastically.

Particle size analysis is carried out using the hydrometer method as specified by ASTM D7928 (ASTM International, 2017). This method utilizes principles from Stoke's law, namely that larger and denser particles fall out of a sediment suspension faster than smaller and less dense particles. A sediment suspension is created by mixing ~50g of sediment, 5g of sodium hexametaphosphate (dispersant), and nanopure water. After hydrating the sediment for 24 hours, the suspension is poured into a graduated cylinder and water is used to bring the total volume to 1000mL. The suspension is then vigorously mixed and timed sedimentation begins. A hydrometer is inserted into the suspension to measure specific gravity at discrete points in elapsed time. Results of hydrometer tests are given as the percent of particles in the suspension that are finer than any given particle size.

The mineralogy of the dry sediment powders is determined by X-ray diffraction (XRD). The whole rock and clay fraction (particles <2μm) XRD analyses were performed using a Bruker D8 Advance X-ray diffractometer with a CuKα source (λ=0.154 nm) operating at 40 kV and 40 mA. The whole rock XRD patterns were recorded from 2-70° 2θ with a dwell time of 3° 2θ per minute. To obtain the clay fraction, the bulk sample was first pretreated with 1 M sodium acetate at a pH of 5 in an 80°C water bath and 30% hydrogen peroxide to remove all carbonate minerals and organic matter, respectively. The clay fraction was then obtained via centrifugation after deflocculation and Na saturation with Na_2CO_3. Salts in the resultant clay fraction suspension were removed by dialysis. The clay fraction was then treated with Mg and K separately and transferred to their respective glass slides for analysis. Clay fraction XRD

patterns were recorded from 2-32° 2θ with a dwell time of 3° 2θ per minute. These XRD spectra were recorded in the air-dried state, after the Mg saturated sample was treated with glycerol, and after the K saturated sample had been heated to 330°C and 550°C. Semi-quantitative analysis was performed using the reference intensity ratio method for the bulk mineralogy and the mineral intensity factor method for the <2μm fraction.

3.4.3. Resedimentation

Resedimentation experiments are used to replicate natural burial processes of fine-grained sediments (e.g., Reece, 2021; Santagata & Kang, 2007; Schneider et al., 2011) and follow the procedure of a traditional oedometer test (ASTM D2435; ASTM International, 2020). We use this technique because it allows us to control the stress conditions acting on a mudstone, create a replicable mudstone sample, eliminate sample disturbance, isolate variables affecting consolidation, and perform a systematic study to address fundamental research questions.

The first step in the resedimentation process is to mix a dry mudstone powder with a pore fluid solution (explained below) to create a stable and homogeneous slurry. Water contents of 102% and 105% for the Ursa and Brazos-Trinity sediments, respectively, were identified to ensure stable slurries without gravimetric settling. The slurry is then poured into a consolidometer and incrementally, uniaxially loaded with weights to a maximum applied vertical stress of 100 kPa using a load increment ratio of 2 (10 total increments). We loaded the slurry for 2 days each during increments 1–9 and for 4 days during increment 10 to reach end of primary consolidation. As the slurry is loaded, the pore fluids are allowed to drain through filter paper and porous stones above

and below the sample. The slurry is then unloaded to an overconsolidation ratio of 4 (~25 kPa) following the increment of maximum stress. Upon completion, the sample can be extruded as a cohesive, intact mudstone. A linear displacement transducer is added during increment 4 and used to continuously measure the vertical displacement of the sample throughout compression. Given no lateral strain, this allows us to calculate void ratio (porosity), permeability, and compressibility at discrete points in the experiment using the Log of Time theory (ASTM D2435; ASTM International, 2020). The final void ratio is measured on a subsample of the extruded mudstone using the wet and dry mass technique (Blum, 1997).

We performed resedimentation experiments with microorganisms (biotic) and without microorganisms (control) mixed into the slurry, and all experiments were performed in an anaerobic chamber containing 80% N_2, 15% CO_2, and 5% H_2. Before biotic or control experiments were performed, the utensils, pouring apparatus, and pieces of the resedimentation apparatus that come in contact with the slurry were sterilized either by autoclave or by wiping with 70% ethanol under UV light in a laminar flow hood.

In the biotic experiments, we used the iron reducing bacteria *Shewanella oneidensis* MR-1 at two different cell concentrations (referred to as biotic 1x and biotic 4x) in the Ursa and Brazos-Trinity sediments. The *Shewanella* were cultured for 24 h in autoclaved Lysogeny Broth (LB) medium (10 g/L tryptone, 5 g/L yeast extract, 10 g/L NaCl) and subsequently harvested via centrifugation and washed. Original cell counts were made by adjusting the cell solution to an optical density of 1.0 at a wavelength of

600 nm using a Beckman Coulter DU 730 spectrophotometer, which yields ~$8x10^8$ cells/mL (Zeng & Tice, 2018). We admixed cells into the mudstone slurries at a concentration of ~$2.5x10^8$ cells/cm^3_{solids} (volume of solids) for the biotic 1x experiments and at an increased concentration (~4 times the cells/cm^3_{solids}) of ~$1.0x10^9$ cells/cm^3_{solids} for the biotic 4x experiments. The control experiments had no cells added.

The pore fluid used to make mudstone slurries was designed to be a basal medium to support *Shewanella* growth, and as a result it had a lower ionic strength than seawater. The medium is modified from Marsili et al. (2008) and Zeng and Tice (2014) and is composed of 0.0174 g/L K_2HPO_4, 0.123 g/L $MgSO_4 \cdot 7H_2O$, 0.227 g/L $(NH_4)_2SO_4$, 0.535 g/L NH_4Cl, 1.47 g/L $CaCl_2 \cdot 2H_2O$, 0.5 g/L casamino acid, 3.73 mL/L Na DL-lactate (electron donor), and 5 mM $Fe(OH)_3$ (electron acceptor). The $Fe(OH)_3$ was prepared fresh by adjusting a solution of 0.17 M $FeCl_3$ to a pH of 7 with 5 M NaOH (Q. S. Fu et al., 2008). The pore fluid medium was filter-sterilized, equilibrated in the anaerobic chamber, and the pH was adjusted to ~7.0.

During resedimentation experiments, the effluent pore fluid was collected at the bottom of the specimen to measure pH and the concentration of Fe^{2+}. The pH was measured with a Fisherbrand accumet micro pH electrode (model 13-620-850) and the concentration of Fe^{2+} was measured using the ferrozine assay (Viollier et al., 2000). All steps for these measurements were performed immediately after collection (within <5 minutes) and inside the anaerobic chamber except the reading of final absorbance values for the ferrozine assay, which were collected using a BioTek ELx800 microplate reader.

3.4.4. Final Cell Counts

Direct cell counts were performed, following the techniques in Monteverde et al. (2018), using subsamples of the extruded mudstones after each resedimentation experiment. To do this, we took a 1 mL cell suspension—created using 8 mL of formalin and a 2 cm^3_{total} (total volume) mudstone subsample—and mixed it with 2.2 mL of 2.5% NaCl, 400 μL of detergent solution (composed of 100 mM EDTA, 100 mM sodium pyrophosphate, 1% (v/v) tween-80), and 400 μL of methanol. This solution was shaken at 500 rpm for 10 minutes and then centrifuged at 3000 g for 5 minutes to pellet the sediment. We then mixed 1425 μL of the supernatant with 75 μL of DAPI, a DNA-binding fluorescent dye, let the mixture equilibrate for 5 minutes in the dark, and vacuum filtered the mixture onto 0.2 μm black polycarbonate filters. The filters were then mounted on glass slides and the cells were counted using epifluorescence light on a Zeiss Axio Imager.M2 at 1000x magnification. The biotic 1x and biotic 4x samples were each counted until at least 200 total cells were observed (~30–40 fields of view). Alternatively, cells were counted in ~50 fields of view for the control samples, while not reaching 200 total cells, due to lower cell concentrations. Once the cells had been counted, we converted the concentrations from cells/cm^3_{total} (total volume) to cells/cm^3_{solids} (volume of solids) using the final void ratio data from each resedimentation experiment. This was required to account for differences in porosity between the beginning and end of resedimentation tests.

3.4.5. Microscale Imaging

After the resedimentation experiments had been completed, subsamples of the extruded mudstones were taken for scanning electron microscopy (SEM). The subsamples were taken parallel to the applied vertical stress using a standard drinking straw (mini-coring technique; Lavoie et al., 1996), which were subsequently cut into 1–3 mm slices using a razor blade. These 1–3 mm slices were then immersed in 2% agarose at ~37°C and then cooled at ~4°C to solidify the agarose. We then used the resin embedding method developed by Uramoto et al. (2014) to replace the pore fluids with resin. First, this consisted of sequentially soaking the subsamples in 2.5% glutaraldehyde, 2% osmium tetroxide, and 1% uranyl acetate for 3 hours each at ~4°C with washings in between. The subsamples were then dehydrated using a series of solutions with increasing ethanol concentrations (between 30% and 100%). The ethanol was then replaced with n-butyl glycidyl ether (QY-1) and the QY-1 was subsequently replaced with Quetol 651 resin (details in Uramoto et al., 2014). After curing for 24 hours at 60°C, the subsamples were cut and then polished using oil-based aluminum oxide grits. The polished subsamples were coated in gold and backscatter electron (BSE) images were taken using a TESCAN VEGA 3 scanning electron microscope (SEM). Images were only taken for the end-member resedimentation experiments, i.e., control and biotic 4x tests.

3.5. Results

3.5.1. Material Characterization

Atterberg limits results show that *LL*, *PL*, and *PI* are 59%, 20% and 39% for the Ursa sediment and 71%, 23%, and 48% for the Brazos-Trinity sediment, respectively (Figure 3.2a). Atterberg limits were performed in duplicate, with water content errors for both samples being <0.5%, and their results are presented as averages. Both sediment samples are classified as high plasticity clays (Figure 3.2a). Hydrometer tests for the Ursa sediment yielded an average of 59% of particles finer than 2μm (by mass), while the Brazos-Trinity sediment yielded an average of 65% of particles finer than 2μm (by mass; Figure 3.2b). The hydrometer tests were also performed in duplicate, with the error of the percent of particles finer than 2μm for both samples being <1.5%. Because two hydrometer tests cannot be easily averaged, we display both hydrometer tests for each sediment sample in Figure 3.2b. The bulk mineralogy of both the Ursa and Brazos-Trinity sediments are dominated by quartz and clay minerals, with subordinate amounts of feldspar, calcite, and dolomite (Figures 3.2c and 3.2d). In the <2μm fraction, the Ursa sediment contains more illite than smectite and the Brazos-Trinity sediment contains more smectite than illite (Figures 3.2c and 3.2d). The hydrometer and mineralogy data for the Ursa sediment were previously published in Mills et al. (2021), where this sediment was referred to as the Gulf of Mexico sediment.

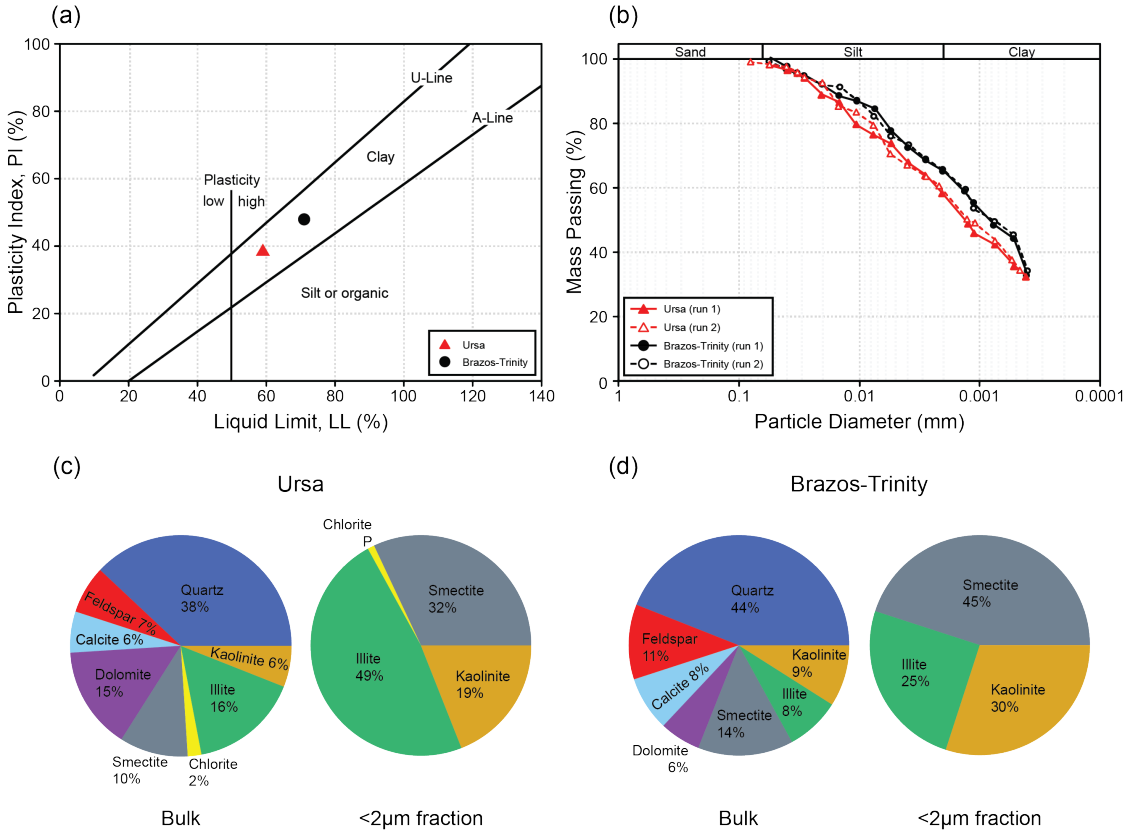

Figure 3.2 Material characterization results for the Ursa and Brazos-Trinity sediments. (a) Plasticity chart showing Atterberg limits results. (b) Particle size distributions from hydrometer tests. Both hydrometer tests for each sediment sample are shown because two tests for the same sample cannot easily be averaged without interpolation due to measurements at different particle size diameters. (c) Bulk and clay-size fraction (<2µm) mineralogy for the Ursa mudstone powder. (d) Bulk and clay-size fraction (<2µm) mineralogy for the Brazos-Trinity mudstone powder. P = present but not quantified.

3.5.2. Compression and Permeability Behavior

Compression curves for the Ursa and Brazos-Trinity sediments with bacteria (biotic 1x and biotic 4x) and without bacteria (control) display similar trends: void ratio (e; $e=n/(1-n)$, where n is porosity) linearly decreases with increasing logarithm of vertical effective stress (σ'_v; Figure 3.3a). This compression trend follows the commonly

observed behavior in sediments during burial (Burland, 1990; Skempton, 1970; Terzaghi, 1943), which can be modeled with the equation:

$$e = e_0 - C_c log_{10}\left(\frac{\sigma_v'}{\sigma_0'}\right), \qquad \text{(Eq. 3.1)}$$

where e_0 and σ'_0 are empirically derived parameters and the compression index (C_c) is the slope of the compression line. Here, we define σ'_0 at 1 kPa and constrain C_c over a vertical effective stress range of 2.5–100 kPa. While both of these sediments display similar compression trends, they show distinct ranges of e and C_c values (Figure 3.3a). The initial void ratios measured at σ'_v of 2.5 kPa (e_i) for the Ursa sediment range between 2.15–2.23 and void ratios decrease with added stress down to 1.17–1.21 at σ'_v of 100 kPa (Figure 3.3a; Table 3.1). For the Brazos-Trinity sediment, e_i values range between 2.36–2.48 and void ratios decrease with added stress down to 1.34–1.35 at σ'_v of 100 kPa (Figure 3.3a; Table 3.1). Compression indices, determined by fitting the e–log(σ'_v) model (Equation 3.1) to the data, range between 0.60–0.66 and between 0.64–0.72 for Ursa and Brazos-Trinity sediments, respectively (Figure 3.3b; Table 3.1). The lower C_c values for the Ursa sediment indicate that this sediment is stiffer than the Brazos-Trinity sediment. In contrast, the expansion indices (C_e; slope between e and log(σ'_v) during the unloading phase of the resedimentation experiments) for both sediments fall within a similar range (~0.05-0.06; Figure 3.3a; Table 3.1).

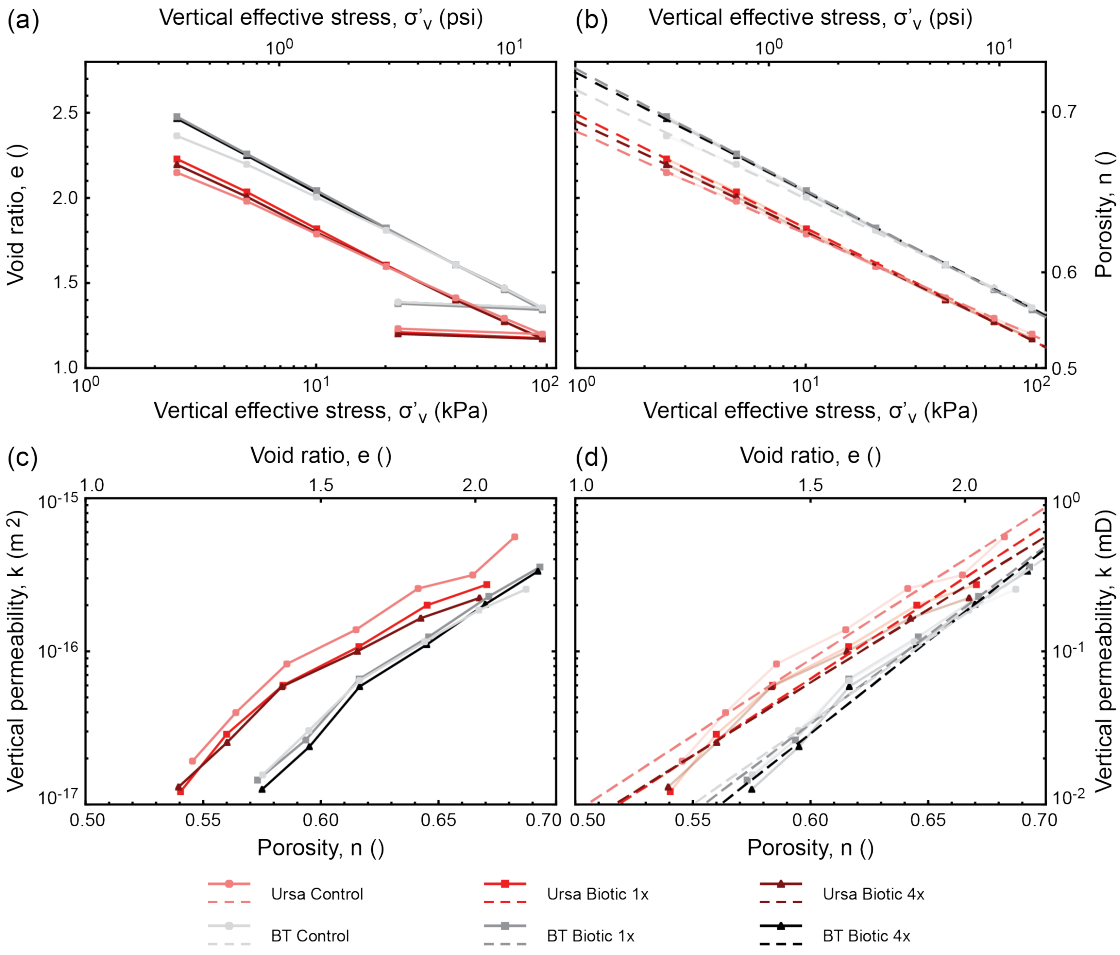

Figure 3.3 (a and b) Compression and (c and d) permeability – porosity behavior of the Ursa and Brazos-Trinity sediments for control, biotic 1x, and biotic 4x circumstances. Measured compression and permeability – porosity data (markers and solid lines) are displayed in (a) and (c), respectively. The best fit lines (dashed lines) from the compression and permeability – porosity models (Equations 3.1 and 3.2) are displayed in (b) and (d), respectively. Modeled compression (e_0 and C_c) and permeability – porosity (γ and k_0) fitting parameters are presented in Table 3.1 for each resedimentation test. The measured data were obtained during resedimentation increments 4–10. BT = Brazos-Trinity.

Table 3.1 Compression and permeability results from the Ursa and Brazos-Trinity resedimentation experiments for control, biotic 1x, and biotic 4x circumstances. e_0 = void ratio at a vertical effective stress of 1 kPa, e_i = first measured void ratio at a vertical effective stress of 2.5 kPa, C_c = compression index (constrained over vertical effective stresses of 2.5 and 100 kPa), C_e = expansion index (constrained over vertical effective stresses of 25 and 100 kPa), γ = fitted slope of the (log)permeability – porosity relationship, log(k_0) = the fitted intercept of the (log)permeability – porosity relationship at a porosity of 0, R^2 = coefficient of determination.

		Compression					Permeability		
Sample	Test	e_0 (-)	e_i (-)	C_c (1/kPa)	R^2 (for C_c)	C_e (1/kPa)	γ (m^2)	R^2 (for γ)	$log(k_0)$ (m^2)
Ursa	Control	2.39	2.15	-0.60	0.999	-0.051	9.94	0.975	-22.02
	Biotic 1x	2.50	2.23	-0.66	0.999	-0.057	10.05	0.965	-22.21
	Biotic 4x	2.45	2.20	-0.65	0.999	-0.047	9.54	0.965	-21.93
Brazos-Trinity	Control	2.64	2.36	-0.64	0.999	-0.053	10.76	0.979	-22.92
	Biotic 1x	2.76	2.48	-0.72	1.000	-0.059	11.06	0.987	-23.44
	Biotic 4x	2.74	2.47	-0.70	0.999	-0.054	12.09	0.986	-23.79

The addition of bacteria slightly changes the compression behavior of the Ursa and Brazos-Trinity sediments. For both sediments, e_i is increased and e at 100 kPa is decreased with the addition of bacteria. These changes result in increasing C_c values with additions of bacteria during resedimentation tests (Figure 3.3b; Table 3.1). Specifically, for both sediments, C_c increases by ~0.06 from the control resedimentation test to both biotic resedimentation tests, which had similar C_c values (Figure 3.3b; Table 3.1). The varying e_i and C_c values result in a crossover of compression curves for the Ursa and Brazos-Trinity sediments at σ'_v values of ~30 kPa and ~40 kPa, respectively

(Figures 3.3a and 3.3b). The C_e values for both sediments show no trends between the control, biotic 1x, and biotic 4x experiments (Figure 3.3a; Table 3.1).

The permeability – porosity behavior of the Ursa and Brazos-Trinity sediments with and without bacteria display similar trends: the permeability decreases logarithmically as porosity decreases (Figure 3.3c). This permeability – porosity relationship is commonly observed in mudstones during burial (e.g., Neuzil, 1994, 2019; Reece et al., 2012; Schneider et al., 2011), and it can be modeled with the equation:

$$log_{10}(k) = \gamma\, n + log_{10}(k_0)\ , \qquad \text{(Eq. 3.2)}$$

where γ is the slope and k_0 is the permeability at a porosity of 0. Both sediments display distinct ranges in permeability for a given porosity (Figure 3.3c; Table 3.1). Measured permeabilities of the Ursa sediment range between $5.6\text{x}10^{-16}$–$1.2\text{x}10^{-17}$ m^2 for a respective porosity range of 0.68–0.54, while measured permeabilities of the Brazos-Trinity sediment range between $3.5\text{x}10^{-16}$–$1.3\text{x}10^{-17}$ m^2 for a respective porosity range of 0.69–0.57 (Figure 3.3c). The γ values, determined by fitting the log-linear permeability – porosity model (Equation 3.2) to the data, range between 9.54–10.05 and 10.76–12.09 for the Ursa and Brazos-Trinity sediments, respectively (Figure 3.3d; Table 3.1). Similarly, log(k_0) values for the Ursa and Brazos-Trinity sediments range between 21.93–22.21 and between 22.92–23.79, respectively (Table 3.1).

The addition of bacteria influenced the permeability values at a given porosity for the Ursa sediment, while the addition of bacteria had little to no influence on the permeability of the Brazos-Trinity sediment (Figure 3.3c). For the Ursa sediment, the measured permeabilities at high porosities (~0.65) in the biotic 1x and biotic 4x tests are

1.3 and 1.5 times lower than that of the control test, respectively (Figure 3.3c). This difference is reduced at lower porosities (~0.55) where the permeabilities of both the biotic 1x and biotic 4x tests are 1.2 times lower than that of the control test (Figure 3.3c). For the Brazos-Trinity sediment, the measured permeability values are similar for the control, biotic 1x, and biotic 4x tests at high porosities (Figure 3.3c). In fact, the control sample has a lower permeability than the biotic 1x and biotic 4x samples between porosities of 0.65 and 0.69 (Figure 3.3c). However, below a porosity of 0.65, the biotic 4x sample has a lower permeability than that of the biotic 1x sample, which has only slightly lower or similar permeabilities as the control sample (Figure 3.3c). At a porosity of ~0.59, the permeability of the biotic 4x sample is 1.2 times lower than that of the biotic 1x and control samples, similar to the Ursa data at lower porosities (Figure 3.3c). The fitting parameters γ and k_0 show no trends for the Ursa resedimentation tests (Figure 3.3d; Table 3.1). For the Brazos-Trinity tests, γ increases and the logarithmic value of k_0 decreases from control to biotic 1x to biotic 4x (Figure 3.3d; Table 3.1).

3.5.3. Scanning Electron Microscopy

The microstructure of the Ursa and Brazos-Trinity sediments under control and biotic 4x conditions (lowest and highest concentrations of added bacterial cells) was investigated using backscatter electron (BSE) images. In general, both sediments display similar microstructures between their respective control and biotic 4x images (Figure 3.4). Three types of grains can be identified in all samples, including framework grains (quartz, calcite, or feldspar; 4–10 μm in diameter), larger elongate grains (micas or clay minerals; high aspect ratios; 10–30 μm in length), and a clay mineral matrix (<2 μm in

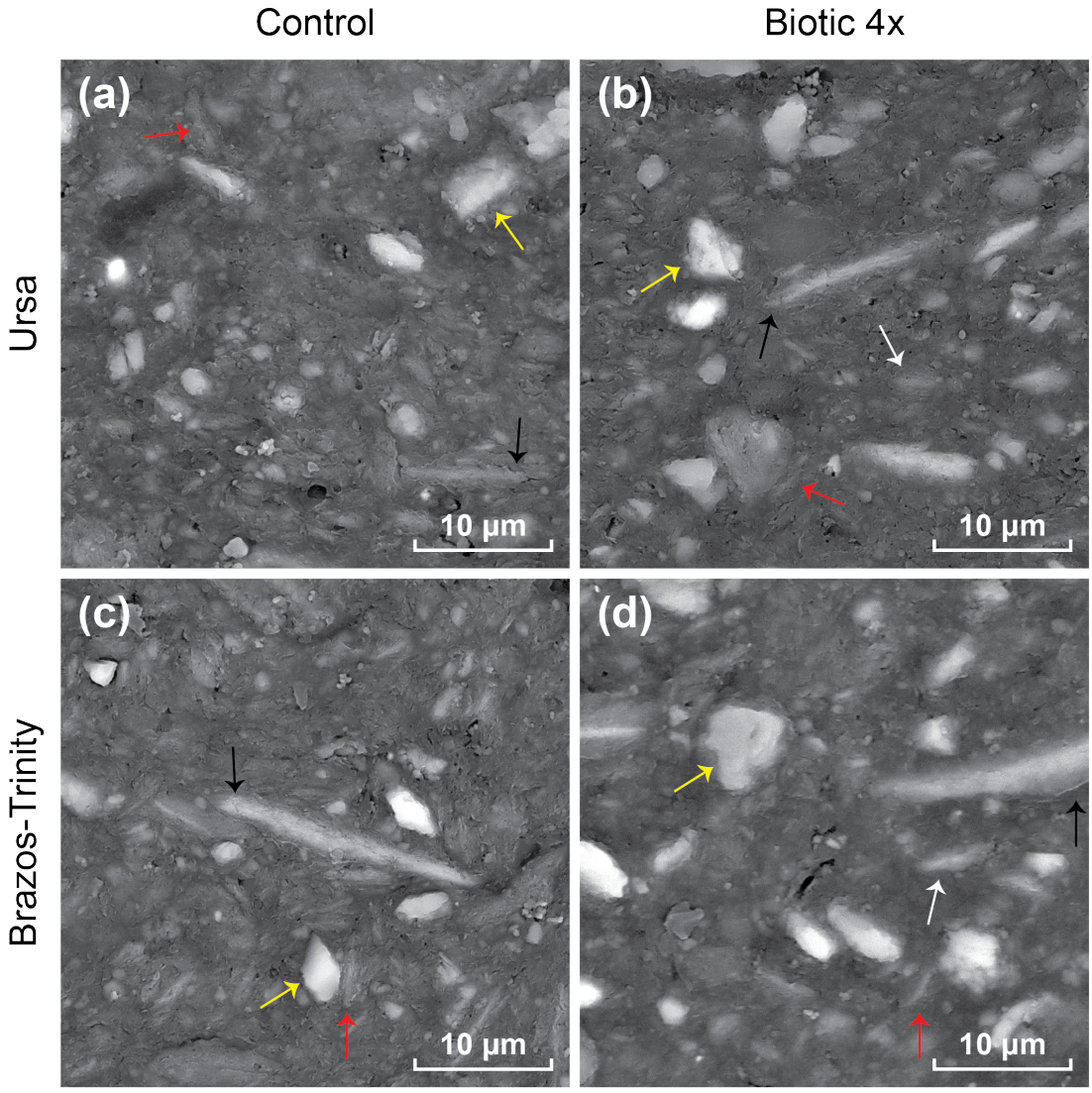

Figure 3.4 BSE-SEM images showing the microstructure of the extruded resedimentation samples after loading to a vertical effective stress of ~100 kPa. (a) Ursa control sample, (b) Ursa biotic 4x sample, (c) Brazos-Trinity control sample, and (d) Brazos-Trinity biotic 4x sample. The images are oriented with the applied load going from top to bottom. Yellow arrows point to framework grains, black arrows point to elongate grains oriented perpendicular to the applied load, red arrows point to elongate grains in the clay matrix that align around framework grains, and white arrows point to diffuse grain boundaries.

length; Figure 3.4). The framework grains (yellow arrows in Figure 3.4) are evenly dispersed throughout both sediments confirming that no settling occurred during resedimentation. In both sediments, larger elongate grains are nearly oriented perpendicular to the direction of the applied vertical stress (black arrows in Figure 3.4), while smaller particles in the clay matrix are oriented in this fashion only far from framework grains (Figure 3.4). However, near framework grains, smaller particles in the clay matrix align around the framework grains (red arrows in Figure 3.4).

The clay matrix in the biotic 4x images for both sediments appears darker (i.e., less electron charging) and the grain boundaries within the clay matrix appear more diffuse (white arrows in Figures 3.4b and 3.4d) than in the control samples. The pore space is difficult to distinguish from the clay matrix for both sediments, especially in the biotic 4x images. This is due to the resin used to solidify the samples. However, our resin embedding method (see section 3.4.5) was necessary to preserve the microstructure of our samples without desiccation and cracking. Despite these limitations, pore sizes appear to be <1 μm in diameter in the clay matrix and between 1–4 μm in diameter adjacent to the larger framework grains. We do not observe any bacteria, biofilms, or precipitates under these sample preparation and imaging conditions.

3.5.4. Pore Fluid Geochemistry and Geomicrobiology

The concentration of Fe^{2+} in the pore fluid effluent is used to monitor bacterial activity and chemical conditions in our resedimentation experiments. As the bacteria used in our biotic resedimentation experiments reduce Fe^{3+} in the form of $Fe(OH)_3$ and oxidize lactate ($CH_3CHOHCOO^-$), Fe^{2+} is produced (e.g., Lovley et al., 1989):

$$4Fe(OH)_3 + CH_3CHOHCOO^- + 7H^+ \rightarrow 4Fe^{2+} + HCO_3^- + CH_3COO^- + 10H_2O\ .$$

(Eq. 3.3)

For the Ursa and Brazos-Trinity sediments, the Fe^{2+} concentrations in the control tests remain low (<0.1 mM) throughout the experiments (Figure 3.5a). In contrast, the Fe^{2+} concentrations in the biotic tests for both sediments initially rise over the first 8–10 days, followed by a subsequent decline over the remainder of the experiments (Figure 3.5a). The biotic 1x and biotic 4x tests from the Ursa sediment reach maximum Fe^{2+} concentrations of 7 mM and 9 mM, respectively, while the biotic 1x and biotic 4x tests from the Brazos-Trinity sediment reach lower maximum Fe^{2+} concentrations of 5 mM for both (Figure 3.5a). Interestingly, the Fe^{2+} concentrations in the biotic 4x tests for both sediments reach their maximum values and subsequently decline to lower values in a shorter period of time than the Fe^{2+} concentrations in the biotic 1x tests for both sediments (Figure 3.5a).

We also monitored bacterial activity and chemical conditions by measuring the change in the effluent pH (ΔpH) from the beginning of each resedimentation experiment. As the bacteria in our biotic resedimentation experiments drive Fe reduction, they increase pore fluid pH via the consumption of H^+ (Equation 3.3). For the Ursa sediment, ΔpH in the control test remains constant throughout the experiment (between 0 and -0.15; Figure 3.5b). In the biotic 1x and biotic 4x tests, ΔpH increases over the first 6 days to respective maximum values of 0.32 and 0.50, slightly drops from days 6 through 10, and then remains constant for the remainder of the experiments (Figure 3.5b). For the Brazos-Trinity sediment, ΔpH in the control test gradually increases throughout the

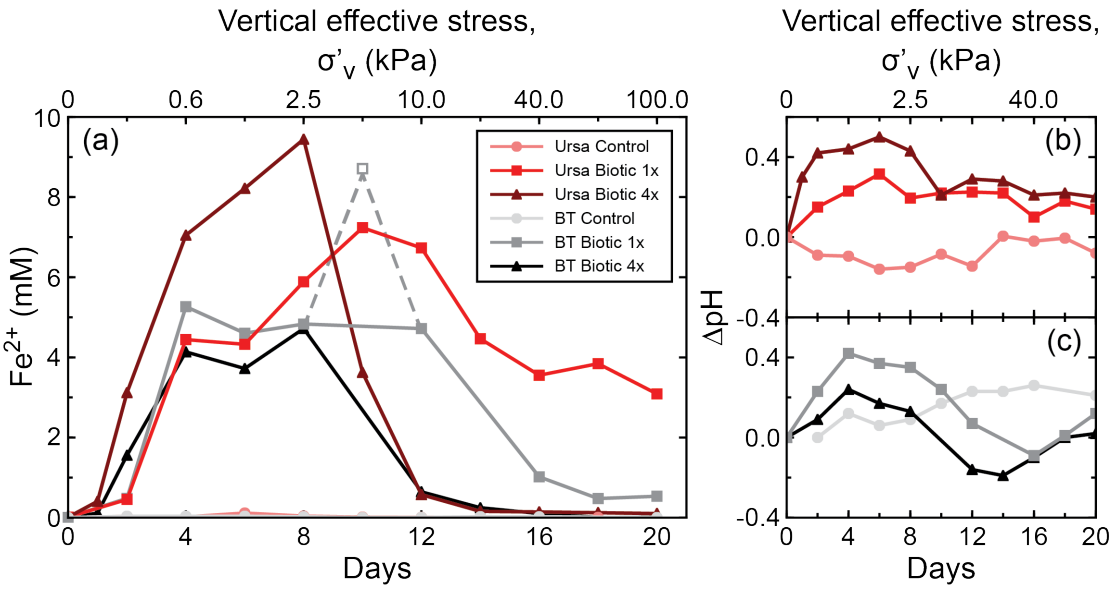

Figure 3.5 Pore-fluid geochemistry results for the Ursa and Brazos-Trinity sediments under control, biotic 1x, and biotic 4x circumstances. (a) The concentration of Fe^{2+} throughout each resedimentation experiment. (b) The ΔpH (change in pH from beginning of each experiment) values for the Ursa control, biotic 1x, and biotic 4x tests. (c) The ΔpH values for the Brazos-Trinity control, biotic 1x, and biotic 4x tests. The open marker indicates a potentially false data point and the dashed lines show the potential trends to and from that data point. These data were obtained during resedimentation increments 1–10. BT = Brazos-Trinity.

experiment from 0 to 0.25 (Figure 3.5c). In the biotic 1x and biotic 4x tests, ΔpH initially increases over the first 4 days to respective maximum values of 0.37 and 0.24, declines from days 4–15 to respective minimum values of -0.1 and -0.2, and then gradually increases for the remainder of the experiments (Figure 3.5c).

The final cell counts from the extruded mudstones, along with initial concentrations of cells inoculated into each resedimentation experiment, are shown in Table 3.2. The final cell counts for the Ursa and Brazos-Trinity sediments yielded over

an order of magnitude more cells/cm^3_{solids} in the biotic 1x tests than the control tests and the biotic 4x tests yielded slightly more cells/cm^3_{solids} than the biotic 1x tests (Table 3.2).

Table 3.2 The initial concentrations of bacterial cells inoculated into each resedimented sample and the results for the final cell counts at the end of each experiment. Cell concentrations are given in cells per volume of solids (cm^3). The volume of solids is the volume comprised of solid particles only. This is to account for porosity differences and allow for direct comparisons between the beginning and end of a resedimentation experiment.

Sample	Test	Inoculation concentration (cells cm^{-3}_{solids})	Final cell count (cells cm^{-3}_{solids})
Ursa	Control	0	$2.29x10^6$
	Biotic 1x	$2.45x10^8$	$2.73x10^7$
	Biotic 4x	$9.80x10^8$	$3.87x10^7$
Brazos-Trinity	Control	0	$2.17x10^6$
	Biotic 1x	$2.52x10^8$	$3.05x10^7$
	Biotic 4x	$1.01x10^9$	$4.34x10^7$

3.6. Discussion

3.6.1. Bacterial Growth

Based on our pore-fluid geochemistry and geomicrobiology measurements, we show that the bacteria used in our experiments respired Fe^{3+} and likely produced biofilms (e.g., Thormann et al., 2004). In the biotic experiments, Fe^{2+} concentrations increased as a result of microbial iron reduction (Figure 3.5). In fact, the bacteria reduced all 5 mM of the seeded $Fe(OH)_3$ in both sediments and an additional 2–4 mM in the Ursa sediment, likely due to preexisting Fe^{3+} in the Ursa sediment (Figure 3.5). The addition of four times the bacterial cells from the biotic 1x to biotic 4x experiments for both sediments resulted in a quicker rise and subsequent fall of Fe^{2+} concentrations

(Figure 3.5). The darker appearance of the clay matrix in the biotic 4x BSE images could perhaps be due to the microbial reduction of $Fe(OH)_3$ causing less electron scattering than in the control images (Figure 3.4). Microbial iron reduction also resulted in an increase in pH that was coincident with increasing Fe^{2+} concentrations (Figure 3.5).

The final cell counts for the control experiments (Table 3.2) are similar to the cell counts obtained from IODP data reports for the Ursa ($6x10^5$ cells/cm^3_{solids}; converted from cells/cm^3_{total} at a porosity of 0.75) and Brazos-Trinity ($4.3x10^6$ cells/cm^3_{solids}; converted from cells/cm^3_{total} at a porosity of 0.78) sites at the depths our sediments were obtained from (see section 3.3). It is likely that these natural cells were largely inactive or dead at the time of our resedimentation experiments, as evidenced by unchanging pH values and Fe^{2+} concentrations (Figure 3.5), due to our sediment preparation and storage techniques (see section 3.4.1). Not only were the added cells in our biotic experiments active (Figure 3.5), but the final cell counts for each biotic experiment (biotic 1x and biotic 4x) were over an order of magnitude higher than those of the control experiments for both sediments (Table 3.2). These geochemical and geomicrobiological data indicate that changes to sediment compression and permeability behavior were due to the addition of bacteria, given that all other parameters were kept constant and only the concentration of bacterial cells was changed between each experiment.

3.6.2. Compression Behavior

Microorganisms cause small, yet systematic changes in compression behavior. The addition of microorganisms results in an increase in C_c but relatively constant C_e for both sediment types (Table 3.1; Figure 3.3), indicating that microorganisms affect the

elasto-plastic behavior of sediments, but not their elastic behavior. Perhaps the increase in C_c is due to microorganisms increasing porosity at lower vertical effective stresses, while at higher effective stresses microbial activity could be limited by the increasing load (e.g., Rebata-Landa & Santamarina, 2006). The observation that sediments become more compressible and less stiff with added microorganisms is consistent with results from Daniels et al. (2009), who showed that C_c values increase with increasing amounts of biofilm for a lean clay (with sand-size grains present) but not for a sand-bentonite mixture (65% sand; 35% bentonite). While their results are inconclusive, our results clarify and affirm that microorganisms increase C_c.

3.6.3. Permeability

Several processes could explain the fact that the addition of microorganisms caused greater absolute changes to permeability at a given porosity for the Ursa sediment than for the Brazos-Trinity sediment (Figures 3.3c and 3.3d). For example, sedimentological and physical property differences between the two sediments could be responsible for this observed behavior. The Brazos-Trinity sediment has a smaller average grain size than the Ursa sediment (65% versus 59% of particles <2 μm; Figure 3.2) and, as a result, has smaller pores and pore throats (Dewhurst et al., 1999) and a larger specific surface area (Mayer & Rossi, 1982). In fact, specific surface area (S_a) calculated for the Ursa and Brazos-Trinity sediments from their *LL* values after Santamarina et al. (2002) yielded respective S_a values of 72.2 m^2/g and 93.8 m^2/g. These S_a values reflect the differences in the <2 μm fraction between the two sediments, which is dominated by illite for the Ursa sediment and by smectite for the Brazos-Trinity

sediment. Therefore, it is likely that these smaller pores and pore throats make it harder for microorganisms to survive under increasing vertical stress (Ivanov & Chu, 2008; Park & Santamarina, 2020; Phadnis & Santamarina, 2011) and that as sediment S_a goes up the produced biofilm covers more of the increased particle surface area and protrudes less into the open pore space. This would indicate that biofilms are less effective at decreasing permeability in sediments with smaller pores and pore throats and larger S_a.

Another explanation for the larger impact of microorganisms on the permeability of the Ursa sediment than the Brazos-Trinity sediment could be a difference in the amount of nutrients or the spatial distribution of those nutrients. More Fe^{3+} was reduced in the biotic samples from the Ursa sediment than the Brazos-Trinity sediment (see section 3.6.1; Figure 3.5), despite both sediments having the same amount of synthesized Fe^{3+} added to them (5 mM of $Fe(OH)_3$). The excess of naturally occurring Fe^{3+} or its spatial distribution in the Ursa sediment could have caused biofilms to have a greater effect on permeability, especially at higher porosities, compared to the biotic samples from the Brazos-Trinity sediments which had less naturally occurring Fe^{3+} (Figure 3.5). This increased biofilm growth or spatial distribution of biofilms, combined with differences in sediment properties, are likely the reasons that microorganisms had a greater effect on permeability in the Ursa sediment. Strikingly, changes in sediment properties resulted in larger permeability differences between the Ursa and Brazos-Trinity sediments than the addition of microorganisms to an individual sediment (Figures 3.3c and 3.3d).

The effect of microorganisms on permeability varies with porosity. For the Ursa sediment, permeability is more impacted by microorganisms at higher porosities than at lower porosities, which can be observed by the convergence of regression lines towards lower porosities (Figures 3.3c and 3.3d). Several processes could explain this behavior. First, lower porosities at increased vertical stress could restrict habitable pore space for microorganisms, and potentially puncture them (e.g., Rebata-Landa & Santamarina, 2006). Second, it could be due to the exhaustion of $Fe(OH)_3$ as evidenced by a decrease in Fe^{2+} concentrations over the second half of the Ursa biotic experiments (Figure 3.5). A lack of nutrients such as $Fe(OH)_3$ (for Fe-reducing microorganisms) can cause deterioration of biofilms and can result in a relative increase in permeability (Castegnier et al., 2006). The Fe^{2+} concentrations also decrease in the Brazos-Trinity sediment during the later stages of the biotic experiments (Figure 3.5). However, in this sample, microorganisms appear to have a minimal effect on permeability at all porosities (Figures 3.3c and 3.3d), which is in contrast to the Ursa sediment and is likely due to the decreased grain and pore size as discussed above.

We further place permeability changes caused by microorganisms in our sediments into context using permeability models from literature that depend on sediment properties, including clay fraction (*CF*; % of grains <2 μm; Yang & Aplin, 2010), S_a (Daigle & Dugan, 2009), and *LL* (Casey et al., 2013; Figure 3.6). To do this, we determine the changes in these sediment properties needed to match the greatest change in permeability created by microorganisms for each sediment (change from their respective *CF*, S_a, and *LL* values). Specifically, the largest permeability differences in

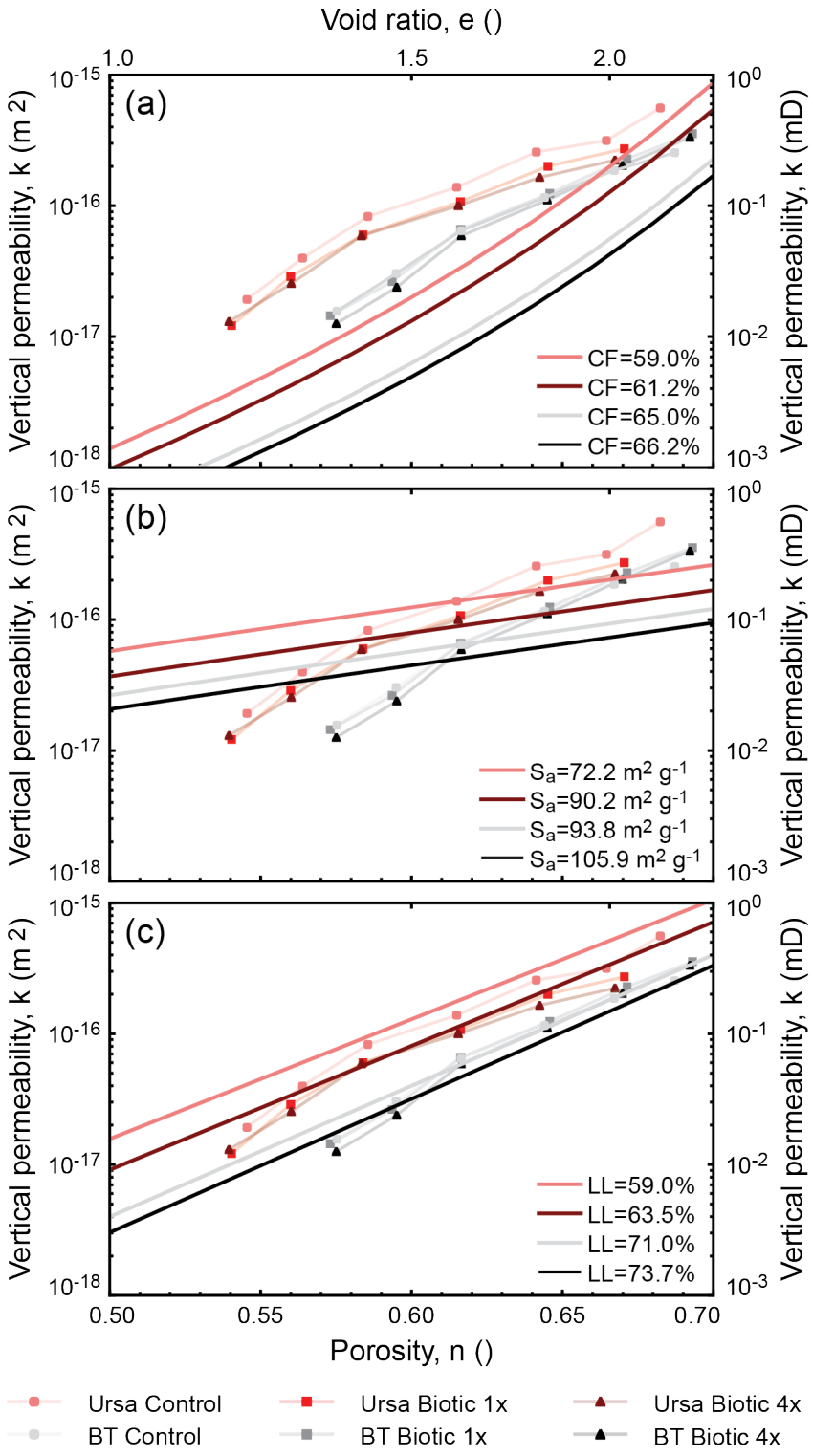

Figure 3.6 Permeability models from literature show that small changes in (a) clay fraction (*CF*; % of grains <2μm; Yang & Aplin, 2010), (b) specific surface area (S_a;

Kozeny-Carman equation; assumed tortuosity factors of 0.11 and 0.15 for the Ursa and Brazos-Trinity sediments, respectively; Daigle & Dugan, 2009), and liquid limit (*LL*; Casey et al., 2013) are needed to match the greatest difference in permeability caused by microorganisms in the Ursa (at porosity of 0.65) and Brazos-Trinity (at porosity of 0.58) sediments. The measured permeability – porosity data from our experiments are displayed with semitransparent lines behind the modeled permeability – porosity curves displayed with solid lines. The salmon and light grey colored solid curves indicate the modeled permeability – porosity relationships using measured *CF*, S_a, and *LL* data (see sections 3.5.1 and 3.6.3 for data) from the Ursa and Brazos-Trinity sediments (approximates the control experiments), respectively. The maroon and black colored solid curves indicate the modeled permeability – porosity relationships at increased values (to match permeability change due to microorganisms) of *CF*, S_a, and *LL* for the Ursa and Brazos-Trinity sediments, respectively.

the Ursa and Brazos-Trinity sediments occur at porosities of 0.64 and 0.58, respectively. At these porosities, the permeabilities of the biotic 4x samples are 1.5 and 1.2 times lower than those of the control samples. In order to account for these same permeability differences in the Ursa and Brazos-Trinity sediments, *CF* would need to be increased by 2.2% and 1.2% (Figure 3.6a; Yang & Aplin, 2010), S_a would need to be increased by 18.0 m^2/g and 12.1 m^2/g (Figure 3.6b; Daigle & Dugan, 2009), and *LL* would need to be increased by 4.5% and 2.7% (Figure 3.6c; Casey et al., 2013), respectively. These models illustrate that the influence of microorganisms on sediment permeability is relatively small for our two fine-grained sediment samples in comparison to changes in *CF*, S_a, and *LL* (Figure 3.6). Ultimately, the effects of microorganisms on sediment permeability are likely lessened for increasingly finer-grained sediments, e.g., from the Ursa sediment to Brazos-Trinity sediment.

Incidentally, the *LL* model from Casey et al. (2013) fits our measured control data for both sediments better than the *CF* (Yang & Aplin, 2010) and S_a (Daigle &

Dugan, 2009) models. This is not surprising as *LL* reflects both the quantity and type of clay minerals present in a mudstone (Casey et al., 2013), and therefore combines the effects of clay-size fraction and S_a, which is a function of mineralogy, into a single model parameter.

3.6.4. Conceptual Model

We developed a conceptual model for biofilm distributions at the pore scale that integrates previous work on sandstones/siltstones and fractures with our new observations for fine-grained sediments (mudstones; Figure 3.7). Our model emphasizes the effects of microorganisms on permeability for sediments with different physical and textural properties (Figure 3.7), given the stark contrast between our results for mudstones and results from literature for coarser-grained sediments and fractures (e.g., Brydie et al., 2005; Cheng et al., 2021; Hill & Sleep, 2002; Taylor & Jaffé, 1990). The sandstone/siltstone and fracture have large grains, large pores and pore throats, low S_a, and few flow paths (Figures 3.7a and 3.7b). As a result, biofilm covers the available surface area and grows out into the large pores and pore throats and occludes porosity (Figure 3.7a and 3.7b), which causes a significant decrease in permeability. It should be noted that in our sandstone/siltstone and fracture illustrations the biofilms occluding pore space are simplified (Figures 3.7a and 3.7b), while they are more complex in three-dimensional pores in nature (Figure 3.7d; e.g., Hand et al., 2008; Harrison et al., 2011). In contrast, the mudstone illustration has grains of various shapes and sizes, small pores and pore throats, high S_a, and multiple flow paths (Figure 3.7c), which are all evidenced in our BSE images (Figure 3.4). In this scenario, we hypothesize that biofilm is spread

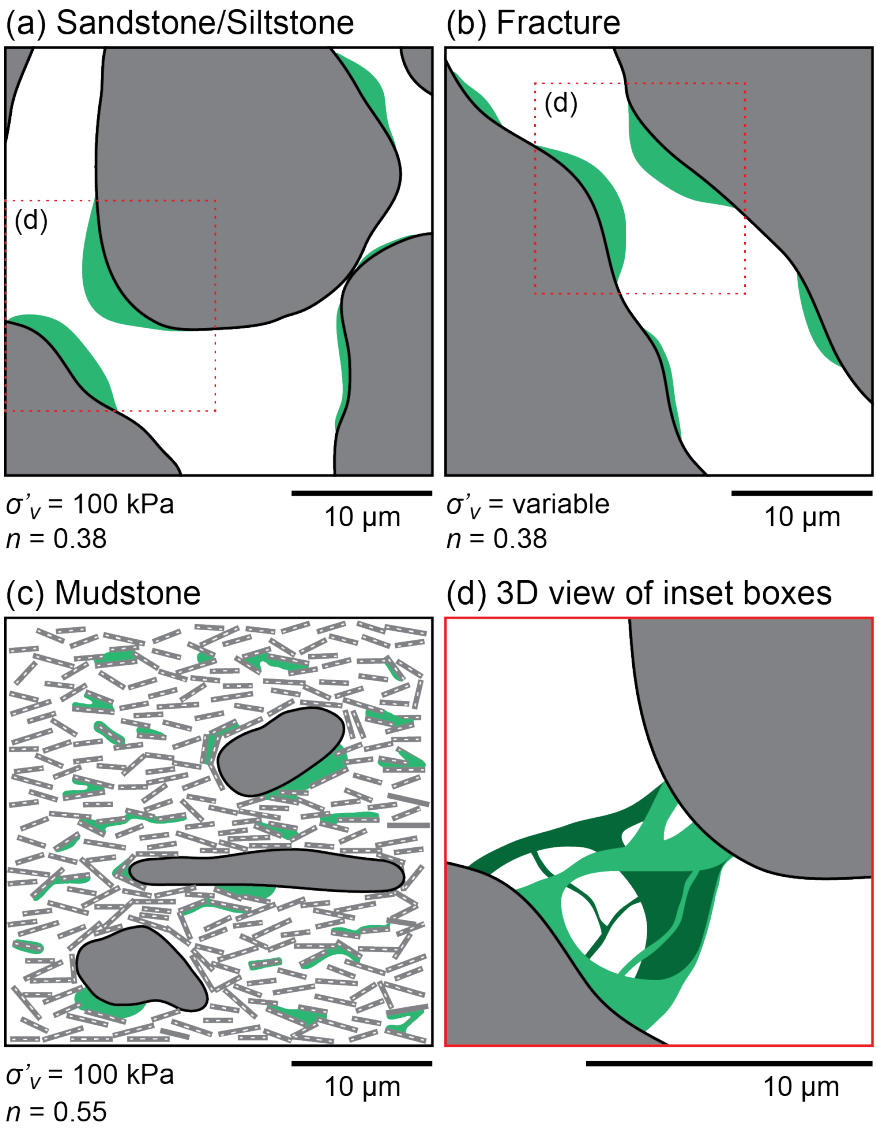

Figure 3.7 A conceptual model showing the two-dimensional pore scale effects of biofilm on a (a) sandstone or siltstone, (b) fracture, and (c) mudstone. (d) Zoomed-in view from the inset boxes in (a) and (b) that is more indicative of three-dimensional (3D) biofilm distribution in natural pores. Biofilms are green and sediments are grey. Each of the illustrations in (a-c) contain the same area of biofilm. The (a) sandstone/siltstone and (c) mudstone illustrations contain respective porosities of 0.38 and 0.55, which are both indicative of burial to a vertical effective stress of 100 kPa (Ingebritsen et al., 2006; Mondol et al., 2007). The (a) sandstone/siltstone and (b) fracture illustrations have the same porosity. Vertical effective stress (σ'_v) and porosity (n) for the illustrations in (a-c) are located below each of the respective illustrations. The theoretical fluid flow is from the bottom to the top of each illustration.

out over a large surface area and fills only a small portion of the available pore space (Figure 3.7c). Despite a larger tortuosity, the high number of flow paths in the mudstone indicates that pores filled with biofilm could potentially even be bypassed (Figure 3.7c). For these reasons, microorganisms have a lessened effect on mudstone permeability than they do on coarser-grained sediments and fractures. Therefore, grain size, specific surface area, pore and pore throat size, and the number of flow paths—all of which could potentially be moderated by (clay) mineralogy—are likely to control changes in permeability due to microorganisms.

3.6.5. Implications

We have shown that microorganisms have a larger effect on the permeability of fine-grained sediments at lower stresses, i.e., higher porosities (Figure 3.3). For fine-grained sediments near the sediment-water interface in marine or lacustrine settings, these porosities could be even higher (0.75-0.80; Boggs, 2009) than measured in our experiments, leading to an even greater reduction in permeability due to the presence of microorganisms. This effect could be amplified in sediments with higher concentrations of nutrients and microbial cells (e.g., Haglund et al., 2003; Kallmeyer et al., 2012; Montagna, 1982) than used in our experiments. The decrease in permeability caused by microorganisms near the sediment-water interface could prevent fluxes of aqueous chemical species (e.g., carbon, nitrogen, sulfur, iron, phosphorous) between the sediments and the overlying water column. Moreover, a decrease in permeability and an increase in compression index, which was also observed in our data (Figure 3.3), are both independent parameters known to increase pore pressure within sediments during

consolidation (Broichhausen et al., 2005). Overpressured pore fluids in the shallow subsurface could cause sediment gravity flows or even submarine landslides (Dugan & Flemings, 2000; Flemings et al., 2008), which in turn have the potential to damage seafloor infrastructure. However, at lower porosities in fine-grained sediments, this effect on pore pressure would be diminished.

Our results also have significance for terrestrial environments and geotechnical engineering practices. At porosities more indicative of fine-grained terrestrial soils (<0.55; e.g., Foti & Lancellotta, 2004; Y. Fu et al., 2019), it is likely that microorganisms have a lessened effect on permeability. Further, adding microorganisms to fine-grained terrestrial soils, as has been hypothesized for coarser-grained soils or fracture systems to prevent fluid flow around radioactive waste sites (Coombs et al., 2008; Harrison et al., 2011) and contaminated areas (Kanmani et al., 2014; Ross & Bickerton, 2002) or on precarious slopes (Ivanov & Chu, 2008), may not be as useful and effective in reducing permeability compared to coarser-grained soils and fractures. Given that microorganisms have been shown to decrease fluid flow in coarser-grained sediments and fractures and that our results show that microorganisms have a limited effect on permeability in finer-grained sediments at lower porosities (<0.55), there is likely a grain size threshold at which microorganisms no longer have a significant impact on permeability, especially at lower porosities.

3.7. Conclusions

We used resedimentation experiments to document the effects of microorganisms on the compression and permeability behavior of fine-grained sediments. Key findings include:

- The pore fluid geochemistry and geomicrobiology data indicate that microorganisms respired and likely developed biofilms in the biotic experiments of both sediments.
- The addition of microorganisms resulted in small, yet systematic changes in compression behavior, as evidenced by an increase in C_c of ~0.06 for both of our sediments.
- The addition of microorganisms resulted in a greater absolute permeability reduction in the Ursa sediment than in the Brazos-Trinity sediment, which is likely due to differences in sediment properties and the amount of microbial activity between the two sediments.
- The effect of microorganisms on permeability is greater at higher porosities and lower vertical effective stresses. The effectiveness of microorganisms in decreasing permeability is not as great in fine-grained sediments compared to coarse-grained sediments and is controlled by sediment grain size, pore and pore throat size, specific surface area, and porosity.

3.8. Data Availability Statement

Our experimental resedimentation and pore fluid geochemistry data are available in the Zenodo repository (https://doi.org/10.5281/zenodo.5519839).

3.9. References

ASTM D7928-17, Standard test method for particle-size distribution (gradation) of fine-grained soils using the sedimentation (hydrometer) analysis, West Conshohocken, PA, 2017, www.astm.org.

ASTM D4318-17, Standard test methods for liquid limit, plastic limit, and plasticity index of soils, ASTM International, West Conshohocken, PA, 2017, www.astm.org.

ASTM D2435, Standard test methods for one-dimensional consolidation properties of soils using incremental loading, ASTM International, West Conshohocken, PA, 2020, www.astm.org.

Blum, P. (1997). Physical properties handbook: a guide to the shipboard measurement of physical properties of deep-sea cores. *Ocean Drilling Program Technical Note, 26*. https://doi.org/10.2973/odp.tn.26.1997

Boggs, S. (2009). *Petrology of Sedimentary Rocks*. New York, NY: Cambridge University Press, 600 p.

Broichhausen, H., Littke, R., & Hantschel, T. (2005). Mudstone compaction and its influence on overpressure generation, elucidated by a 3D case study in the North Sea. *International Journal of Earth Sciences, 94*(5), 956-978. https://doi.org/10.1007/s00531-005-0014-1

Brydie, J. R., Wogelius, R. A., Merrifield, C. M., Boult, S., Gilbert, P., Allison, D., & Vaughan, D. J. (2005). The μ2M project on quantifying the effects of biofilm growth on hydraulic properties of natural porous media and on sorption equilibria: an overview. *Geological Society of London, Special Publications, 249*(1), 131. https://doi.org/10.1144/GSL.SP.2005.249.01.11

Burland, J. B. (1990). On the compressibility and shear strength of natural clays. *Géotechnique, 40*(3), 329-378. https://doi.org/10.1680/geot.1990.40.3.329

Casey, B., Germaine, J. T., Flemings, P. B., Reece, J. S., Gao, B., & Betts, W. (2013). Liquid limit as a predictor of mudrock permeability. *Marine and Petroleum Geology, 44*, 256-263. http://dx.doi.org/10.1016/j.marpetgeo.2013.04.008

Castegnier, F., Ross, N., Chapuis, R. P., Deschênes, L., & Samson, R. (2006). Long-term persistence of a nutrient-starved biofilm in a limestone fracture. *Water Research, 40*(5), 925-934. https://doi.org/10.1016/j.watres.2005.12.038

Cheng, Y., Chou, C., Voltolini, M., Borglin, S., Ajo-Franklin, J. B., & Wu, Y. (2021). Flow and Permeability Evolution during Microbial Sulfate Reduction and Inhibition in Fractured Rocks. *Energy & Fuels, 35*(3), 1989-1997. https://doi.org/10.1021/acs.energyfuels.0c01787

Coombs, P., West, J. M., Wagner, D., Turner, G., Noy, D. J., Milodowski, A. E., et al. (2008). Influence of biofilms on transport of fluids in subsurface granitic environments — some mineralogical and petrographical observations of materials from column experiments. *Mineralogical Magazine, 72*(1), 393-397. https://doi.org/10.1180/minmag.2008.072.1.393

D'Hondt, S., Jørgensen, B. B., Miller, D. J., Batzke, A., Blake, R., Cragg, B. A., et al. (2004). Distributions of Microbial Activities in Deep Subseafloor Sediments. *Science, 306*(5705), 2216. https://doi.org/10.1126/science.1101155

Daigle, H., & Dugan, B. (2009). Extending NMR data for permeability estimation in fine-grained sediments. *Marine and Petroleum Geology, 26*(8), 1419-1427. https://doi.org/10.1016/j.marpetgeo.2009.02.008

Daniels, J. L., Cherukuri, R., & Ogunro, V. O. (2009). Consolidation and Strength Characteristics of Biofilm Amended Barrier Soils. In E. K. Yanful (Ed.), *Appropriate Technologies for Environmental Protection in the Developing World: Selected Papers from ERTEP 2007, July 17–19 2007, Ghana, Africa* (pp. 257-270). Dordrecht: Springer Netherlands.

Delgado-Baquerizo, M., Oliverio, A. M., Brewer, T. E., Benavent-González, A., Eldridge, D. J., Bardgett, R. D., et al. (2018). A global atlas of the dominant bacteria found in soil. *Science, 359*(6373), 320. https://doi.org/10.1126/science.aap9516

Dewhurst, D. N., Aplin, A. C., & Sarda, J.-P. (1999). Influence of clay fraction on pore-scale properties and hydraulic conductivity of experimentally compacted mudstones. *Journal of Geophysical Research: Solid Earth, 104*(B12), 29261-29274. https://doi.org/10.1029/1999JB900276

Dewhurst, D. N., Aplin, A. C., Sarda, J.-P., & Yang, Y. (1998). Compaction-driven evolution of porosity and permeability in natural mudstones: An experimental study. *Journal of Geophysical Research: Solid Earth, 103*, 651-661. https://doi.org/10.1029/97JB02540

Dugan, B., & Flemings, P. B. (2000). Overpressure and Fluid Flow in the New Jersey Continental Slope: Implications for Slope Failure and Cold Seeps. *Science, 289*(5477), 288. https://doi.org/10.1126/science.289.5477.288

Dzevanshir, R. D., Buryakovskiy, L. A., & Chilingarian, G. V. (1986). Simple quantitative evaluation of porosity of argillaceous sediments at various depths of burial. *Sedimentary Geology, 46*(3), 169-175. https://doi.org/10.1016/0037-0738(86)90057-6

Flemings, P. B., Behrmann, J. H., John, C. M., & Scientists, E. (2006). *Proceedings of the Integrated Ocean Drilling Program 308*. College Station, TX: Integrated Ocean Drilling Program Management International, Inc.

Flemings, P. B., Long, H., Dugan, B., Germaine, J., John, C. M., Behrmann, J. H., et al. (2008). Pore pressure penetrometers document high overpressure near the seafloor where multiple submarine landslides have occurred on the continental slope, offshore Louisiana, Gulf of Mexico. *Earth and Planetary Science Letters, 269*(3), 309-325. https://doi.org/10.1016/j.epsl.2007.12.005

Flemming, H.-C., & Wingender, J. (2010). The biofilm matrix. *Nature Reviews Microbiology, 8*(9), 623-633. https://doi.org/10.1038/nrmicro2415

Foti, S., & Lancellotta, R. (2004). Soil porosity from seismic velocities. *Géotechnique, 54*(8), 551-554. https://doi.org/10.1680/geot.2004.54.8.551

Francis, C. A., Roberts, K. J., Beman, J. M., Santoro, A. E., & Oakley, B. B. (2005). Ubiquity and diversity of ammonia-oxidizing archaea in water columns and sediments of the ocean. *Proceedings of the National Academy of Sciences of the United States of America, 102*(41), 14683. https://doi.org/10.1073/pnas.0506625102

Fu, Q. S., Boonchayaanant, B., Tang, W., Trost, B. M., & Criddle, C. S. (2008). Simple menaquinones reduce carbon tetrachloride and iron (III). *Biodegradation, 20*(1), 109. https://doi.org/10.1007/s10532-008-9204-4

Fu, Y., Tian, Z., Amoozegar, A., & Heitman, J. (2019). Measuring dynamic changes of soil porosity during compaction. *Soil and Tillage Research, 193*, 114-121. https://doi.org/10.1016/j.still.2019.05.016

Glatstein, D. A., & Francisca, F. M. (2014). Hydraulic conductivity of compacted soils controlled by microbial activity. *Environmental Technology, 35*(15), 1886-1892. https://doi.org/10.1080/09593330.2014.885583

Haglund, A.-L., Lantz, P., Törnblom, E., & Tranvik, L. (2003). Depth distribution of active bacteria and bacterial activity in lake sediment. *FEMS Microbiology Ecology, 46*(1), 31-38. https://doi.org/10.1016/S0168-6496(03)00190-9

Hand, V. L., Lloyd, J. R., Vaughan, D. J., Wilkins, M. J., & Boult, S. (2008). Experimental Studies of the Influence of Grain Size, Oxygen Availability and Organic Carbon Availability on Bioclogging in Porous Media. *Environmental Science & Technology, 42*(5), 1485-1491. https://doi.org/10.1021/es072022s

Harrison, H., Wagner, D., Yoshikawa, H., West, J. M., Milodowski, A. E., Sasaki, Y., et al. (2011). Microbiological influences on fracture surfaces of intact mudstone and the implications for geological disposal of radioactive waste. *Mineralogical Magazine, 75*(4), 2449-2466. https://doi.org/10.1180/minmag.2011.075.4.2449

Hart, B. S., Flemings, P. B., & Deshpande, A. (1995). Porosity and pressure: Role of compaction disequilibrium in the development of geopressures in a Gulf Coast Pleistocene basin. *Geology, 23*(1), 45-48. https://doi.org/10.1130/0091-7613(1995)023<0045:PAPROC>2.3.CO;2

Hill, D. D., & Sleep, B. E. (2002). Effects of biofilm growth on flow and transport through a glass parallel plate fracture. *Journal of Contaminant Hydrology, 56*(3), 227-246. https://doi.org/10.1016/S0169-7722(01)00210-8

Inagaki, F., Hinrichs, K. U., Kubo, Y., Bowles, M. W., Heuer, V. B., Hong, W. L., et al. (2015). Exploring deep microbial life in coal-bearing sediment down to ~2.5 km below the ocean floor. *Science, 349*(6246), 420-424. https://doi.org/10.1126/science.aaa6882

Ingebritsen, S. E., Sanford, W. E., & Neuzil, C. E. (2006). *Groundwater in Geologic Processes, 2nd Edition*. Cambridge, UK: Cambridge University Press, 564 p.

Ivanov, V., & Chu, J. (2008). Applications of microorganisms to geotechnical engineering for bioclogging and biocementation of soil in situ. *Reviews in Environmental Science and Bio/Technology, 7*(2), 139-153. https://doi.org/10.1007/s11157-007-9126-3

Kallmeyer, J., Pockalny, R., Adhikari, R. R., Smith, D. C., & D'Hondt, S. (2012). Global distribution of microbial abundance and biomass in subseafloor sediment. *Proceedings of the National Academy of Sciences, 109*(40), 16213. https://doi.org/10.1073/pnas.1203849109

Kanmani, S., Gandhimathi, R., & Muthukkumaran, K. (2014). Bioclogging in porous media: influence in reduction of hydraulic conductivity and organic contaminants during synthetic leachate permeation. *Journal of Environmental Health Science and Engineering, 12*(1), 126. https://doi.org/10.1186/s40201-014-0126-2

Lavoie, D. M., Baerwald, R. J., Hulbert, M. H., & Bennett, R. H. (1996). A drinking-straw mini-corer for sediments. *Journal of Sedimentary Research, 66*(5), 1030. https://doi.org/10.2110/jsr.66.1030

Lovley, D. R., Phillips, E. J. P., & Lonergan, D. J. (1989). Hydrogen and Formate Oxidation Coupled to Dissimilatory Reduction of Iron or Manganese by Alteromonas putrefaciens. *Applied and Environmental Microbiology, 55*(3), 700-706. https://doi.org/10.1128/aem.55.3.700-706.1989

Marsili, E., Baron, D. B., Shikhare, I. D., Coursolle, D., Gralnick, J. A., & Bond, D. R. (2008). Shewanella secretes flavins that mediate extracellular electron transfer. *Proceedings of the National Academy of Sciences, 105*(10), 3968-3973. https://doi.org/10.1073/pnas.0710525105

Mayer, L. M., & Rossi, P. M. (1982). Specific surface areas in coastal sediments: Relationships with other textural factors. *Marine Geology, 45*(3), 241-252. https://doi.org/10.1016/0025-3227(82)90112-8

Mills, N. T., Reece, J. S., & Tice, M. M. (2021). Clay minerals modulate early carbonate diagenesis. *Geology, 49*(8), 1015-1019. https://doi.org/10.1130/G48713.1

Mondol, N. H., Bjørlykke, K., Jahren, J., & Høeg, K. (2007). Experimental mechanical compaction of clay mineral aggregates—Changes in physical properties of mudstones during burial. *Marine and Petroleum Geology, 24*(5), 289-311. https://doi.org/10.1016/j.marpetgeo.2007.03.006

Montagna, P. A. (1982). Sampling Design and Enumeration Statistics for Bacteria Extracted from Marine Sediments. *Applied and Environmental Microbiology, 43*(6), 1366-1372. https://doi.org/10.1128/aem.43.6.1366-1372.1982

Monteverde, D. R., Sylvan, J. B., Suffridge, C., Baronas, J. J., Fichot, E., Fuhrman, J., et al. (2018). Distribution of Extracellular Flavins in a Coastal Marine Basin and Their Relationship to Redox Gradients and Microbial Community Members. *Environmental Science & Technology, 52*(21), 12265-12274. https://doi.org/10.1021/acs.est.8b02822

Neuzil, C. E. (1994). How permeable are clays and shales? *Water Resources Research, 30*(2), 145-150. https://doi.org/10.1029/93WR02930

Neuzil, C. E. (2019). Permeability of Clays and Shales. *Annual Review of Earth and Planetary Sciences, 47*(1), 247-273. https://doi.org/10.1146/annurev-earth-053018-060437

Onstott, T. C., Phelps, T. J., Colwell, F. S., Ringelberg, D., White, D. C., Boone, D. R., et al. (1998). Observations pertaining to the origin and ecology of microorganisms recovered from the deep subsurface of Taylorsville Basin, Virginia. *Geomicrobiology Journal, 15*(4), 353-385. https://doi.org/10.1080/01490459809378088

Park, J., & Santamarina, J. C. (2020). The critical role of pore size on depth-dependent microbial cell counts in sediments. *Scientific Reports, 10*(1), 21692. https://doi.org/10.1038/s41598-020-78714-3

Parkes, R. J., Cragg, B. A., Bale, S. J., Getlifff, J. M., Goodman, K., Rochelle, P. A., et al. (1994). Deep bacterial biosphere in Pacific Ocean sediments. *Nature, 371*(6496), 410-413. https://doi.org/10.1038/371410a0

Pedersen, K., Arlinger, J., Ekendahl, S., & Hallbeck, L. (1996). 16S rRNA gene diversity of attached and unattached bacteria in boreholes along the access tunnel to the Äspö hard rock laboratory, Sweden. *FEMS Microbiology Ecology, 19*(4), 249-262. https://doi.org/10.1111/j.1574-6941.1996.tb00217.x

Phadnis, H. S., & Santamarina, J. C. (2011). Bacteria in sediments: pore size effects. *Géotechnique Letters, 1*(4), 91-93. https://doi.org/10.1680/geolett.11.00008

Rebata-Landa, V., & Santamarina, J. C. (2006). Mechanical limits to microbial activity in deep sediments. *Geochemistry, Geophysics, Geosystems, 7*(11), 1-12. https://doi.org/10.1029/2006GC001355

Reece, J. S. (2021). The Impact of Grain Size on the Hydromechanical Behavior of Mudstones. *Geochemistry, Geophysics, Geosystems, 22*(8), 1-23. https://doi.org/10.1029/2021GC009732

Reece, J. S., Flemings, P. B., Dugan, B., Long, H., & Germaine, J. T. (2012). Permeability-porosity relationships of shallow mudstones in the Ursa Basin, northern deepwater Gulf of Mexico. *Journal of Geophysical Research: Solid Earth, 117*(B12), 1-13. https://doi.org/10.1029/2012JB009438

Ross, N., & Bickerton, G. (2002). Application of Biobarriers for Groundwater Containment at Fractured Bedrock Sites. *Remediation Journal, 12*(3), 5-21. https://doi.org/10.1002/rem.10031

Ross, N., Villemur, R., Deschênes, L., & Samson, R. (2001). Clogging of a limestone fracture by stimulating groundwater microbes. *Water Research, 35*(8), 2029-2037. https://doi.org/10.1016/S0043-1354(00)00476-0

Rubey, W. W., & Hubbert, M. K. (1959). Role of fluid pressure in mechanics of overthrust faulting, Part 2. Overthrust belt in geosynclinal are of western Wyoming in light of fluid-pressure hypothesis. *Geological Society of America Bulletin, 70*(2), 167-205. https://doi.org/10.1130/0016-7606(1959)70[167:ROFPIM]2.0.CO;2

Santagata, M., & Kang, Y. I. (2007). Effects of geologic time on the initial stiffness of clays. *Engineering Geology, 89*(1), 98-111. https://doi.org/10.1016/j.enggeo.2006.09.018

Santamarina, J. C., Klein, K. A., Wang, Y. H., & Prencke, E. (2002). Specific surface: determination and relevance. *Canadian Geotechnical Journal, 39*(1), 233-241. https://doi.org/10.1139/t01-077

Schneider, J., Flemings, P. B., Day-Stirrat, R. J., & Germaine, J. T. (2011). Insights into pore-scale controls on mudstone permeability through resedimentation experiments. *Geology, 39*(11), 1011-1014. https://doi.org/10.1130/G32475.1

Seki, K., Miyazaki, T., & Nakano, M. (1998). Effects of microorganisms on hydraulic conductivity decrease in infiltration. *European Journal of Soil Science, 49*(2), 231-236. https://doi.org/10.1046/j.1365-2389.1998.00152.x

Skempton, A. W. (1970). The consolidation of clays by gravitational compaction. *Quarterly Journal of the Geological Society of London, 125*(1-4), 373-411. https://doi.org/10.1144/gsjgs.125.1.0373

Taylor, S. W., & Jaffé, P. R. (1990). Biofilm growth and the related changes in the physical properties of a porous medium: 1. Experimental investigation. *Water Resources Research, 26*(9), 2153-2159. https://doi.org/10.1029/WR026i009p02153

Terzaghi, K. (1943). Theory of Consolidation. In *Theoretical Soil Mechanics* (pp. 265-296): John Wiley & Sons, Inc.

Thormann, K. M., Saville, R. M., Shukla, S., Pelletier, D. A., & Spormann, A. M. (2004). Initial Phases of Biofilm Formation in Shewanella oneidensis MR-1. *Journal of Bacteriology, 186*(23), 8096-8104. https://doi.org/10.1128/JB.186.23.8096-8104.2004

Uramoto, G.-I., Morono, Y., Uematsu, K., & Inagaki, F. (2014). An improved sample preparation method for imaging microstructures of fine-grained marine sediment using microfocus X-ray computed tomography and scanning electron microscopy. *Limnology and Oceanography: Methods, 12*(7), 469-483. https://doi.org/10.1128/JB.186.23.8096-8104.200410.4319/lom.2014.12.469

Viollier, E., Inglett, P. W., Hunter, K., Roychoudhury, A. N., & Van Cappellen, P. (2000). The ferrozine method revisited: Fe(II)/Fe(III) determination in natural waters. *Applied Geochemistry, 15*(6), 785-790. http://doi.org/10.1016/S0883-2927(99)00097-9

Yang, Y., & Aplin, A. C. (2004). Definition and practical application of mudstone porosity–effective stress relationships. *Petroleum Geoscience, 10*(2), 153-162. https://doi.org/10.1144/1354-079302-567

Yang, Y., & Aplin, A. C. (2010). A permeability–porosity relationship for mudstones. *Marine and Petroleum Geology, 27*(8), 1692-1697. https://doi.org/10.1016/j.marpetgeo.2009.07.001

Zeng, Z., & Tice, M. M. (2014). Promotion and nucleation of carbonate precipitation during microbial iron reduction. *Geobiology, 12*(4), 362-371. https://doi.org/10.1111/gbi.12090

Zeng, Z., & Tice, M. M. (2018). Electron Transfer Strategies Regulate Carbonate Mineral and Micropore Formation. *Astrobiology, 18*(1), 28-36. https://doi.org/10.1089/ast.2016.1560

Zhong, X., & Wu, Y. (2013). Bioclogging in porous media under continuous-flow condition. *Environmental Earth Sciences, 68*(8), 2417-2425. https://doi.org/10.1007/s12665-012-1926-2

4. MICROBIALLY DRIVEN SMECTITE-TO-ILLITE REACTION AND CARBONATE DIAGENESIS IN NATURAL SEDIMENTS DURING IRON REDUCTION

4.1. Abstract

Microorganisms are known to induce the smectite-to-illite (S-I) reaction by partially dissolving the smectite structure during the reduction of structurally bound Fe^{3+}, which is commonly associated with the precipitation of authigenic Fe-rich carbonate. However, definitive evidence for this S-I reaction has just been shown using culture experiments with pure clay samples and nanometer scale observations. Additionally, it is difficult to definitively identify this microbial process in nature. Here, we investigated microbially induced S-I transformation and simultaneous carbonate diagenesis by performing resedimentation experiments with and without Fe reducing bacteria added to natural sediments collected from Integrated Ocean Drilling Program cores. We then analyzed these biotic and control sediments, respectively, at multiple scales using a series of analytical methods such as X-ray powder diffraction, micro X-ray fluorescence, electron microprobe elemental mapping, and energy dispersive spectroscopy (EDS). Bulk mineralogy results show that the biotic sediment had increased abundances of illite and amorphous material (likely amorphous carbonates) and decreased abundances of smectite-illite mixed layered clay minerals compared to the control sediment. Moreover, our elemental mapping and EDS analyses show that the biotic sediment had decreased Si, increased Al (minimally increased), K, and Al/Si, and

close spatial relationships of Ca, Mg, and Fe compared to the control sample. These results indicate that Fe^{3+} from the crystal lattice of smectite and smectite-illite mixed layered clay minerals was reduced by microorganisms, which promoted the S-I reaction and the precipitation of amorphous carbonate minerals. Our results further the understanding of microbial S-I transformation by performing experiments with natural sediments and showing that this process can be identified at multiple scales and with multiple techniques. We therefore bridge the gap between observations of this process in culture experiments using pure clay minerals and those made in natural environments.

4.2. Introduction

The smectite-to-illite (S-I) reaction has been one of the most studied aspects of clay diagenesis in marine sediments, as it has been related to overpressure generation and changes to fluid flow properties in sediments (Brown et al., 2001; Tremosa et al., 2020), friction along faults (van der Pluijm, 2011), and oil and gas exploration (e.g., Burst, 1969; Pevear, 1999). This process has historically been thought to only occur due to increased temperature, pressure, and time during burial diagenesis (Ahn and Peacor, 1989; Eberl and Hower, 1976; Hower et al., 1976; Pytte and Reynolds, 1989). However, recent studies have shown that microorganisms can induce this reaction at ambient temperatures and pressures and in short time periods (Kim et al., 2004; Koo et al., 2014; Koo et al., 2016; Zhang et al., 2007).

Microbially driven S-I transformation occurs as microorganisms solubilize and reduce the structural Fe^{3+} from smectites (Kostka et al., 2002; Kostka et al., 1999; Kostka et al., 1996; Stucki and Kostka, 2006). This process partially dissolves the

smectite lattice (Dong et al., 2003) and is associated with the release of Si and Fe from the smectite lattice, the addition of K (and possibly Al) to the illite lattice, and an increase in the Al/Si ratio in the resultant illite (Dong et al., 2003; Hower et al., 1976; Koo et al., 2014; Koo et al., 2016; Vorhies and Gaines, 2009):

$$\text{smectite} + K^+ \ (+Al^{3+}) \rightarrow \text{illite} + Si^{4+} + Fe^{2+} \ . \quad \text{(Eq. 4.1)}$$

While previous researchers have identified the dissolution and elemental exchange processes that occur during microbially driven S-I transformation, they have primarily utilized culture experiments with pure clay samples, rather than natural sediments, and nanometer scale observations (e.g., Kim et al., 2004; Koo et al., 2014; Koo et al., 2016). Moreover, the recognition of microbially driven S-I transformation in natural environments is difficult, therefore yielding few research studies and speculative interpretations (e.g., Kim et al., 2019; Vorhies and Gaines, 2009).

The microbial reduction of Fe^{3+} during the S-I reaction is often associated with carbonate precipitation (O'Reilly et al., 2005; Zhang et al., 2007). This is because microbial Fe^{3+} reduction coupled to the oxidation of organic matter is known to raise local pH values and produce Fe^{2+}, and thereby increase carbonate mineral saturation (Boudreau and Canfield, 1988; Reimers et al., 1996; Zeng and Tice, 2014):

$$SI = log_{10}\left(\frac{[Me^{n+}][CO_3^{2-}]}{[K_{sp}]}\right), \quad \text{(Eq. 4.2)}$$

where Me^{n+} is a given metal cation and K_{sp} is the solubility product constant. However, previous work has overlooked potential relationships between the S-I reaction and authigenic Fe-carbonates in natural settings.

Here, we investigate the microbially driven S-I reaction and coupled carbonate diagenesis by performing resedimentation experiments with and without Fe reducing bacteria added to natural marine sediments composed of different mineral types and grain sizes. The control and biotic sediments were then analyzed at different scales using multiple analytical methods. We show that microbially induced S-I transformation and amorphous carbonate precipitation both occurred in the biotic sediment. Our work therefore bridges the gap between observations made from previous laboratory experiments using pure clay minerals and those from natural environments.

4.3. Materials and Methods

The sediment sample used in this study is referred to as the Ursa sediment and was created by homogenizing natural, clay-rich sediments from the Gulf of Mexico into a mudstone powder. Specifically, the Ursa sediment was collected from the Ursa Basin (Site U1324; Figure 4.1) during IODP Expedition 308. It is composed of 59% clay-size (<2μm) particles (see section 3.5.1; Figure 3.2). The bulk mineralogy of this sediment is dominated by quartz and clay minerals, with subordinate amounts of feldspar, calcite, and dolomite (see section 3.5.1; Figure 3.2). In the <2μm fraction, this sediment contains a mixture of illite, smectite, kaolinite, and minor amounts of chlorite (in descending order; see section 3.5.1; Figure 3.2). The grain size and mineralogy data were previously published in (Mills et al., 2021), where this sediment was referred to as the Gulf of Mexico sediment.

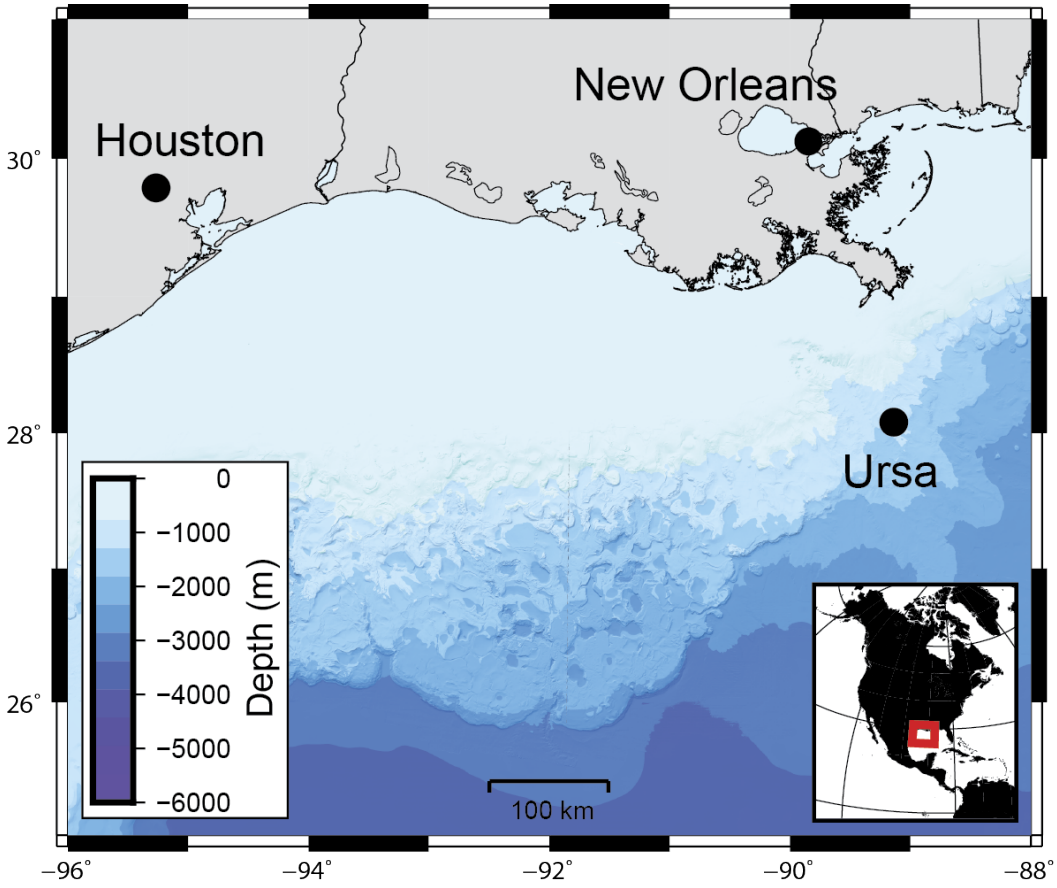

Figure 4.1 Bathymetry map showing the location of the Ursa sediment obtained from the Gulf of Mexico during IODP Expedition 308.

We performed resedimentation experiments with (biotic sediment) and without (control sediment) microorganisms added to the Ursa sediment, which each lasted 20 days. The resedimentation method replicates natural burial processes and consists of mixing a dry mudstone powder with a fluid (pore fluid; described below) to create a stable slurry, pouring the slurry into a consolidometer, and incrementally loading the slurry with weights to a maximum vertical effective stress of 100 kPa while allowing it to fully drain on both ends of the specimen (see section 3.4.3; ASTM D2435; ASTM

International, 2020; e.g., Reece, 2021; Santagata and Kang, 2007). Upon completion, the sample can be extruded as a cohesive, intact mudstone. Our resedimentation experiments were performed in an anaerobic chamber containing 80% N_2, 15% CO_2, and 5% H_2 and all pieces of the consolidometer that came in contact with the slurries were sterilized either by autoclave or by wiping with 70% ethanol under UV light in a laminar flow hood.

We used the iron reducing bacteria *Shewanella oneidensis* MR-1 in our biotic experiments and designed the pore fluid to serve as a medium to support *Shewanella* growth. The *Shewanella* were cultured for 24 h in autoclaved Lysogeny Broth (LB) medium and original cell counts were made using a Beckman Coulter DU 730 spectrophotometer after harvesting and washing the cells (after Zeng and Tice, 2018). The *Shewanella* were admixed with the Ursa slurry, before pouring into the consolidometer, at a concentration of ~$1.0x10^9$ cells/cm^3_{solids} (volume of solids) for the biotic experiment, while the control experiment had no cells added. The pore fluid medium is modified from Marsili et al. (2008) and Zeng and Tice (2014) and is composed of 0.0174 g/L K_2HPO_4, 0.123 g/L $MgSO_4 \cdot 7H_2O$, 0.227 g/L $(NH_4)_2SO_4$, 0.535 g/L NH_4Cl, 1.47 g/L $CaCl_2 \cdot 2H_2O$, 0.5 g/L casamino acid, 3.73 mL/L Na DL-lactate (electron donor), and 5 mM $Fe(OH)_3$ (electron acceptor). The $Fe(OH)_3$ was prepared fresh by adjusting a solution of 0.17 M $FeCl_3$ to a pH of 7 with 5 M NaOH (Fu et al., 2008). The pore fluid medium was filter-sterilized, equilibrated in the anaerobic chamber, and the pH was adjusted to ~7.0.

During the control and biotic experiments, the effluent pore fluid was monitored for pH and the concentration of Fe^{2+}. The pH was measured with a Fisherbrand accumet micro pH electrode (model 13-620-850) and the concentration of Fe^{2+} was measured using the ferrozine assay (Viollier et al., 2000). All steps for these measurements were performed immediately after collection (within <5 minutes) and inside the anaerobic chamber except the reading of final absorbance values for the ferrozine assay, which were collected using a BioTek ELx800 microplate reader.

After completion of the resedimentation experiments, subsamples of the extruded specimens were air-dried and powdered with a mortar and pestle and the mineralogy of the control and biotic sediments were determined by standard powder X-ray diffraction (XRD). The whole rock XRD analyses were performed using a Rigaku Miniflex 6G X-ray diffractometer with a CuKα source operating at 40 kV and 15 mA. XRD patterns were collected from 3-65° 2θ with a dwell time of 3° 2θ per minute.

Subsamples of the intact mudstone were resin embedded and polished to prepare them for μXRF and electron microprobe work. The subsamples were taken parallel to the applied stress using a standard drinking straw (mini-coring technique; Lavoie et al., 1996), which were subsequently cut into 1-3 mm slices using a razor blade. These 1-3 mm slices were then dehydrated with ethanol and embedded with Quetol 651 resin using the methodology of Uramoto et al. (2014). After resin embedding, the subsamples were cut and then polished using oil-based aluminum oxide grits (coarser grits) and diamond paste (final polish).

The polished surfaces of the resin embedded control and biotic sediments were analyzed for elemental abundances using μXRF and an electron microprobe. The μXRF analyses were carried out using a Bruker M4 Tornado Plus with a rhodium anode, a tube voltage of 50 kV, and a tube current of 600 μA. Electron microprobe analyses were carried out using a Cameca SXFive electron microprobe housed in the Materials Characterization Facility at Texas A&M University. Standards used for quantitative mapping consisted of appropriate mineral standards for Mg, S, Ca, Si, Fe, Na, Ti, K, Al, and Mn. Beam conditions for standards calibration and energy dispersive spectroscopy (EDS) spot analyses were 15 kV and 10 nA and used minimum beam spot size. Quantitative mapping was acquired using the Probe for EPMA software, mean atomic number backgrounds, beam conditions of 15 kV and 50 nA, and minimum spot size. The map settings were 250 x 250 pixels with a step size of 0.1 μm (total map areas of 25 x 25 μm) and the count time on each pixel was 70 ms.

4.4. Results

4.4.1. Pore Fluid Geochemistry

The pH and concentration of Fe^{2+} in the effluent pore fluid is used to monitor bacterial activity and chemical conditions in our resedimentation experiments. As the *Shewanella* used in our biotic experiment reduce Fe^{3+} ($Fe(OH)_3$) and oxidize lactate, Fe^{2+} and acetate are produced, respectively (e.g., Lovley et al., 1989):

$$4Fe(OH)_3 + CH_3CHOHCOO^- + 7H^+ \rightarrow 4Fe^{2+} + HCO_3^- + CH_3COO^- + 10H_2O \text{ .}$$

(Eq. 4.3)

Therefore, this reaction should increase pH via the consumption of H^+ and increase the concentration of Fe^{2+}. In the control experiment, effluent pH values remained constant between 6.7 and 6.9 (Figure 4.2). Conversely, effluent pH values in the biotic

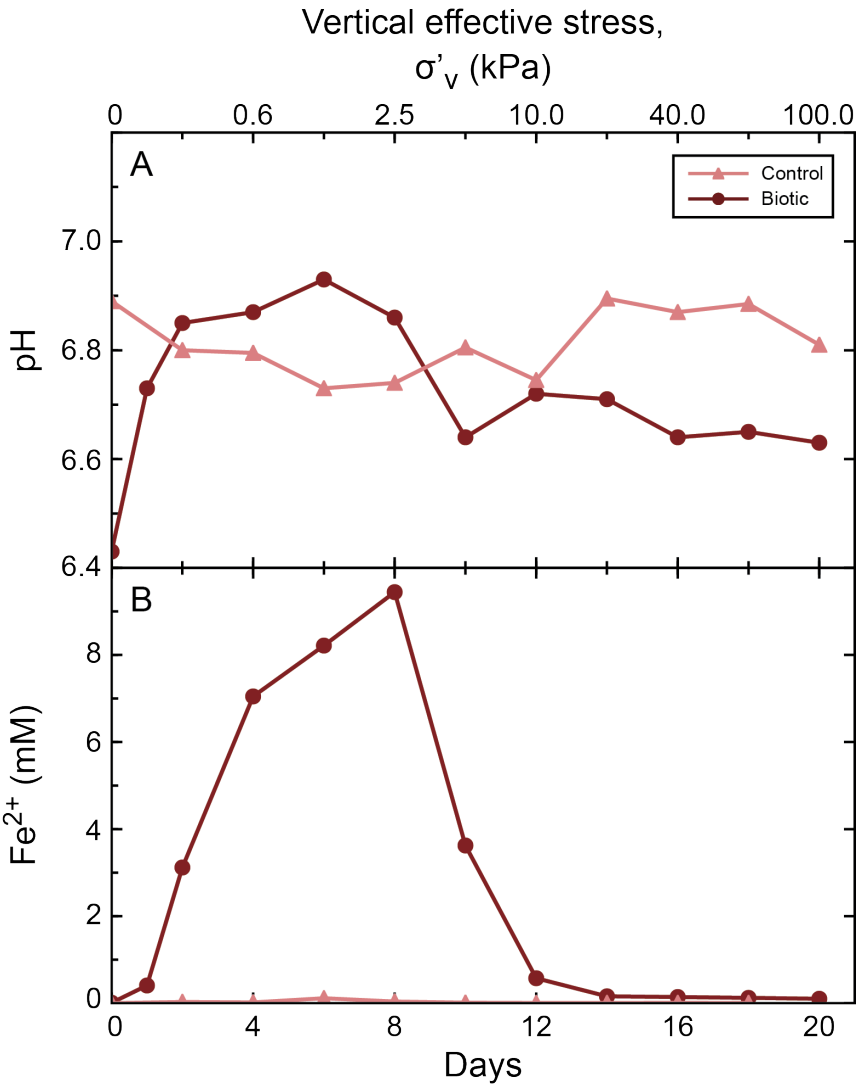

Figure 4.2 Pore fluid geochemistry results showing (A) pH values and (B) Fe^{2+} concentrations for the control and biotic sediments throughout each experiment.

experiment were initially ~6.4—despite titrating the pore fluid to a pH of ~7 before creating the slurries for the control and biotic experiments—and increased to 6.9 over the first 6 days. After this point, the effluent pH declines to ~6.5 from days 6–9 and then remains near that value for the remainder of the experiment. The effluent Fe^{2+} concentrations in the control experiment are low (<0.1 mM) for the duration of the experiment. In the biotic experiment, effluent Fe^{2+} concentrations rise to ~9 mM over the first 8 days, fall to ~1 mM between days 8 and 12, and remain low (<0.5 mM) for the remainder of the experiment.

4.4.2. Bulk Mineralogy

The bulk mineralogy of the control and biotic sediments are both comprised of quartz, clay minerals (smectite, illite, and kaolinite), feldspar, calcite, and dolomite (Figure 4.3), however, key differences exist between the two sediments. The biotic sediment displays higher relative intensities from 3–8 °2θ than the control sediment, indicating an increase in amorphous material and a decrease in crystallinity. The illite peaks at 8.8 °2θ and 27.8 °2θ are relatively higher in the biotic sediment than the control sediment. There is also a slight increase in the dolomite peak at 30.8 °2θ in the biotic sediment relative to the control sediment. In contrast, the biotic sediment has lower relative intensities for what are likely goethite and mixed layer smectite-illite peaks at 22.9 °2θ and 27.4 °2θ, respectively.

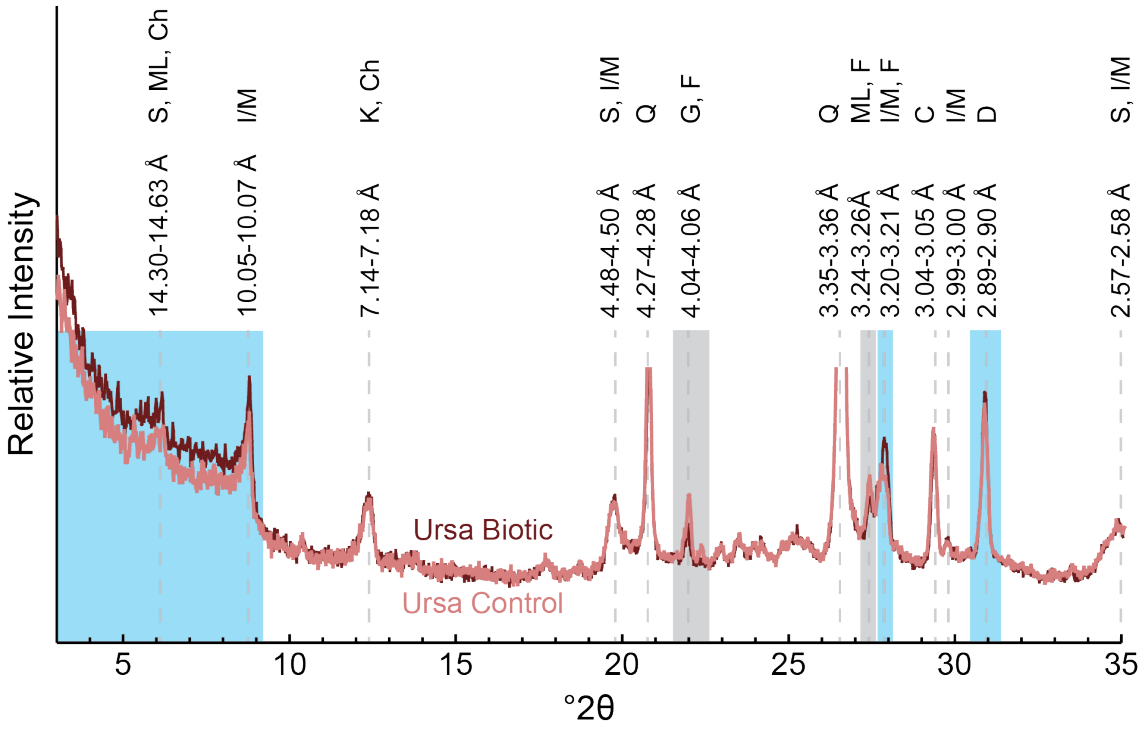

Figure 4.3 Bulk mineralogy for the control and biotic sediments. The blue and gray shaded areas indicate peaks where the relative intensity for the biotic sediment is higher and lower, respectively, than the control sediment. Above the XRD patterns, d-spacings for each peak are shown (in Angstroms). S = smectite, ML = mixed layer smectite-illite, I/M = illite/mica, K = kaolinite, Ch = chlorite, Q = quartz, F = feldspar, C = calcite, D = dolomite, G = goethite.

4.4.3. Bulk Elemental Composition

The bulk element compositions of the control and biotic sediments are similar to each other (Table 4.1). Between the two sediments, the greatest differences are just 0.34 wt.% and 0.44 wt.% for SiO_2 and Al_2O_3, respectively, while all other elements have differences of <0.1 wt.% (Table 4.1). A ternary plot with endmembers of Al_2O_3, MgO + FeO, and CaO + K_2O + Na_2O—endmembers listed in order of increasing elemental

mobility—indicates that the composition for the biotic sediment moves slightly towards the $CaO + Na_2O + K_2O$ and $MgO + FeO$ endmembers (Figure 4.4).

Table 4.1 Bulk elemental compositions for the control and biotic sediments in wt.%.

Sample	SiO_2	Al_2O_3	Fe_2O_3	CaO	MgO	MnO	K_2O	Na_2O	TiO_2	SO_3	BaO
Ursa control	57.79	14.06	8.89	8.32	2.79	0.16	4.16	0.65	0.98	0.28	0.25
Ursa biotic 4x	58.13	13.62	8.92	8.24	2.75	0.16	4.07	0.72	0.97	0.27	0.22

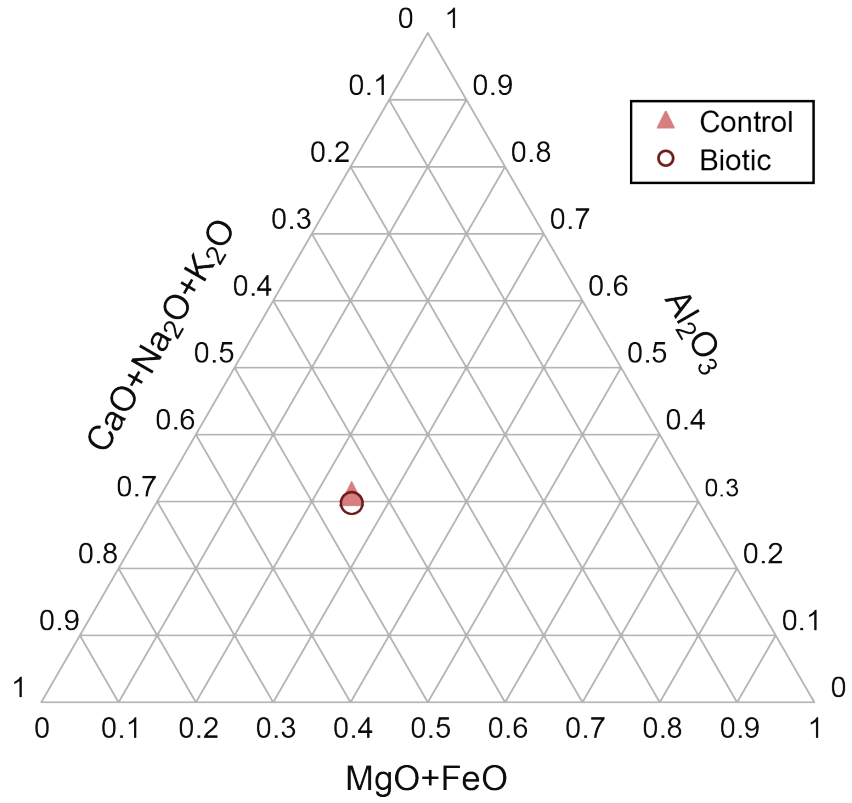

Figure 4.4 Ternary plot showing the compositions of the control and biotic sediments. Endmembers represent groups of elements with similar mobilities. Endmember mobility increases from Al_2O_3 to MgO + FeO to $CaO + Na_2O + K_2O$.

4.4.4. Fine-Scale Elemental Analysis

Based on electron microprobe quantitative elemental maps, the elements commonly associated with carbonate minerals (CaO, MgO, and FeO; presented as wt.% oxides) display similarities and some key differences between the control and biotic sediments. The biotic sediment displays a slightly higher proportion of the mapped area with CaO concentrations >~6 wt.%) than the control sediment (Figures 4.5A and 4.5B). Mapped areas with MgO concentrations >~8 wt.% are similar between the control and biotic sediments (Figures 4.5C and 4.5D). However, the distribution and morphology of MgO between the control and biotic sediments differ. In the biotic sediment, there are rod-like structures ~1-2 μm in length (white arrows in Figure 4.5) and small diffuse, circular enrichments of MgO (~4 wt.%) directly adjacent to larger grain-like areas (likely dolomite) which have MgO concentrations >8 wt.% (red arrows in Figure 4.5), both of which are absent or rare in the control sediment (Figure 4.5C and 4.5D). The concentrations and distribution of FeO is vastly different between the control and biotic sediments. This is exemplified by an area with high concentrations of FeO (>25 wt.%) in the biotic sediment (dashed box in Figure 4.5F), while FeO concentrations in the control sediment are low (<~15 wt.%; Figure 4.5E). Within this region of the biotic sediment, there is an area with high concentrations of FeO (>35 wt%; Figure 4.5F) that corresponds to an area of high total wt.% (black arrow in Figure 4.6N), which indicates a solid grain rich in Fe. Adjacent to this rhombohedral grain (to the upper right), there is an area enriched in Fe, however, this area displays low total wt.%, indicating that it is part of the matrix and not a solid grain (white arrow in Figure 4.6N). The biotic FeO

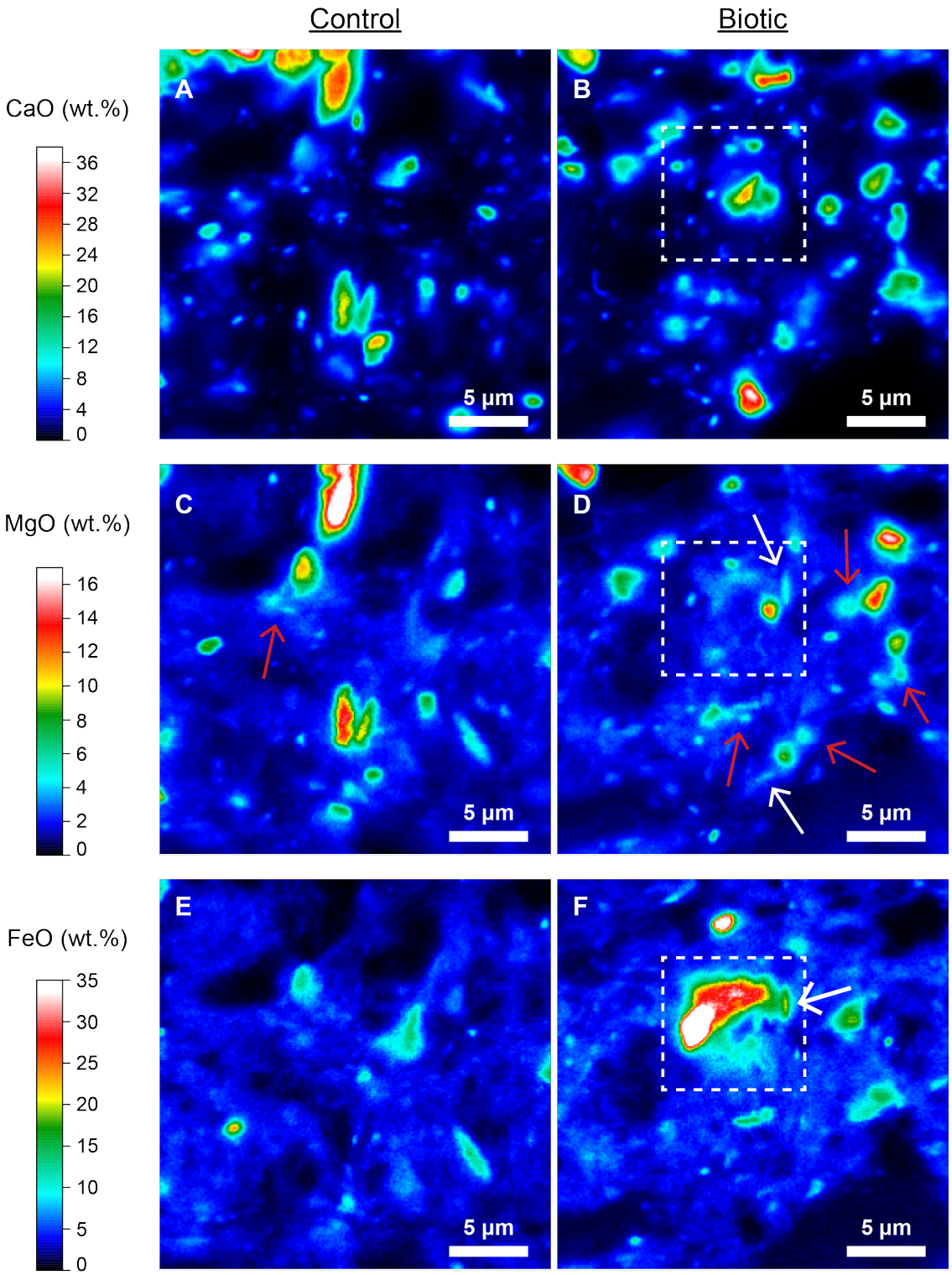

Figure 4.5 Electron microprobe elemental maps of (A, B) CaO, (C, D) MgO, and (E, F) FeO for the control (left) and biotic (right) sediments with associated wt.%

scales (far left). Dashed boxes indicate an area with high concentrations of FeO which overlaps and is adjacent to areas with high concentrations of CaO and MgO. White arrows point to rod-like structures ~1-2 μm in length. Red arrows point to diffuse, circular enrichments of MgO adjacent to larger MgO-rich grains.

map also displays rod-like structures ~1-2 μm in length (Figure 4.5F), similar to the biotic MgO map, which are absent in the FeO map for the control sediment. Interestingly, for the biotic maps, the areas of high FeO concentrations overlap with and are directly adjacent to areas of high MgO and CaO concentrations (dashed boxes in Figures 4.5B, 4.5D, and 4.5F). In contrast, the control sediment displays little correlation between FeO, MgO, and CaO (although direct overlap of CaO and MgO signifies dolomite grains), lower concentrations of FeO (<~12 wt.%), and the areas between 9–12 wt.% FeO correspond to areas of high total wt.%, indicating they are solid grains (black arrows in Figure 4.6M).

Based on electron microprobe quantitative elemental maps, the elements commonly associated with clay minerals (Al_2O_3, SiO_2, and K_2O; presented as wt.% oxides) display subtle differences between the control and biotic sediments. In the control and biotic maps, we highlight respective areas dominantly comprised of clay minerals with a dashed box around them. We discuss differences in clay mineral elemental compositions between the control and biotic sediments for clay minerals within these respective boxes (Figure 4.6). Additionally, due to the resin used (composed of carbon) to embed our sediments, low total weight percentages were recorded in areas dominated by clay minerals and devoid of solid framework grains (Figures 4.6M and 4.6N). We therefore normalized the Al_2O_3 and SiO_2 maps by dividing them both by the

total weight percent maps for each sediment. Clay minerals in the biotic sediment displayed higher Al_2O_3 concentrations (not normalized) than the control sediment by ~2 wt.% (Figures 4.6A and 4.6B). When normalizing by total wt.%, differences between the biotic and control sample are minimized and clay minerals in the biotic sediment have only a slightly higher average Al_2O_3/total wt.% ratio (ratio of 0.22) than the control sediment (ratio of 0.20; Figures 4.6C and 4.6D), indicating that the control and biotic sediments have similar concentrations of Al_2O_3. The clay mineral SiO_2 concentrations (not normalized) are much higher in the biotic sample (39 wt.%) than the control sediment (33 wt.%; Figures 4.6E and 4.6F). However, when normalized by total wt.%, the clay mineral SiO_2/total wt.% ratio is lower in the biotic sediment (ratio of 0.58) than in the control sediment (ratio of 0.67; Figures 4.6G and 4.6H), indicating that clay minerals in the biotic sediment have less SiO_2 than in the control sediment. Additionally, clay minerals in the biotic sediment have higher Al_2O_3/SiO_2 ratios (ratio of ~0.4) than in the control sediment (ratio of ~0.3; Figures 4.6I and 4.6J), which is likely due to clay minerals having lower SiO_2 concentrations in the biotic sediment compared to the control sediment. Clay minerals in the biotic sediment appear to have slightly higher concentrations of K_2O (~2.5 wt.%) than in the control sediments (~2 wt.%; Figures 4.6K and 4.6L).

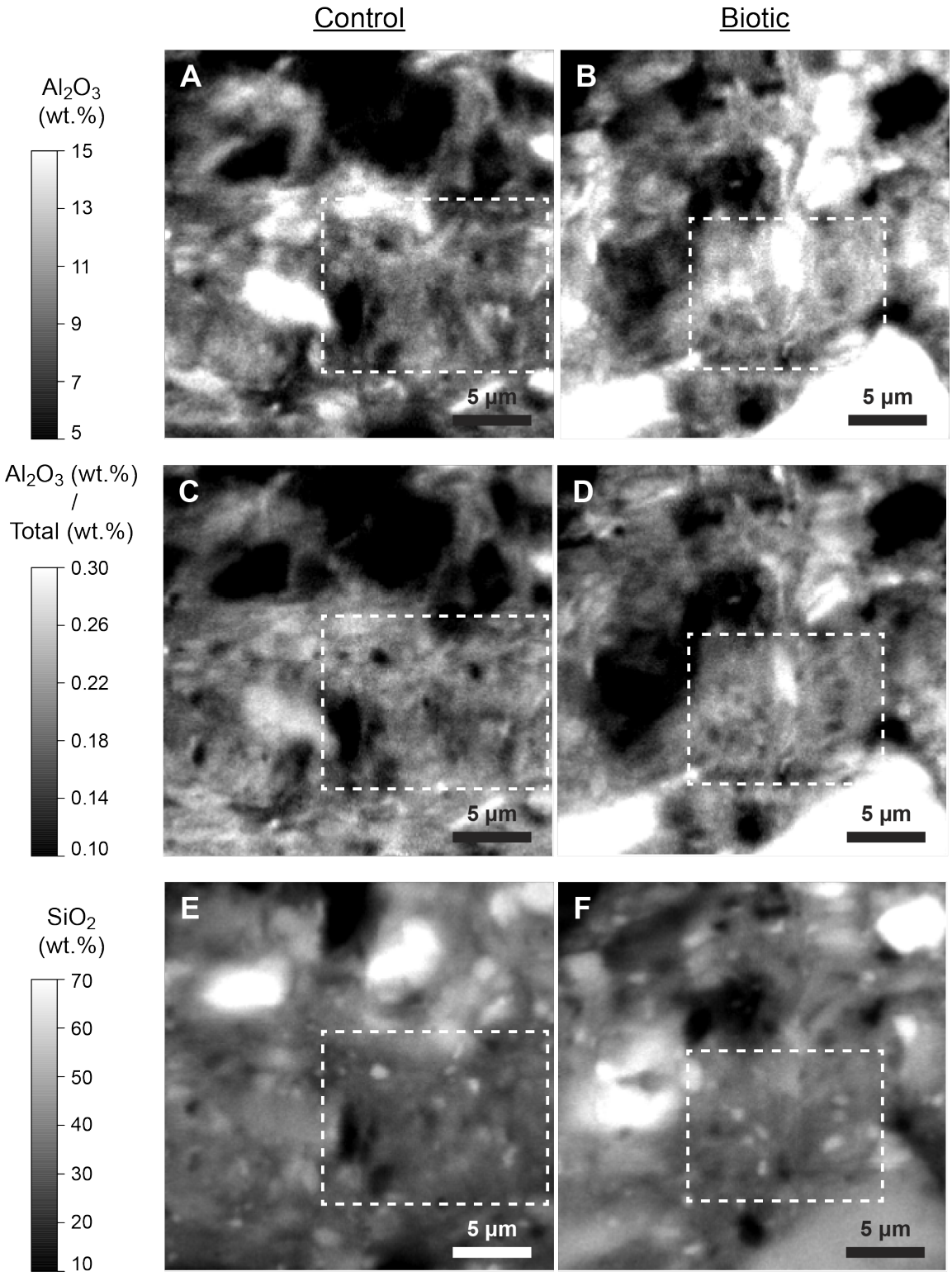
Control
Biotic
A
B
C
D
E
F
5 µm
Al_2O_3 (wt.%)
15
13
11
9
7
5
Al_2O_3 (wt.%) / Total (wt.%)
0.30
0.26
0.22
0.18
0.14
0.10
SiO_2 (wt.%)
70
60
50
40
30
20
10

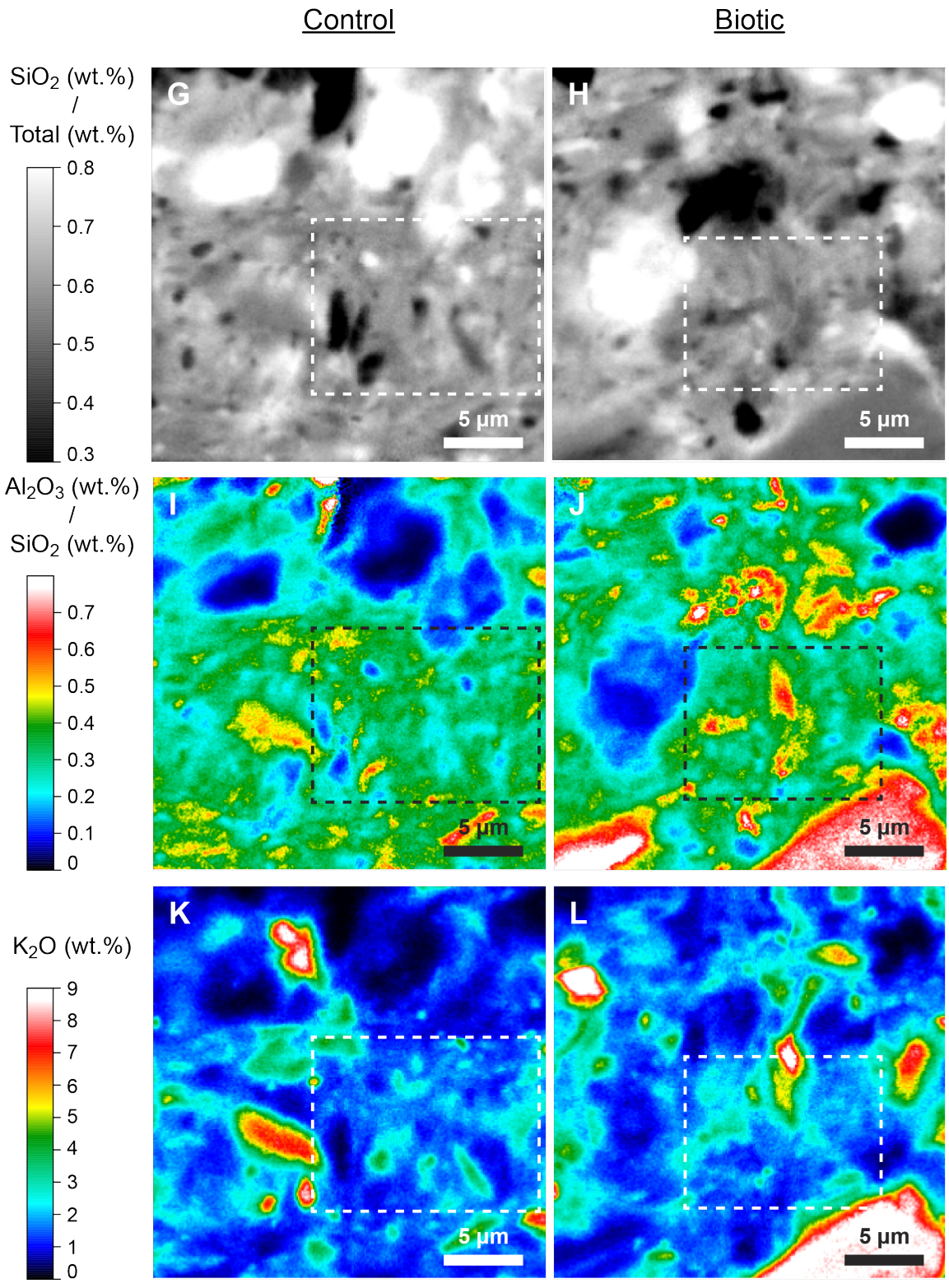
Control
Biotic
SiO2 (wt.%) / Total (wt.%)
0.8
0.7
0.6
0.5
0.4
0.3
G
H
5 µm
Al2O3 (wt.%) / SiO2 (wt.%)
0.7
0.6
0.5
0.4
0.3
0.2
0.1
0
I
J
5 µm
K2O (wt.%)
9
8
7
6
5
4
3
2
1
0
K
L
5 µm

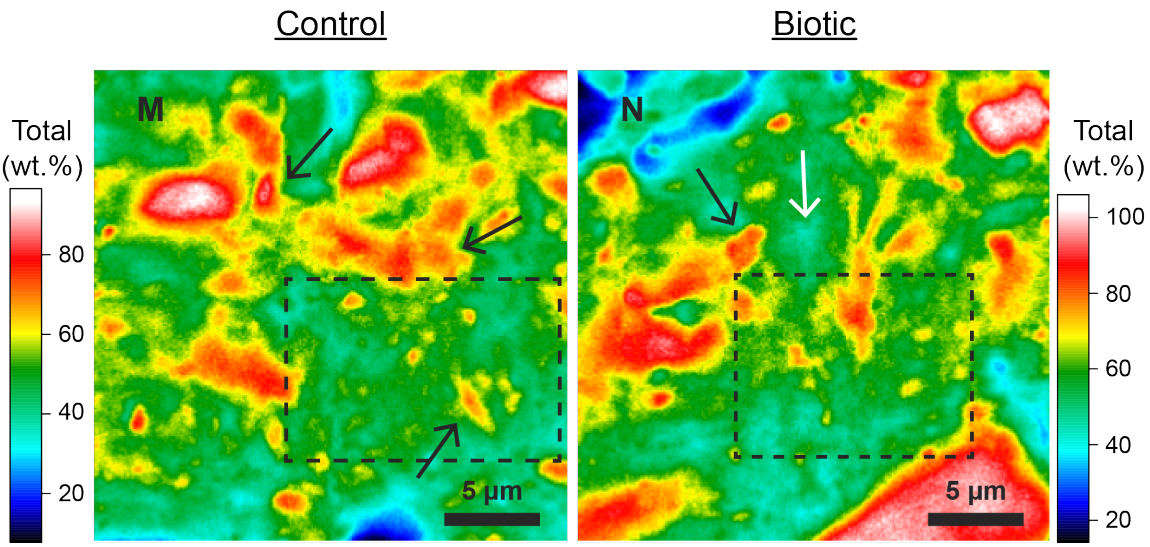

Figure 4.6 Electron microprobe elemental maps of (A, B) Al_2O_3, (C, D) Al_2O_3/total wt.%, (E, F) SiO_2, (G, H) SiO_2/total wt.%, (I, J) Al_2O_3/SiO_2, (K, L) K_2O, and (M, N) total wt.% for the control (left) and biotic (right) sediments with associated color scales (the same one on far left in A-L and different ones on far left and far right in M and N). Dashed boxes indicate areas dominantly comprised of clay minerals. Black arrows point to solid grains with high total wt.%. White arrow points to an area in the matrix with low total wt%.

Electron microprobe EDS spot analyses were also carried out on 17 individual clay minerals in both the control (Table 4.2) and biotic (Table 4.3) sediments. Average clay mineral Al concentrations are similar between the biotic (10.64 at.%) and control (10.94 at.%) sediments, while average clay mineral Si is lower in the biotic sediment (26.01 at.%) than the control sediment (30.21 at.%; Tables 4.2 and 4.3). Thus, the average Al/Si ratio of individual clay minerals is higher in the biotic sediment (ratio of 0.41) than the control sediment (ratio of 0.37; Tables 4.2 and 4.3).

Table 4.2 Electron microprobe spot analyses of individual clay minerals in the control sediment.

Spot number	Al (at.%)	Si (at.%)	K (at.%)	Ca (at.%)	Fe (at.%)	Al/Si	K / (K+2Ca)
1	10.11	37.48	2.13	3.3	2.92	0.27	0.24
3	10.41	29.01	1.64	3.18	1.94	0.36	0.21
4	12.62	26.47	1.89	3.97	2.7	0.48	0.19
5	12.75	31.83	3.22	2.56	3.61	0.40	0.39
6	13.11	33.66	2.07	2.29	2.93	0.39	0.31
7	11.64	29.69	2.79	3.88	2.88	0.39	0.26
8	11.46	33.42	2.36	1.99	2.53	0.34	0.37
9	7.99	32.61	1.65	4.13	1.63	0.25	0.17
10	11.82	29.68	2	1.36	2.42	0.40	0.42
11	10.23	28.01	1.94	1.27	3.37	0.37	0.43
12	10.95	36.48	2.19	3.17	3.54	0.30	0.26
14	11.94	29.86	2.95	2.09	3.79	0.40	0.41
15	11.51	30.35	1.9	1.15	2.95	0.38	0.45
17	8.47	23.65	1.69	10.37	4.53	0.36	0.08
18	9.4	24.5	2.17	4.19	3.41	0.38	0.21
19	9.99	26.91	1.8	5.19	2.8	0.37	0.15
20	11.61	29.99	2.02	2.24	2.78	0.39	0.31
Average	10.94	30.21	2.14	3.31	2.98	0.37	0.29

Table 4.3 Electron microprobe spot analyses of individual clay minerals in the biotic sediment.

Spot number	Al (at.%)	Si (at.%)	K (at.%)	Ca (at.%)	Fe (at.%)	Al/Si	K / (K+2Ca)
1	11.63	25.48	1.51	0.94	1.88	0.46	0.45
2	10.37	29.57	2.01	1.73	3.01	0.35	0.37
3	8.55	23.62	1.2	5.4	2.14	0.36	0.10
5	11.81	26.95	1.97	2.54	2.58	0.44	0.28
6	8.58	19.21	0.97	7.13	2.89	0.45	0.06
7	10.06	28.29	2.32	0.69	3.38	0.36	0.63
9	13.45	25.85	1.6	3.56	2.17	0.52	0.18
10	12.13	32.56	2.42	1.73	3.49	0.37	0.41
11	11.98	26.62	1.59	2.93	2.26	0.45	0.21
12	11.44	29.48	1.62	1.09	3.53	0.39	0.43
13	10.91	22.43	2.29	1.34	1.88	0.49	0.46
14	9.04	20.62	2.27	1.46	1.58	0.44	0.44
15	7.35	18.6	1.31	9.72	2.14	0.40	0.06
16	11.52	31.05	3.69	1.06	2.39	0.37	0.64
17	11.76	35.41	4.79	1.16	2.87	0.33	0.67
18	11.42	25.55	1.62	2.21	3.7	0.45	0.27
19	8.8	20.92	1.63	2.98	2.6	0.42	0.21
Average	10.64	26.01	2.05	2.80	2.62	0.41	0.35

4.5. Discussion

4.5.1. Pore Fluid Geochemistry

The pH and Fe^{2+} data indicate that the bacteria added to the biotic sediment actively respired Fe^{3+} and that the chemical conditions in the control and biotic sediments were vastly different (Figure 4.2). During Fe^{3+} reduction (days 0–8) in the biotic sediment, the rise in effluent Fe^{2+} concentrations directly coincided with an increase in effluent pH (Figure 4.2), which indicates that carbonate mineral saturation (*SI*) also increased (Equation 4.2). In the biotic sediment, pore fluid effluent Fe^{2+} concentrations reached ~9 mM (day 8; Figure 4.2), which far exceeded the 5 mM $Fe(OH)_3$ added at the beginning of each experiment. This excess Fe^{3+} (~4 mM) likely came from preexisting Fe-oxides, such as goethite (Figure 4.3), and Fe-rich clay minerals within the sediment (e.g., Kostka et al., 1999; Kostka et al., 1996; Stucki and Kostka, 2006). It is likely that by day 8 all of the available Fe^{3+} had been respired by the bacteria. Between days 8 and 12, effluent Fe^{2+} concentrations decreased dramatically and pH values decreased slightly (Figure 4.2). This could be due to Fe-carbonate precipitation within the sediment or the oxidation of effluent Fe^{2+} after draining from the sediment—a consequence of low O_2 levels in the anaerobic chamber after passing items through the air-lock chamber. Both of these processes would slightly reduce pH. The low initial effluent pH value from the biotic sediment (~6.4; Figure 4.2A), in contrast to the initial effluent pH from the control sediment (~6.9; Figure 4.2A), could be due to the bacteria consuming the remaining O_2 from the pore fluid and sediments before our first pH measurement and the beginning of Fe^{3+} reduction. Therefore, the pore fluid

geochemistry from the biotic sediment stands in stark contrast to that of the control sediment.

4.5.2. Carbonate Diagenesis

The key differences in the spatial distributions of Ca, Mg, and Fe between the control and biotic sediments were further explored using multicolor composite images (Figure 4.7). In the biotic sediment, Ca, Mg, and Fe are closely associated with each other in multiple small clusters (Figure 4.7B), whereas in the control sediment, Ca, Mg, and Fe appear to be evenly spaced and not associated with each other (Figure 4.7A). Interestingly, clusters of Ca, Mg, and Fe in the biotic sample are typically in close proximity to rod-like structures composed of Fe and Mg and ~1-2 μm in length (white arrows in Figures 4.5 and 4.7), which are not observed in the control sediment (Figures 4.5 and 4.7). These rod-like structures have similar shapes and sizes to the *Shewanella* cells previously observed by Zeng and Tice (2018) and could therefore be Fe and Mg encrusted *Shewanella* cells. In fact, Fe^{2+} and Mg can even be adsorbed to cell surfaces and extracellular polymeric substances (EPS) secreted by cells (Jaisi et al., 2007; Liu et al., 2001b; Thomas and Rice, 2014; Tourney and Ngwenya, 2014). Given the proximity to these potential encrusted cells, clusters of Ca, Mg, and Fe could be carbonate precipitates.

Amorphous carbonates could be precipitated in the biotic sediment inside the area of the dashed box in Figure 4.7. The rhombohedral Fe-rich grain inside this area is likely crystalline goethite as evidenced by its crystal habit, high Fe content, and high total weight percentages (Figures 4.5F and 4.6N) and the presence of goethite in

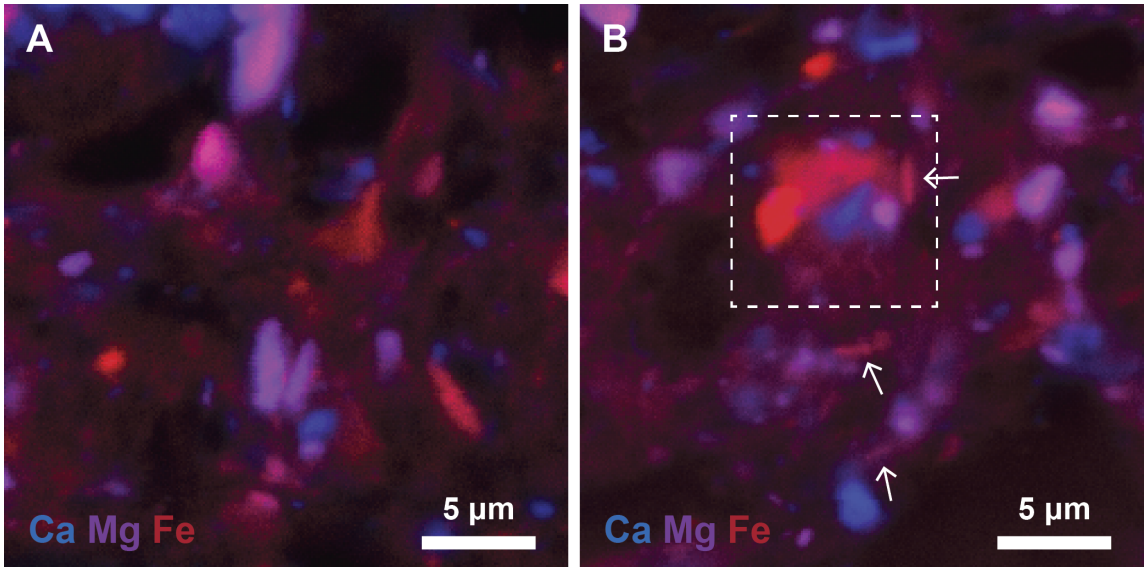

Figure 4.7 Multicolor composite images from Ca, Mg, and Fe elemental maps for the (A) control and (B) biotic sediments. Dashed box indicates the matching location of the dashed box in Figure 4.5 and is the area with a rhombohedral Fe-rich grain, potential amorphous carbonates, and potentially encrusted cell. White arrows point to potentially encrusted cells with nearby clusters of diffuse Ca, Mg, and Fe enrichments.

XRD spectra (Figure 4.3). While siderite has similar crystal habit and Fe content, it was not observed in XRD spectra (Figure 4.3; although poorly crystalline siderite could have oxidized before XRD analyses) and would have lower total weight percentages due to the carbon in its crystal structure (carbon not measured by the electron microprobe). Directly adjacent to this goethite grain is an area with high Fe, Ca, and Mg in close proximity to a potentially encrusted cell (Figure 4.7B). However, in this region, these elements appear diffuse without clear grain boundaries (Figure 4.7B), and the total weight percentages for this area are quite low (Figure 4.6N), indicating a lack of crystallinity. In this local region (dashed box in Figure 4.7B), Fe^{3+} from the goethite

surface was likely reduced (e.g., Liu et al., 2001a), which liberated Fe^{2+} and increased carbonate mineral saturation (Equation 4.2). Previous work has shown that Fe- and Ca-carbonate precipitation is typically initiated by an amorphous precursor phase (Jiang and Tosca, 2019; Montes-Hernandez and Renard, 2016; Sel et al., 2012). In fact, our XRD results for the biotic sediment show an increase in amorphous material (3–8 °2θ), no indication of siderite precipitation, no excess calcite, and a small increase in dolomite (Figure 4.3). Not only do we observe a cluster of diffuse Ca, Mg, and Fe (potential amorphous carbonate) near the goethite grain and potentially encrusted cell (inside dashed box in Figure 4.7B), but we also observe similar clusters near other potentially encrusted cells and throughout the biotic sediment (Figures 4.5D, 4.5F, and 4.7B). We therefore suggest that amorphous carbonates of varying Ca, Mg, and Fe compositions precipitated in our biotic sample, especially in areas with close proximity to potentially encrusted cells, and that crystalline carbonates did not precipitate—with the exception of potentially a minor amount of excess dolomite (Figure 4.3).

4.5.3. Smectite-to-Illite Reaction

XRD results show key differences in clay mineralogy between the control and biotic sediments (Figure 4.3). Most notably, illite peaks in the bulk biotic sediment XRD pattern exhibit increased relative intensities compared to the control sediment (8.8 °2θ and 27.8 °2θ; Figure 4.2), indicating the bulk biotic sediment has an increased abundance of illite. Conversely, XRD patterns for the bulk biotic sediment exhibit lower relative intensities for a smectite-illite mixed layer peak (27.4 °2θ; Figure 4.2), indicating a decreased abundance of smectite-illite mixed layered clay minerals in the

bulk biotic sediment. The potential smectite peak at 6.1 °2θ (could also be a chlorite peak) is difficult to interpret due to the increased abundance of amorphous material in the biotic sediment (Figure 4.3). While this amorphous material may be from amorphous carbonate precipitation, it may in part be due to decreased smectite crystallinity. The increase in illite, decrease in smectite-illite mixed layered clay minerals, and potentially less crystalline smectite are likely due to microbial reduction of Fe^{3+} from the structural sites of smectites and smectite-illite mixed layered clay minerals, which induced the smectite to illite transformation (e.g., Jaisi et al., 2011; Kim et al., 2004; Zhang et al., 2007).

The effects of the S-I reaction on the elemental composition of representative matrix clay minerals in the control and biotic sediments were explored using electron microprobe elemental maps. Our results show that the biotic sediment had a slight increase in normalized Al_2O_3, an increase in K_2O, a decrease in normalized SiO_2, and an increase in the Al_2O_3/SiO_2 ratio compared to the control sediment (inside dashed boxes in Figure 4.6). All of these results are consistent with microbially induced S-I transformation (Equation 4.1; Dong et al., 2003; Hower et al., 1976; Koo et al., 2014; Koo et al., 2016; Vorhies and Gaines, 2009). In contrast, our bulk elemental data obtained via μXRF mapping shows little change between the control and biotic sediments (Table 4.1; Figure 4.4), indicating that bulk elemental data may not be useful in identifying the S-I reaction in natural sediment and that the loss of Si during the S-I reaction has little effect on the bulk elemental composition due to the abundance of silt-size quartz grains.

The elemental composition of the control and biotic sediments were further explored at a finer scale using EDS spot data of individual clay minerals. A cross plot of Al/Si versus K/(K+2Ca) shows that the biotic sediment plot at higher Al/Si values (~0.35–0.53) than those from the control sediment (~0.25–0.40), while the two sediments have a small zone of overlap (0.35–0.40; Figure 4.8). Likewise, data from the biotic sediment on average plots at higher K/(K+2Ca) values than the control sediment, however, there is much more overlap along this axis (Figure 4.8). Previous work has shown that microbially induced S-I reaction is accompanied with an increase in Al/Si and K/(K+2Ca) (Kim et al., 2019; Koo et al., 2014; Koo et al., 2016). In fact,

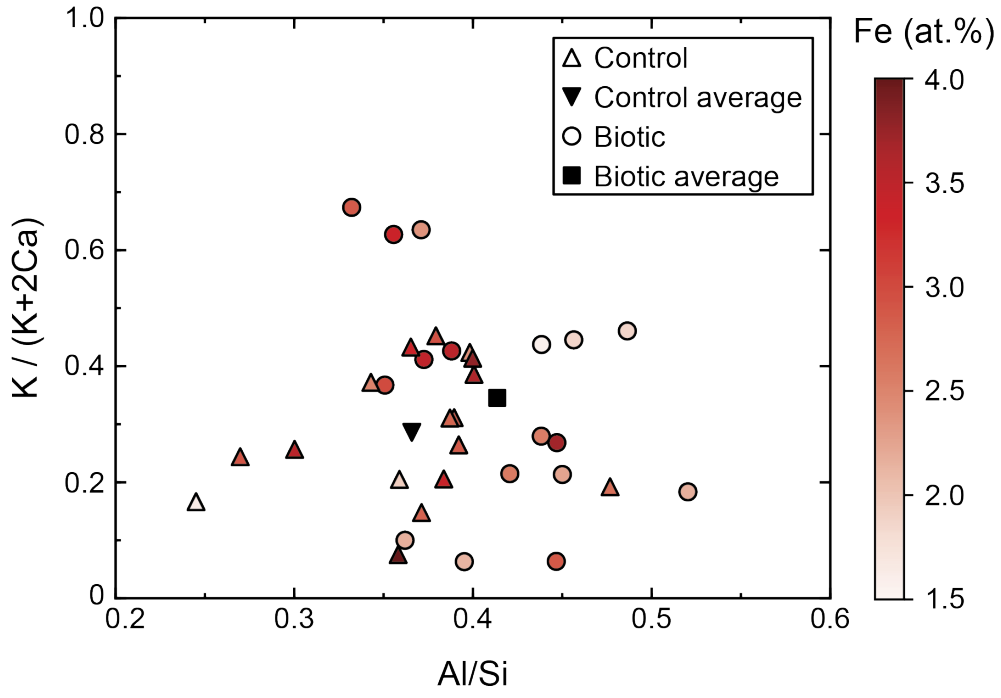

Figure 4.8 Plot of Al/Si versus K/(K+2Ca) for the control (triangles) and biotic (circles) sediments. Markers are shaded by Fe concentrations (Fe at.% scale to the right).

Koo et al. (2014) and Kim et al. (2019) demonstrated increases in Al/Si and K/(K+2Ca) due to microbially induced S-I transformation at the nanometer scale within individual clay packets. Here, we show similar increases in Al/Si and K/(K+2Ca) due to microbially induced S-I transformation, but we do this at the μm scale for entire clay packets (single clay grains). Thus, we extend the scale at which elemental spot analysis can identify the indicators of microbially induced S-I transformation. Moreover, not only does the biotic sediment data plot at higher Al/Si and K/(K+2Ca) values than the control sediment data (average values plotted for each dataset in Figure 4.8), but Fe concentrations generally decrease towards higher Al/Si values and from the control sediment to the biotic sediment (Figure 4.8). This points towards microbial reduction of structurally bound Fe^{3+} in clay minerals as the cause of the S-I transformation.

4.6. Implications

While microbially induced S-I transformation has been experimentally explored using pure, homogeneous Fe-rich smectites (Kim et al., 2004; Koo et al., 2014; Koo et al., 2016; Zhang et al., 2007), recognition of this process in naturally occurring sediments is difficult. Here, we further the understanding of microbial S-I transformation by performing experiments with natural sediments collected from the Gulf of Mexico and by showing that this process can be identified at multiple scales and with multiple techniques. Our work therefore bridges the gap between previous experimental work and recognition of this process in natural environments. Moreover, we show that this process may be accompanied by authigenic carbonate precipitation in ferruginous sediments. For example, in sediments, Fe reducing bacteria could solubilize, liberate, and reduce Fe^{3+}

from the crystal lattice of smectites (Kostka et al., 2002; Kostka et al., 1999; Kostka et al., 1996; Weber et al., 2006), which would simultaneously induce the S-I reaction and increase carbonate mineral saturation. Therefore, the S-I reaction may occur in close proximity to Fe-rich authigenic carbonates in natural sediments.

While the global scope of the S-I reaction is likely controlled by increased temperature, pressure, and time during burial, recognition of microbially induced S-I transformation could have important local and regional consequences. For instance, the conversion of smectite to illite releases water, which can generate overpressure in the subsurface if the water cannot drain (Brown et al., 2001; Tremosa et al., 2020). Finally, this reaction could lubricate faults, via water release, and increase movement (Lauer et al., 2017).

4.7. References

ASTM D2435, Standard test methods for one-dimensional consolidation properties of soils using incremental loading, ASTM International, West Conshohocken, PA, 2020, www.astm.org.

Ahn, J. H., and Peacor, D. R., 1989, Illite/Smectite from Gulf Coast Shales: A Reappraisal of Transmission Electron Microscope Images: Clays and Clay Minerals, v. 37, p. 542-546, htpps://doi.org/10.1346/CCMN.1989.0370606.

Boudreau, B. P., and Canfield, D. E., 1988, A provisional diagenetic model for pH in anoxic porewaters: Application to the FOAM Site: Journal of Marine Research, v. 46, p. 429-455, https://doi.org/10.1357/002224088785113603.

Brown, K. M., Saffer, D. M., and Bekins, B. A., 2001, Smectite diagenesis, pore-water freshening, and fluid flow at the toe of the Nankai wedge: Earth and Planetary Science Letters, v. 194, p. 97-109, https://doi.org/10.1016/S0012-821X(01)00546-5.

Burst, J. F., 1969, Diagenesis of Gulf Coast Clayey Sediments and Its Possible Relation to Petroleum Migration1: AAPG Bulletin, v. 53, p. 73-93, https://doi.org/10.1306/5D25C595-16C1-11D7-8645000102C1865D.

Dong, H., Kostka, J. E., and Kim, J., 2003, Microscopic Evidence for Microbial Dissolution of Smectite: Clays and Clay Minerals, v. 51, p. 502-512, 10.1346/CCMN.2003.0510504.

Eberl, D., and Hower, J., 1976, Kinetics of illite formation: GSA Bulletin, v. 87, p. 1326-1330, 10.1130/0016-7606(1976)87<1326:KOIF>2.0.CO;2.

Fu, Q. S., Boonchayaanant, B., Tang, W., Trost, B. M., and Criddle, C. S., 2008, Simple menaquinones reduce carbon tetrachloride and iron (III): Biodegradation, v. 20, p. 109, https://doi.org/10.1007/s10532-008-9204-4.

Hower, J., Eslinger, E. V., Hower, M. E., and Perry, E. A., 1976, Mechanism of burial metamorphism of argillaceous sediment: 1. Mineralogical and chemical evidence: GSA Bulletin, v. 87, p. 725-737, https://doi.org/10.1130/0016-7606(1976)87<725:MOBMOA>2.0.CO;2.

Jaisi, D. P., Dong, H., and Liu, C., 2007, Kinetic Analysis of Microbial Reduction of Fe(III) in Nontronite: Environmental Science & Technology, v. 41, p. 2437-2444, https://doi.org/10.1021/es0619399.

Jaisi, D. P., Eberl, D. D., Dong, H., and Kim, J., 2011, The Formation of Illite from Nontronite by Mesophilic and Thermophilic Bacterial Reaction: Clays and Clay Minerals, v. 59, p. 21-33, https://doi.org/10.1346/CCMN.2011.0590105.

Jiang, C. Z., and Tosca, N. J., 2019, Fe(II)-carbonate precipitation kinetics and the chemistry of anoxic ferruginous seawater: Earth and Planetary Science Letters, v. 506, p. 231-242, https://doi.org/10.1016/j.epsl.2018.11.010.

Kim, J., Dong, H., Seabaugh, J., Newell, S. W., and Eberl, D. D., 2004, Role of Microbes in the Smectite-to-Illite Reaction: Science, v. 303, p. 830-832,

Kim, J., Dong, H., Yang, K., Park, H., Elliott, W. C., Spivack, A., Koo, T.-h., Kim, G., Morono, Y., Henkel, S., Inagaki, F., Zeng, Q., Hoshino, T., and Heuer, V. B., 2019, Naturally occurring, microbially induced smectite-to-illite reaction: Geology, v. 47, p. 535-539, https://doi.org/10.1130/G46122.1.

Koo, T.-h., Jang, Y.-n., Kogure, T., Kim, J. H., Park, B. C., Sunwoo, D., and Kim, J.-w., 2014, Structural and chemical modification of nontronite associated with microbial Fe(III) reduction: Indicators of “illitization”: Chemical Geology, v. 377, p. 87-95, https://doi.org/10.1016/j.chemgeo.2014.04.005.

Koo, T.-h., Lee, G., and Kim, J.-w., 2016, Biogeochemical dissolution of nontronite by Shewanella oneidensis MR-1: Evidence of biotic illite formation: Applied Clay Science, v. 134, p. 13-18, https://doi.org/10.1016/j.clay.2016.03.030.

Kostka, J. E., Dalton, D. D., Skelton, H., Dollhopf, S., and Stucki, J. W., 2002, Growth of Iron(III)-Reducing Bacteria on Clay Minerals as the Sole Electron Acceptor and Comparison of Growth Yields on a Variety of Oxidized Iron Forms: Applied and Environmental Microbiology, v. 68, p. 6256-6262, 10.1128/aem.68.12.6256-6262.2002.

Kostka, J. E., Haefele, E., Viehweger, R., and Stucki, J. W., 1999, Respiration and Dissolution of Iron(III)-Containing Clay Minerals by Bacteria: Environmental Science & Technology, v. 33, p. 3127-3133, 10.1021/es990021x.

Kostka, J. E., Stucki, J. W., Nealson, K. H., and Wu, J., 1996, Reduction of structural Fe(III) in smectite by a pure culture of Shewanella Putrefaciens strain MR-1: Clays and Clay Minerals, v. 44, p. 522-529,

Lauer, R. M., Saffer, D. M., and Harris, R. N., 2017, Links between clay transformation and earthquakes along the Costa Rican subduction margin: Geophysical Research Letters, v. 44, p. 7725-7732, https://doi.org/10.1002/2017GL073744.

Lavoie, D. M., Baerwald, R. J., Hulbert, M. H., and Bennett, R. H., 1996, A drinking-straw mini-corer for sediments: Journal of sedimentary Research, v. 66, p. 1030, https://doi.org/10.2110/jsr.66.1030.

Liu, C., Kota, S., Zachara, J. M., Fredrickson, J. K., and Brinkman, C. K., 2001a, Kinetic Analysis of the Bacterial Reduction of Goethite: Environmental Science & Technology, v. 35, p. 2482-2490, https://doi.org/10.1021/es001956c.

Liu, C., Zachara, J. M., Gorby, Y. A., Szecsody, J. E., and Brown, C. F., 2001b, Microbial Reduction of Fe(III) and Sorption/Precipitation of Fe(II) on Shewanella putrefaciens Strain CN32: Environmental Science & Technology, v. 35, p. 1385-1393, https://doi.org/10.1021/es0015139.

Lovley, D. R., Phillips, E. J. P., and Lonergan, D. J., 1989, Hydrogen and Formate Oxidation Coupled to Dissimilatory Reduction of Iron or Manganese by Alteromonas putrefaciens: Applied and Environmental Microbiology, v. 55, p. 700-706, https://doi.org/10.1128/aem.55.3.700-706.1989.

Marsili, E., Baron, D. B., Shikhare, I. D., Coursolle, D., Gralnick, J. A., and Bond, D. R., 2008, Shewanella secretes flavins that mediate extracellular electron transfer: Proceedings of the National Academy of Sciences, v. 105, p. 3968-3973, https://doi.org/10.1073/pnas.0710525105.

Mills, N. T., Reece, J. S., and Tice, M. M., 2021, Clay minerals modulate early carbonate diagenesis: Geology, v. 49, p. 1015-1019, https://doi.org/10.1130/G48713.1.

Montes-Hernandez, G., and Renard, F., 2016, Time-Resolved in Situ Raman Spectroscopy of the Nucleation and Growth of Siderite, Magnesite, and Calcite and Their Precursors: Crystal Growth & Design, v. 16, p. 7218-7230, https://doi.org/10.1021/acs.cgd.6b01406.

O'Reilly, S. E., Watkins, J., and Furukawa, Y., 2005, Secondary mineral formation associated with respiration of nontronite, NAu-1 by iron reducing bacteria: Geochemical Transactions, v. 6, p. 67, https://doi.org/10.1186/1467-4866-6-67.

Pevear, D. R., 1999, Illite and hydrocarbon exploration: Proceedings of the National Academy of Sciences, v. 96, p. 3440, htpps://doi.org/10.1073/pnas.96.7.3440.

Pytte, A. M., and Reynolds, R. C., The Thermal Transformation of Smectite to Illite, *in* Proceedings Thermal History of Sedimentary Basins, New York, NY, 1989// 1989, Springer New York, p. 133-140.

Reece, J. S., 2021, The Impact of Grain Size on the Hydromechanical Behavior of Mudstones: Geochemistry, Geophysics, Geosystems, v. 22, p. 1-23, https://doi.org/10.1029/2021GC009732.

Reimers, C. E., Ruttenberg, K. C., Canfield, D. E., Christiansen, M. B., and Martin, J. B., 1996, Porewater pH and authigenic phases formed in the uppermost sediments of the Santa Barbara Basin: Geochimica et Cosmochimica Acta, v. 60, p. 4037-4057, https://doi.org/10.1016/S0016-7037(96)00231-1.

Santagata, M., and Kang, Y. I., 2007, Effects of geologic time on the initial stiffness of clays: Engineering Geology, v. 89, p. 98-111, https://doi.org/10.1016/j.enggeo.2006.09.018.

Sel, O., Radha, A. V., Dideriksen, K., and Navrotsky, A., 2012, Amorphous iron (II) carbonate: Crystallization energetics and comparison to other carbonate minerals related to CO2 sequestration: Geochimica et Cosmochimica Acta, v. 87, p. 61-68, https://doi.org/10.1016/j.gca.2012.03.011.

Stucki, J. W., and Kostka, J. E., 2006, Microbial reduction of iron in smectite: Comptes Rendus Geoscience, v. 338, p. 468-475, http://dx.doi.org/10.1016/j.crte.2006.04.010.

Thomas, K. J., and Rice, C. V., 2014, Revised model of calcium and magnesium binding to the bacterial cell wall: BioMetals, v. 27, p. 1361-1370, https://doi.org/10.1007/s10534-014-9797-5.

Tourney, J., and Ngwenya, B. T., 2014, The role of bacterial extracellular polymeric substances in geomicrobiology: Chemical Geology, v. 386, p. 115-132, https://doi.org/10.1016/j.chemgeo.2014.08.011.

Tremosa, J., Gailhanou, H., Chiaberge, C., Castilla, R., Gaucher, E. C., Lassin, A., Gout, C., Fialips, C., and Claret, F., 2020, Effects of smectite dehydration and illitisation on overpressures in sedimentary basins: A coupled chemical and thermo-hydro-mechanical modelling approach: Marine and Petroleum Geology, v. 111, p. 166-178, https://doi.org/10.1016/j.marpetgeo.2019.08.021.

Uramoto, G.-I., Morono, Y., Uematsu, K., and Inagaki, F., 2014, An improved sample preparation method for imaging microstructures of fine-grained marine sediment using microfocus X-ray computed tomography and scanning electron microscopy: Limnology and Oceanography: Methods, v. 12, p. 469-483, https://doi.org/10.1128/JB.186.23.8096-8104.200410.4319/lom.2014.12.469.

van der Pluijm, B., 2011, Natural fault lubricants: Nature Geoscience, v. 4, p. 217-218, https://doi.org/10.1038/ngeo1126.

Vorhies, J. S., and Gaines, R. R., 2009, Microbial dissolution of clay minerals as a source of iron and silica in marine sediments: Nature Geoscience, v. 2, p. 221-225, https://doi.org/10.1038/ngeo441.

Weber, K. A., Achenbach, L. A., and Coates, J. D., 2006, Microorganisms pumping iron: anaerobic microbial iron oxidation and reduction: Nature Reviews Microbiology, v. 4, p. 752-764, https://doi.org/10.1038/nrmicro1490.

Zeng, Z., and Tice, M. M., 2014, Promotion and nucleation of carbonate precipitation during microbial iron reduction: Geobiology, v. 12, p. 362-371, https://doi.org/10.1111/gbi.12090.

Zeng, Z., and Tice, M. M., 2018, Electron Transfer Strategies Regulate Carbonate Mineral and Micropore Formation: Astrobiology, v. 18, p. 28-36, https://doi.org/10.1089/ast.2016.1560.

Zhang, G., Dong, H., Kim, J., and Eberl, D. D., 2007, Microbial reduction of structural Fe3+ in nontronite by a thermophilic bacterium and its role in promoting the smectite to illite reaction: American Mineralogist, v. 92, p. 1411-1419, https://doi.org/10.2138/am.2007.2498.

5. CONCLUSIONS

The objective of this dissertation was to utilize numerical modeling, experimental, and analytical techniques to understand interactions between microorganisms and fine-grained sediments during the early stages of burial and diagenesis. The key conclusions reached in this dissertation are outlined below.

In Chapter 2, we found that clay minerals enhance carbonate precipitation in sediment pore fluids during O_2 and SO_4^{2-} reduction and inhibit carbonate precipitation during Fe^{3+} reduction and CH_4 production, but only when pore fluid pH and clay mineral pK_a values are within ~2 log units of one another. Therefore, clay minerals could significantly modify the environmental conditions and settings in which early diagenetic carbonate precipitation occurs. In Phanerozoic marine sediments—where O_2 and SO_4^{2-} reduction have been the main oxidants of marine sedimentary organic carbon—clay minerals have likely inhibited carbonate dissolution and promoted precipitation of authigenic carbonate.

In Chapter 3, we found that microorganisms caused a systematic, yet small increase in the compression index of fine-grained sediments. Changes in permeability caused by microorganisms, while relatively minor, were greater for our sediment sample with a larger average grain size compared to our sample with a smaller average grain size. Additionally, the effect of microorganisms on permeability is greater at higher porosities and lower vertical effective stresses. We suggest that the effectiveness of microorganisms at altering fluid flow in fine-grained sediments is dependent on burial

depth (porosity as a function of vertical effective stress) and the grain size, pore and pore throat size, and specific surface area of a sediment. Characterizing the effects of microorganisms on the hydromechanical properties of fine-grained sediments can further our understanding of the controls on pore pressure near the sediment-water interface in marine environments and aid in bioclogging practices around contaminated sites in terrestrial environments.

In Chapter 4, we found that microorganisms increased the abundances of illite and amorphous carbonates and decreased the abundance of smectite-illite mixed layered clay minerals in our sediment samples. Elemental mapping and energy dispersive spectroscopy data show that microorganisms decreased clay mineral Si, increased clay mineral Al (minimally increased), K, and Al/Si, and caused close spatial relationships between Ca, Mg, and Fe in our sediment samples. We suggest that Fe^{3+} was reduced from the crystal lattice of smectite and smectite-illite mixed layered clay minerals by microorganisms, which promoted the smectite-to-illite reaction, and that Fe reduction promoted the precipitation of amorphous carbonate minerals. Our results further the understanding of microbial smectite-to-illite transformation by performing experiments with natural sediments and showing that this process can be identified at multiple scales and with multiple techniques. We therefore bridge the gap between observations of this process in culture experiments using pure clay minerals and those made in natural environments.

APPENDIX A

SUPPLEMENTAL MATERIAL FOR CHAPTER 2

Materials

Two bulk sediment powders are created using homogenized, natural sediments collected from Integrated Ocean Drilling Program (IODP) sediment cores. They include the Nankai and Gulf of Mexico sediment powders. The Nankai sediment originates from the Nankai Trough, offshore Japan, and was collected during IODP Expedition 322 at Site C0011 (main text Figure 2.1A). This sample is from two lithologic units composed of hemipelagic muds at depths ranging between 580-865 m below sea floor (mbsf; Reece et al., 2013). The Gulf of Mexico sediment was collected from the Ursa region in the Gulf of Mexico during IODP Expedition 308 at Site U1324 (main text Figure 2.1B). This sample comes from two distinct lithologic units with the first being composed of hemipelagic muds at depths ranging between 4-32 mbsf and the second being composed of silt and mud overbank deposits at depths ranging between 493-502 mbsf (Flemings et al., 2006). After collection, the samples were individually air-dried, disaggregated into clay- and silt-sized particles, and homogenized into two distinct bulk sediment powders.

Material Characterization Methods

Particle Size Analysis

Particle size analysis is carried out for the Nankai and Gulf of Mexico sediments using the hydrometer method as specified by ASTM D7928-17 (ASTM International, 2017). This method utilizes principles from Stoke's law, namely that larger and denser

particles fall out of a sediment suspension faster than smaller and less dense particles. A 1L sediment-water suspension was created in a graduated cylinder by mixing 50g of sediment and 5g of sodium hexametaphosphate (dispersant) with nanopure water. After thoroughly mixing the sediment-water suspension, timed sedimentation begins and the specific gravity of the suspension is measured with a hydrometer at discrete points in elapsed time. Thus, we calculate the sediment mass still in suspension and the particle diameter at that particular time and depth below the suspension surface. Ultimately, results of the hydrometer tests are reported as the percent of sediment in suspension finer than a given particle diameter.

Mineralogy

Mineralogy of the Nankai and Gulf of Mexico sediments was determined by X-ray powder diffraction (XRD). The whole rock and clay-size fraction (particles <2μm) XRD analyses were performed with a Bruker D8 Advance X-ray diffractometer using a CuKα source (λ=0.154 nm) operating at 40 kV and 40 mA. The whole rock XRD patterns were recorded from 2-70° 2θ with a dwell time of 3° 2θ per minute. To obtain the clay-size fraction the bulk sample was first pretreated with 1M sodium acetate at a pH of 5 in an 80°C water bath and 30% hydrogen peroxide to remove all carbonate minerals and organic matter, respectively. The clay-size fraction was then obtained via centrifugation after deflocculation and Na saturation. Ions in the resultant clay-size fraction suspension were removed by dialysis. Subsequently, the clay-size fraction was treated with Mg and K separately then transferred to their respective glass slides for analysis. Clay fraction XRD patterns were recorded from 2-32° 2θ with a dwell time of

3° 2θ per minute. These XRD patters were recorded in the air-dried state and after the Mg saturated sample was treated with glycerol and after the K saturated sample had been heated to 330°C and 550°C. Semi-quantitative analysis was performed using the reference intensity ratio method for the bulk mineralogy and the mineral intensity factor method for the <2μm fraction.

Potentiometric Titrations

Potentiometric titrations were performed in order to obtain pK_a and total acidity values for the Nankai and Gulf of Mexico sediments. To obtain the clay fraction from each sediment sample, the bulk samples were first pretreated with 1M sodium acetate at a pH of 5 in an 80°C water bath and 30% hydrogen peroxide to remove all carbonate minerals and organic matter, respectively. The clay fraction was then obtained for each sample via centrifugation after deflocculation and Na saturation. Ions in the resultant clay fraction suspension were removed by dialysis.

Automated potentiometric titrations were carried out using a Metrohm Titrando 907. Each titration consisted of 0.25g or 0.5g of sample in 50mL of a 0.56M NaCl background solution, which is used to approximate the ionic strength of marine waters. Because our titrations were performed in this 0.56M NaCl solution, we also performed a blank titration and subtracted it from our clay mineral titrations. Prior to each titration the solution pH was adjusted to 3.5 with 2M HCl and during each titration the pH was adjusted up, down, and back up again in the range of 3.5-11 using 0.1 M NaOH (for the up titrations) and 0.1 M HCl (for the down titrations). In each titration, titrant was only added after the pH electrode reached a stability of 0.1mV/s. Each titration solution was

bubbled with N_2 for 30 minutes prior to, and throughout, each titration and the containers were sealed with parafilm to prevent CO_2 contamination. We performed titrations of each sample at two sediment concentrations to investigate whether or not the pK_a and total acidity values change with sediment concentration. The titrations consisting of 0.25g of sediment were performed in duplicate, while the titrations consisting of 0.5g of sediment were performed once.

The pK_a values for the Nankai and Gulf of Mexico sediments were obtained from the experimental data and from a simple surface complexation model. We used Gran Plots to obtain pK_a and clay acidity values from the experimental data. We then calculated pK_a values using a surface complexation model (Stumm, 1992), which is detailed in Davranche et al. (2003). This method calculates the surface charge of a solid for each point in a titration as a function of pH. Then the surface charge and the total concentration of surface species (obtained from the equivalence points in the Gran Plots) can be used to calculate an acid dissociation constant (K_a).

Material Characterization Results

Particle Size Analysis

Hydrometer results for the Nankai and Gulf of Mexico sediments are reported in Table A1. The clay-size fractions (<2μm) for the Nankai and Gulf of Mexico sediments are 56% and 59%, respectively.

Table A1. Hydrometer results showing the particle size distribution for the Nankai and Gulf of Mexico sediments expressed as wt.%.

Sample	% Sand (63-2000μm)	% Silt (2-63μm)	% Clay (<2μm)
Nankai	0	44	56
Gulf of Mexico	0	41	59

Mineralogy

The mineralogies of the bulk and clay-size (<2μm fraction) fractions, determined by XRD analyses, are presented in Tables A2 and A3, respectively. Most notably, the Nankai sediment contains more smectite than illite in the <2μm fraction, while the Gulf of Mexico sediment contains more illite than smectite in the <2μm fraction (Table A3). However, both sediments contain a mixture of smectite, illite, and kaolinite (Table A3).

Table A2. Bulk mineralogy of the Nankai and Gulf of Mexico sediments expressed as wt.%.

Sample	Quartz	Feldspar	Calcite	Dolomite	Pyrite	Smectite	Illite	Kaolinite	Chlorite
Nankai	33	16	2	-	1	22	14	9	3
Gulf of Mexico	38	7	6	15	-	10	16	6	2

Table A3. Mineralogy of the clay-size (<2μm) fraction shown as relative wt.% (P = present but not quantified in the <2μm fraction).

Sample	Smectite	Illite	Kaolinite	Chlorite
Nankai	48	31	21	P
Gulf of Mexico	32	49	19	P

Potentiometric Titrations

The experimental pK_a and total acidity values for the Nankai and Gulf of Mexico sediments were obtained from the slopes and x-intercepts, respectively, of Gran Plots (Figure A1). The pK_a values for both sediments from the 0.25g, 0.25g duplicate, and 0.5g titration runs and from the up, down, and second up titrations in each of those runs are presented in Table A4. The total clay acidity values (in mmol g^{-1}) from the first up titrations in the 0.25g, 0.25g duplicate, and 0.5g titration runs are also presented in Table A4. The Gran Plots in Figure A1 show that the slopes between the 0.25g and 0.5g titrations are the same and that the equivalence points (x-intercept) for the 0.5g titrations are twice that of the 0.25g titrations meaning that the clay acidity values in mmol g^{-1} are the same. For a given pK_a value, we report the average pK_a from the up, down, and second up titrations for the titrations performed (0.25g, 0.25g duplicate, and 0.5g titrations) along with the range of pK_a values (expressed as ± from the average). The Nankai sediment yielded clay mineral pK_a values of pK_{a1}=4.28±0.06, pK_{a2}=6.64±0.13, pK_{a3}=8.71±0.05 with respective clay acidity values of 0.18 mmol g^{-1}, 0.05 mmol g^{-1}, and 0.07 mmol g^{-1}. The Gulf of Mexico sediment yielded clay mineral pK_a values of pK_{a1}=4.79±0.06, pK_{a2}=6.92±0.08, pK_{a3}=8.96±0.06 with respective clay acidity values of 0.04 mmol g^{-1}, 0.03 mmol g^{-1}, and 0.05 mmol g^{-1}. The Nankai sample had a pK_a value with a larger range (pK_{a2} for Nankai). This is because two of the second up titrations yielded values that were outside of an otherwise smaller range (Table A4). We performed a regression analysis in an attempt to determine if our Gran Plot slopes (and consequently pK_a values) were statistically distinguishable between the 0.25g, 0.25g

duplicate, and 0.5g titration runs and between the first and second up titrations in each of those runs (for example, for the first pK_a value from the Nankai sample 6 slopes were used). The regression analysis used dummy terms to test for differences in intercepts and interaction terms to test for differences in slopes. In each regression a few p-values were below 0.05, indicating that not all of the slopes were statistically the same. This is most likely because of slight variations between the 0.25g, 0.25g duplicate, and 0.5g titration runs and between the first and second up titrations in each of those runs. It could also indicate a small amount of clay alteration during the course of an up-down-up titration experiment. However, this alteration was minimal as the pK_a values calculated from Gran Plot slopes that had low p-values were still within ±0.08 log units of average values, with the exception of one pK_a value (pK_{a2} from Nankai) that was farther from the averages (±0.13). While the regression analysis suggests that the slopes (pK_a values) are statistically different, a pK_a difference of 0.08 log units, or even 0.15 log units, does not produce significantly different model results, and it is unlikely to drive geologically significant differences in natural sediments.

The modeled pK_a values were obtained from the first up titrations in each of the 0.25g, 0.25g duplicate, and 0.5g titration runs and are reported as averages with their respective ranges (expressed as ± from the average). The surface complexation model yielded clay mineral pK_a values of pK_{a1}=4.26±0.05, pK_{a2}=6.65±0.04, pK_{a3}=8.75±0.05 for the Nankai sediment and pK_a values of pK_{a1}=4.86±0.02, pK_{a2}=6.93±0.03, pK_{a3}=8.92±0.03 for the Gulf of Mexico sediment (Table A4). These are the pK_a values

reported in the main text. The pK_a values obtained from Gran Plots are all within ±0.07 log units of the pK_a values from the surface complexation model (Table A4).

As the total clay acidity values displayed in Table A4 represent a sediment with a porosity of ~99.8% (0.25g in 50mL solution), we obtain model input values for total clay acidity by upscaling the values in Table A4 to represent freshly deposited muddy sediments with a porosity of ~70% (e.g., Boggs, 2009; Tucker, 2001). This is done by using the following equation: upscaled clay acidity value (mM) = clay acidity (mmol g^{-1}) * ((1-porosity) / porosity) * (1000 (cm^3) / 1 (L)) * clay density (g cm^{-3}) * the fraction of the sediment composed of clay minerals. We use the lowest reported clay density value from Osipov (2012) for a hydrated clay mineral (1.4 g cm^{-3}), which places our upscaled clay acidity values at a minimum.

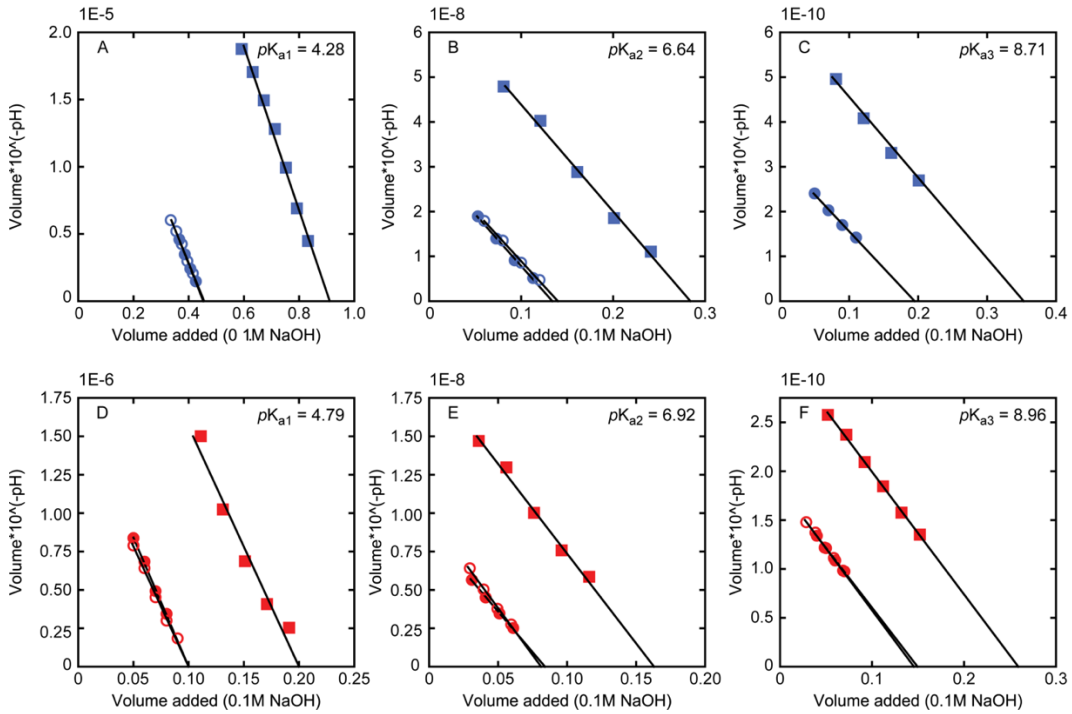

Figure A1. Gran plots showing titration data for the Nankai (A-C) and Gulf of Mexico (D-F) sediments. Clay mineral pK_a values are listed in the top right corner of each plot and were obtained from the slopes of the data, while the total clay acidity values were obtained from the x-intercept. Solid circles = 0.25g titrations, hollow circles = 0.25g duplicate titrations, solid squares = 0.5g titrations.

Table A4. Experimental and modeled titration results for the Nankai and Gulf of Mexico sediments. The experimental pK_a values for the 1st alkalimetric, acidimetric, and 2nd alkalimetric titrations and total clay acidity values for the 1st alkalimetric titrations (obtained from the Gran Plots in Figure A2) are shown. The modeled pK_a values for the 1st alkalimetric titrations are also shown (obtained from a simple surface complexation model). TCA= total clay acidity, Up = alkalimetric titration, Down = acidimetric titration, dup = duplicate, GP = Gran Plot, SCM = surface complexation model, X = poor trend on Gran Plot near end of titration (i.e., high pH values on alkalimetric titration and low pH values on acidimetric titration).

Sample	Test	pK_{a1} GP	pK_{a1} SCM	TCA (mmol g^{-1})	pK_{a2} GP	pK_{a2} SCM	TCA (mmol g^{-1})	pK_{a3} GP	pK_{a3} SCM	TCA (mmol g^{-1})
Nankai										
	1st Up 0.25g	4.28	4.29	0.18	6.63	6.68	0.054	8.66	8.79	0.078
	1st Up 0.25g dup	4.29	4.21	0.18	6.65	6.65	0.056	X	8.70	X
	1st Up 0.5g	4.22	4.29	0.18	6.62	6.61	0.054	8.68	8.76	0.071
	Down 0.25g	4.29			6.68			8.72		
	Down 0.25g dup	4.33			6.70			8.66		
	Down 0.5g	4.34			6.61			8.70		
	2nd Up 0.25g	4.23			6.61			8.70		
	2nd Up 0.25g dup	4.27			6.53			8.76		
	2nd Up 0.5g	4.26			6.51			X		
Gulf of Mexico										
	1st Up 0.25g	4.77	4.87	0.04	6.98	6.90	0.032	8.91	8.94	0.061
	1st Up 0.25g dup	4.81	4.84	0.04	6.91	6.96	0.032	8.90	8.92	0.061
	1st Up 0.5g	4.81	4.87	0.04	6.94	6.93	0.033	8.90	8.89	0.051
	Down 0.25g	4.76			6.95			8.99		
	Down 0.25g dup	4.77			6.94			8.95		
	Down 0.5g	X			6.99			9.01		
	2nd Up 0.25g	4.80			6.85			X		
	2nd Up 0.25g dup	4.75			6.86			9.00		
	2nd Up 0.5g	4.85			6.84			9.01		

Biogeochemical Model

The model assumes a pore fluid composition that is similar to modern seawater and the model uses effective speciation terms appropriate for seawater composition and ionic strength. We checked for the influence of ion pairs and when ion pairs were found to have an insignificant effect on pore fluid pH and *SI* they were dropped from our calculations. We also assumed that all clay mineral effective charge sites are available for H^+ exchange. Initial conditions are the initial pH (pH_0) and saturation index (SI_0); model parameters are the acid dissociation constants (pK_a) and the total acidity values of the clay minerals (concentration of sites that can be protonated or deprotonated).

Aerobic Respiration

Aerobic respiration is driven by microorganisms as they utilize oxygen (O_2) as an electron acceptor and oxidize organic carbon (Equation A1; e.g., Froelich et al., 1979). We model this reaction by defining the reaction progress (x) as the total amount of O_2 reduced. Using the stoichiometry from Equation A1, the total carbon (CT) in the system is equal to the initial dissolved inorganic carbon (DIC_0) plus the reaction progress (x) (Equation A2).

$$CH_2O + O_2 \rightarrow CO_2 + H_2O \qquad (A1)$$

$$CT = DIC_0 + x = [H_2CO_3^*] + [HCO_3^-] + [CO_3^{2-}] \qquad (A2)$$

To incorporate clay minerals in our model, we account for the deprotonation (forward reaction in Equation A3) and protonation (reverse reaction in Equation A3) reactions of clay minerals (e.g., Avena et al., 2003; Mitchell and Soga, 2005).

$$[\text{clay: OH}] \leftrightarrow [\text{clay: O}^-] + [H^+] \qquad (A3)$$

Charge balance dictates that the net charge of the system does not change as the reaction progresses. The charged species that undergo a change in concentration as the reaction proceeds are summed on the left side of Equation A4, while the charged species that remain constant throughout the reaction are not included.

$$\frac{d}{dz}([\mathrm{H^+}] - [\mathrm{OH^-}] - [\mathrm{HCO_3^-}] - 2[\mathrm{CO_3^{2-}}] - [\mathrm{clay{:}O^-}]) = 0 \qquad \text{(A4)}$$

By adding the term [clay:O$^-$] to the charge balance equation we can account for the acid-base properties of clay minerals, and alternatively, by removing this term we are able to model the aerobic respiration reaction alone. We rearrange the charge balance equation and write it in terms of [H$^+$] and constants using equations for speciation (Equations A5-A8) and mass balance (Equations A9 and A10). Subsequently, collecting the term d[H$^+$]/dx to the left side of the equation yields Equation A11.

$$[\mathrm{H^+}][\mathrm{OH^-}] = K_w \qquad \text{(A5)}$$

$$\frac{[H^+][HCO_3^-]}{[H_2CO_3^*]} = K_{a1} \qquad \text{(A6)}$$

$$\frac{[H^+][CO_3^{2-}]}{[HCO_3^-]} = K_{a2} \qquad \text{(A7)}$$

$$\frac{[clay{:}O^-][H^+]}{[clay{:}OH]} = K_{clay} \qquad \text{(A8)}$$

$$clay_{TA} = [clay{:}OH] + [clay{:}O^-] \qquad \text{(A9)}$$

$$\left[\mathrm{H_2CO_3^*}\right] = K_H p\mathrm{CO_2} \qquad \text{(A10)}$$

$$\frac{1}{[\mathrm{H^+}]} \cdot \frac{d[\mathrm{H^+}]}{dx} = (\alpha_{HCO3-} - 2\alpha_{CO32-}) \div ([H^+] + [OH^-] + \alpha_{HCO3-}[H_2CO_3^*] +$$

$$(\alpha_{HCO3-} + 4\alpha_{H2CO3})[CO_3^{2-}] + [clay{:}O^-] \cdot \alpha_{clayOH}) \qquad \text{(A11)}$$

The change in pH with respect to the reaction progress, x, can be described by rewriting the relationship pH = -$\log_{10}[H^+]$ as:

$$\frac{dpH}{dx} = -\frac{1}{ln10} \cdot \frac{1}{[H^+]} \cdot \frac{d[H^+]}{dx} . \quad \text{(A12)}$$

Combining Equations A11 and A12 yields:

$$\frac{dpH}{dx} = -\frac{1}{ln10} \cdot ((\alpha_{HCO3-} - 2\alpha_{CO32-}) \div ([H^+] + [OH^-] + \alpha_{HCO3-}[H_2CO_3^*] + (\alpha_{HCO3-} + 4\alpha_{H2CO3})[CO_3^{2-}] + [clay{:}O^-] \cdot \alpha_{clayOH}) . \quad \text{(A13)}$$

This equation then describes the evolution of the system and makes it possible to model system pH as a function of the amount of oxygen reduced for circumstances with and without clay minerals.

In like manner, we calculate the evolution of carbonate saturation during aerobic respiration. Critical saturation, Ω_c, is expressed in Equation A14 and the change in Ω_c with respect to the reaction progress, x, assuming that $[Ca^{2+}]$ remains constant (i.e., $d[Ca^{2+}]/dx = 0$), is expressed in Equation A15.

$$\Omega_C = \frac{[Ca^{2+}][CO_3^{2-}]}{[K_{sp}]} \quad \text{(A14)}$$

$$\frac{1}{\Omega} \cdot \frac{d\Omega}{dx} = \frac{d[CO_3^{2-}]}{[CO_3^{2-}] \cdot dx} \quad \text{(A15)}$$

The carbonate saturation index, SI, is simply expressed as $SI = \log_{10}\Omega_c$, and the change in SI with respect to the reaction progress, x, can be written as:

$$\frac{dSI}{dx} = \frac{1}{\ln 10} \cdot \frac{1}{\Omega} \cdot \frac{d\Omega}{dx} . \quad \text{(A16)}$$

Combining Equations A15 and A16 yields:

$$\frac{dSI}{dx} = \frac{d[CO_3^{2-}]}{\ln 10 \cdot [CO_3^{2-}] \cdot dx} , \quad \text{(A17)}$$

where values for $[CO_3^{2-}]$ and $d[CO_3^{2-}]/dx$ are obtained from the pH model above (Equations A1-A13). For the case of aerobic respiration, the change in *SI* with respect to the change in the reaction progress can be written as:

$$\frac{dSI}{dx} = \frac{1}{\ln 10 \cdot CT} + (2\alpha_{H2CO3} + \alpha_{HCO3-}) \cdot \frac{dpH}{dx} . \qquad \text{(A18)}$$

These *SI* values can be obtained under circumstances with and without clay minerals present in the system. Thus, for both circumstances we are able to predict *SI* as a function of the amount of oxygen reduced. Equations A19-A22 are used to simplify Equations A11 and A13.

$$\alpha_{H2CO3} = ([H^+]^2 \div K_{a1}) \div (([H^+]^2 \div K_{a1}) + [H^+] + K_{a2}) \qquad \text{(A19)}$$

$$\alpha_{HCO3-} = [H^+] \div (([H^+]^2 \div K_{a1}) + [H^+] + K_{a2}) \qquad \text{(A20)}$$

$$\alpha_{CO32-} = K_{a2} \div (([H^+]^2 \div K_{a1}) + [H^+] + K_{a2}) \qquad \text{(A21)}$$

$$\alpha_{ClayOH} = ([H^+] \div K_{clay}) \div (([H^+] \div K_{clay}) + 1) \qquad \text{(A22)}$$

Iron Reduction

Iron reduction is driven by microorganisms as they utilize Fe^{3+} as an electron acceptor and oxidize organic carbon (Equation A23; Lovley, 1991). This model is adapted from Zeng and Tice (2014). We model this reaction by defining the reaction progress (*y*) as the total amount of iron reduced or the sum of Fe^{2+} species produced (Equation A24). Using the stoichiometry from Equation A23, the total carbon (*CT*) in the system is equal to the initial dissolved inorganic carbon (DIC_0) plus the reaction progress (*y*) divided by 4 (Equation A25).

$$4Fe(OH)_3 + CH_2O + 7H^+ \rightarrow 4Fe^{2+} + HCO_3^- + 10H_2O \qquad \text{(A23)}$$

$$y = [Fe^{2+}] + [FeHCO_3^+] \qquad \text{(A24)}$$

$$CT = DIC_0 + \frac{y}{4} = [\mathrm{H_2CO_3}] + [\mathrm{HCO_3^-}] + [\mathrm{CO_3^{2-}}] + [\mathrm{FeHCO_3^+}] \qquad \text{(A25)}$$

To incorporate clay minerals in our model, we account for the deprotonation (forward reaction in Equation A3) and protonation (reverse reaction in Equation A3) reactions (e.g., Avena et al., 2003; Mitchell and Soga, 2005). Charge balance dictates that the net charge of the system does not change as the reaction progresses. The charged species that undergo a change in concentration as the reaction proceeds are summed on the left side of Equation A26, while the charged species that remain constant throughout the reaction are not included.

$$\frac{d}{dy}([\mathrm{H^+}] + 2[\mathrm{Fe^{2+}}] + [\mathrm{FeHCO_3^+}] - [\mathrm{OH^-}] - [\mathrm{HCO_3^-}] - 2[\mathrm{CO_3^{2-}}] - [\mathrm{clay{:}\,O^-}]) = 0$$

(A26)

By adding the term [clay:O^-] to the charge balance equation we can account for the acid-base properties of clay minerals, and alternatively, by removing this term we are able to model the aerobic respiration reaction alone. We rearrange the charge balance equation and write it in terms of [H^+] and constants using equations for speciation (Equations A5-A8 and A27) and mass balance (Equations A9 and A10). Subsequently, collecting the term $d[\mathrm{H^+}]/dy$ to the left side of the equation yields Equation A28.

$$\frac{FeHCO_3^+}{[Fe^{2+}][HCO_3^-]} = K_b \qquad \text{(A27)}$$

$$\frac{1}{[\mathrm{H}^+]} \cdot \frac{d[\mathrm{H}^+]}{dy} = \left(2 \cdot \alpha_{Fe} + \alpha_{FeHCO3} + \alpha_{FeOH} - \alpha_{FeOH3} + \beta \cdot \left(\frac{0.25 - \alpha_{FeHCO3} - \alpha_{FeCO3}}{(CT-x)(\alpha_{FeHCO3} + \alpha_{FeCO3})}\right)\right) \div$$

$$\left([H^+] + [OH^-] + 2[CO_3^{2-}] + 2y \cdot \alpha_{Fe} \cdot (\alpha_{Fe} + \alpha_{FeOH} + 2 \cdot \alpha_{FeOH2} + 3 \cdot \alpha_{FeOH3}) + y \cdot \right.$$

$$\alpha_{FeHCO3} \cdot (\alpha_{FeCO3} + \alpha_{FeOH} + 2 \cdot \alpha_{FeOH2}) + y \cdot \alpha_{FeOH} \cdot (\alpha_{Fe} + \alpha_{FeOH} - \alpha_{FeOH2} - 2 \cdot$$

$$\alpha_{FeOH3}) + y \cdot \alpha_{FeOH3}(3 \cdot \alpha_{Fe} + 3 \cdot \alpha_{FeOH3} + 2 \cdot \alpha_{FeCO3} + 2 \cdot \alpha_{FeOH} + \alpha_{FeOH3}) + \beta \cdot$$

$$\left([CO_3^{2-}] - [H_2CO_3] + y \cdot \alpha_{FeCO3} \cdot (\alpha_{Fe} + \alpha_{FeHCO3} - \alpha_{FeOH2} - 2\alpha_{FeOH3}) - y \cdot \right.$$

$$\left.\alpha_{FeHCO3}(\alpha_{FeCO3} + \alpha_{FeOH} + \alpha_{FeOH2} + \alpha_{FeOH3})\right) \div \left((CT - y)(\alpha_{FeHCO3} + \alpha_{FeCO3})\right) +$$

$$\left.[clay{:}\, O^-] \cdot \alpha_{clayOH}\right) \qquad \text{(A28)}$$

The change in pH with respect to the reaction progress, *y*, can be described by rewriting the relationship pH = $-\log_{10}[\mathrm{H}^+]$ as:

$$\frac{dpH}{dy} = -\frac{1}{ln10} \cdot \frac{1}{[\mathrm{H}^+]} \cdot \frac{d[\mathrm{H}^+]}{dy} . \qquad \text{(A29)}$$

Combining Equations A28 and A29 yields:

$$\frac{dpH}{dx} = -\frac{1}{ln10} \cdot \left(2 \cdot \alpha_{Fe} + \alpha_{FeHCO3} + \alpha_{FeOH} - \alpha_{FeOH3} + \beta \cdot \left(\frac{0.25 - \alpha_{FeHCO3} - \alpha_{FeCO3}}{(CT-x)(\alpha_{FeHCO3} + \alpha_{FeCO3})}\right)\right) \div$$

$$\left([H^+] + [OH^-] + 2[CO_3^{2-}] + 2y \cdot \alpha_{Fe} \cdot (\alpha_{Fe} + \alpha_{FeOH} + 2 \cdot \alpha_{FeOH2} + 3 \cdot \alpha_{FeOH3}) + y \cdot \right.$$

$$\alpha_{FeHCO3} \cdot (\alpha_{FeCO3} + \alpha_{FeOH} + 2 \cdot \alpha_{FeOH2}) + y \cdot \alpha_{FeOH} \cdot (\alpha_{Fe} + \alpha_{FeOH} - \alpha_{FeOH2} - 2 \cdot$$

$$\alpha_{FeOH3}) + y \cdot \alpha_{FeOH3}(3 \cdot \alpha_{Fe} + 3 \cdot \alpha_{FeOH3} + 2 \cdot \alpha_{FeCO3} + 2 \cdot \alpha_{FeOH} + \alpha_{FeOH3}) + \beta \cdot$$

$$\left([CO_3^{2-}] - [H_2CO_3] + y \cdot \alpha_{FeCO3} \cdot (\alpha_{Fe} + \alpha_{FeHCO3} - \alpha_{FeOH2} - 2\alpha_{FeOH3}) - y \cdot \right.$$

$$\left.\alpha_{FeHCO3} \cdot (\alpha_{FeCO3} + \alpha_{FeOH} + \alpha_{FeOH2} + \alpha_{FeOH3})\right) \div \left((CT - y)(\alpha_{FeHCO3} + \alpha_{FeCO3})\right) +$$

$$\left.[clay{:}\, O^-] \cdot \alpha_{clayOH}\right) . \qquad \text{(A30)}$$

This equation then describes the evolution of the system and makes it possible to model the system pH as a function of the amount of iron reduced for circumstances with and without clay minerals.

In like manner, we calculate the evolution of carbonate saturation during iron reduction. Critical saturation, Ω_c, is expressed in Equation A14 and the change in Ω_c with respect to the reaction progress, y, assuming that $[Ca^{2+}]$ remains constant (i.e., $d[Ca^{2+}]/dy = 0$), is expressed in Equation A31.

$$\frac{1}{\Omega} \cdot \frac{d\Omega}{dy} = \frac{d[CO_3^{2-}]}{[CO_3^{2-}] \cdot dy} \qquad \text{(A31)}$$

The carbonate saturation index, SI, is simply expressed as $SI = \log_{10}\Omega_c$, and the change in SI with respect to the reaction progress, y, can be written as:

$$\frac{dSI}{dy} = \frac{1}{\ln 10} \cdot \frac{1}{\Omega} \cdot \frac{d\Omega}{dy}. \qquad \text{(A32)}$$

Combining Equations A31 and A32 yields:

$$\frac{dSI}{dy} = \frac{d[CO_3^{2-}]}{\ln 10 \cdot [CO_3^{2-}] \cdot dy}, \qquad \text{(A33)}$$

where values for $[CO_3^{2-}]$ and $d[CO_3^{2-}]/dy$ are obtained from the pH model above (Equations A23-A30). These values can be obtained under circumstances with and without clay minerals present in the system. Thus, for both circumstances we are able to predict SI as a function of the amount of iron reduced. Equations A22 and A34-A40 are used to simplify Equations A28 and A30.

$$\beta = y \cdot (-2 \cdot \alpha_{Fe} - \alpha_{FeOH} + \alpha_{FeOH3}) \cdot (\alpha_{FeHCO3} + \alpha_{FeCO3}) + y \cdot \alpha_{FeCO3} \cdot$$
$$(\alpha_{Fe} + \alpha_{FeOH} + \alpha_{FeOH2} + \alpha_{FeOH3}) - [HCO_3^-] - 2 \cdot [CO_3^{2-}] \qquad \text{(A34)}$$

$$\alpha_{Fe} = 10^{-3 \cdot pH} \div (10^{-3 \cdot pH} + [HCO_3^-] \cdot (10^{-pKb-3 \cdot pH} + 10^{-pKc-pKc2-2 \cdot pH}) +$$

$$10^{-pb1-2 \cdot pH} + 10^{-pb2-pH} + 10^{-pb3}) \quad \text{(A35)}$$

$$\alpha_{FeHCO3} = \alpha_{Fe} \cdot [HCO_3^-] \cdot 10^{-pKb} \quad \text{(A36)}$$

$$\alpha_{FeCO3} = \alpha_{Fe} \cdot [HCO_3^-] \cdot 10^{pH-pKc-pKc2} \quad \text{(A37)}$$

$$\alpha_{FeOH} = \alpha_{Fe} \cdot 10^{pH-pb1} \quad \text{(A38)}$$

$$\alpha_{FeOH2} = \alpha_{Fe} \cdot 10^{2 \cdot pH-pb2} \quad \text{(A39)}$$

$$\alpha_{FeOH3} = \alpha_{Fe} \cdot 10^{3 \cdot pH-pb3} \quad \text{(A40)}$$

Sulfate Reduction

Sulfate reduction is driven by microorganisms as they utilize sulfate as an electron acceptor and oxidize organic carbon (Equation A41; e.g., Canfield et al., 1993; Froelich et al., 1979). We model this reaction by defining the reaction progress (z) as the total amount of sulfate reduced or the sum of H_2S, HS^-, or S^{2-} species produced (Equation A42). Using the stoichiometry from Equation A41, the total carbon (CT) in the system is equal to the initial dissolved inorganic carbon (DIC_0) plus the reaction progress (z) multiplied by 2 (Equation A43).

$$2CH_2O + SO_4^{2-} \rightarrow 2HCO_3^- + HS^- + H^+ \quad \text{(A41)}$$

$$z = [SO_4^{2-}]_0 + [SO_4^{2-}] = [H_2S] + [HS^-] + [S^{2-}] \quad \text{(A42)}$$

$$CT = DIC_0 + 2z = [H_2CO_3^*] + [HCO_3^-] + [CO_3^{2-}] \quad \text{(A43)}$$

To incorporate clay minerals in our model, we account for the deprotonation (forward reaction in Equation A3) and protonation (reverse reaction in Equation A3) reactions (e.g., Avena et al., 2003; Mitchell and Soga, 2005). Charge balance dictates the net charge of the system does not change as the reaction progresses. The charged species

that undergo a change in concentration as the reaction proceeds are summed on the left side of Equation A44, while the charged species that remain constant throughout the reaction are not included.

$$\frac{d}{dz}([\mathrm{H^+}] - [\mathrm{OH^-}] - [\mathrm{HCO_3^-}] - 2[\mathrm{CO_3^{2-}}] - 2[\mathrm{SO_4^{2-}}] - [\mathrm{HS^-}] - 2[\mathrm{S^{2-}}] - [\mathrm{clay{:}\,O^-}]) = 0 \qquad \text{(A44)}$$

By adding the term [clay:O$^-$] to the charge balance equation we can account for the acid-base properties of clay minerals, and alternatively, by removing this term we are able to model the aerobic respiration reaction alone. We rearrange the charge balance equation and write it in terms of [H$^+$] and constants using equations for speciation (Equations A5-A8 and A45-A46) and mass balance (Equations A9 and A10). Subsequently, collecting the term d[H$^+$]/dz to the left side of the equation yields Equation A47.

$$\frac{[H^+][HS^-]}{[H_2S]} = K_{s1} \qquad \text{(A45)}$$

$$\frac{[H^+][S^{2-}]}{[HS^-]} = K_{s2} \qquad \text{(A46)}$$

$$\frac{1}{[\mathrm{H^+}]} \cdot \frac{d[\mathrm{H^+}]}{dz} = (2 - 2\alpha_{HCO3-} - \alpha_{HS-} - 4\alpha_{CO32-} - 2\alpha_{S2-}) \div ([H^+] + [OH^-] + [HCO_3^-](\alpha_{H2CO3} - \alpha_{CO32-}) + 2[CO_3^{2-}](2\alpha_{H2CO3} + \alpha_{HCO3-}) + z\alpha_{HS-}(\alpha_{H2S} - \alpha_{s2-}) + 2z\alpha_{S2-}(2\alpha_{H2S} + \alpha_{HS-}) + [clay{:}\,O^-] \cdot \alpha_{clayOH}) \qquad \text{(A47)}$$

The change in pH with respect to the reaction progress, z, can be described by rewriting the relationship pH = -log$_{10}$[H$^+$] as:

$$\frac{dpH}{dz} = -\frac{1}{ln10} \cdot \frac{1}{[\mathrm{H^+}]} \cdot \frac{d[\mathrm{H^+}]}{dz}. \qquad \text{(A48)}$$

Combining Equations A47 and A48 yields:

$$\frac{dpH}{dz} = -\frac{1}{ln10} \cdot (2 - 2\alpha_{HCO3-} - \alpha_{HS-} - 4\alpha_{CO32-} - 2\alpha_{S2-}) \div ([H^+] + [OH^-] + [HCO_3^-](\alpha_{H2CO3} - \alpha_{CO32-}) + 2[CO_3^{2-}](2\alpha_{H2CO3} + \alpha_{HCO3-}) + z\alpha_{HS-}(\alpha_{H2S} - \alpha_{s2-}) + 2z\alpha_{S2-}(2\alpha_{H2S} + \alpha_{HS-}) + [clay{:}O^-] \cdot \alpha_{clayOH}) \; . \quad \text{(A49)}$$

This equation then describes the evolution of the system and makes it possible to model system pH as a function of the amount of sulfate reduced for circumstances with and without clay minerals.

In like manner, we calculate the evolution of carbonate saturation during sulfate reduction. Critical saturation, Ω_c, is expressed in Equation A14 and the change in Ω_c with respect to the reaction progress, z, assuming that $[Ca^{2+}]$ remains constant (i.e., $d[Ca^{2+}]/dz = 0$), is expressed in Equation A50.

$$\frac{1}{\Omega} \cdot \frac{d\Omega}{dz} = \frac{d[CO_3^{2-}]}{[CO_3^{2-}] \cdot dz} \qquad \text{(A50)}$$

The carbonate saturation index, *SI*, is simply expressed as $SI = \log_{10}\Omega_c$, and the change in *SI* with respect to the reaction progress, z, can be written as:

$$\frac{dSI}{dz} = \frac{1}{\ln 10} \cdot \frac{1}{\Omega} \cdot \frac{d\Omega}{dz} \; . \qquad \text{(A51)}$$

Combining Equations A50 and A51 yields:

$$\frac{dSI}{dz} = \frac{d[CO_3^{2-}]}{\ln 10 \cdot [CO_3^{2-}] \cdot dz} \; , \qquad \text{(A52)}$$

where values for $[CO_3^{2-}]$ and $d[CO_3^{2-}]/dz$ are obtained from the pH model above (Equations A41-A49). For the case of sulfate reduction, the change in *SI* with respect to the change in the reaction progress, z, can be written as:

$$\frac{dSI}{dz} = \frac{1}{\ln 10 \cdot CT} + (2\alpha_{H2CO3} + \alpha_{HCO3-}) \cdot \frac{dpH}{dz} \; . \qquad \text{(A53)}$$

These values of *SI* can be obtained under circumstances with and without clay minerals present in the system. Thus, for both circumstances we are able to predict *SI* as a function of the amount of sulfate reduced. Equations A19-A22 and A54-A56 are used to simplify Equations A47 and A49.

$$\alpha_{H2S} = [H^+]^2 \div ([H^+] + K_{s1}[H^+] + K_{s1}K_{s2}) \quad \text{(A54)}$$

$$\alpha_{HS-} = K_{s1}(\alpha_{H2S} \div [H^+]) \quad \text{(A55)}$$

$$\alpha_{S2-} = K_{s2}(\alpha_{HS-} \div [H^+]) \quad \text{(A56)}$$

Hydrogenotrophic Methanogenesis

Hydrogenotrophic methanogenesis is driven by microorganisms as they utilize bicarbonate (HCO_3^-) as an electron acceptor and oxidize molecular hydrogen (H_2) (Equation A57; e.g., Froelich et al., 1979). We model this reaction by defining the reaction progress (*m*) as the total amount of methane (CH_4) produced (Equation A58). Using the stoichiometry from Equation A57, the total carbon (*CT*) in the system is equal to the initial dissolved inorganic carbon (DIC_0) minus the reaction progress (*m*) (Equation A59).

$$HCO_3^- + 4H_2 + H^+ \rightarrow CH_4 + 3H_2O \quad \text{(A57)}$$

$$m = [CH_4] \quad \text{(A58)}$$

$$CT = DIC_0 - m = [H_2CO_3^*] + [HCO_3^-] + [CO_3^{2-}] \quad \text{(A59)}$$

To incorporate clay minerals in our model, we account for the deprotonation (forward reaction in Equation A3) and protonation (reverse reaction in Equation A3) reactions of clay minerals (e.g., Avena et al., 2003; Mitchell and Soga, 2005). Charge balance dictates that the net charge of the system does not change as the reaction progresses. The

charged species that undergo a change in concentration as the reaction proceeds are summed on the left side of Equation A60, while the charged species that remain constant throughout the reaction are not included.

$$\frac{d}{dz}([\mathrm{H^+}] - [\mathrm{OH^-}] - [\mathrm{HCO_3^-}] - 2[\mathrm{CO_3^{2-}}] - [\mathrm{clay{:}O^-}]) = 0 \qquad \text{(A60)}$$

By adding the term [clay:O$^-$] to the charge balance equation we can account for the acid-base properties of clay minerals, and alternatively, by removing this term we are able to model the aerobic respiration reaction alone. We rearrange the charge balance equation and write it in terms of [H$^+$] and constants using equations for speciation (Equations A5-A8) and mass balance (Equations A9 and A10). Subsequently, collecting the term d[H$^+$]/dx to the left side of the equation yields Equation A61.

$$\frac{1}{[\mathrm{H^+}]} \cdot \frac{d[\mathrm{H^+}]}{dm} = (\alpha_{HCO3-} + 2\alpha_{CO32-}) \div ([H^+] + [OH^-] + [HCO_3^-](\alpha_{H2CO3} - \alpha_{CO32-}) + 2[CO_3^{2-}]\left(2\alpha_{H2CO3} + \alpha_{HCO3-}\right) + [clay{:}O^-] \cdot \alpha_{clayOH}\right) \qquad \text{(A61)}$$

The change in pH with respect to the reaction progress, x, can be described by rewriting the relationship pH = -log$_{10}$[H$^+$] as:

$$\frac{dpH}{dm} = -\frac{1}{ln10} \cdot \frac{1}{[\mathrm{H^+}]} \cdot \frac{d[\mathrm{H^+}]}{dm}. \qquad \text{(A62)}$$

Combining Equations A61 and A62 yields:

$$\frac{dpH}{dm} = -\frac{1}{ln10} \cdot (\alpha_{HCO3-} + 2\alpha_{CO32-}) \div ([H^+] + [OH^-] + [HCO_3^-](\alpha_{H2CO3} - \alpha_{CO32-}) + 2[CO_3^{2-}]\left(2\alpha_{H2CO3} + \alpha_{HCO3-}\right) + [clay{:}O^-] \cdot \alpha_{clayOH}\right). \qquad \text{(A63)}$$

This equation then describes the evolution of the system and makes it possible to model system pH as a function of the amount of CH_4 produced for circumstances with and without clay minerals.

In like manner, we calculate the evolution of carbonate saturation during hydrogenotrophic methanogenesis. Critical saturation, Ω_c, is expressed in Equation A14 and the change in Ω_c with respect to the reaction progress, m, assuming that $[Ca^{2+}]$ remains constant (i.e., $d[Ca^{2+}]/dm = 0$), is expressed in Equation A64.

$$\frac{1}{\Omega} \cdot \frac{d\Omega}{dm} = \frac{d[CO_3^{2-}]}{[CO_3^{2-}] \cdot dm} \qquad \text{(A64)}$$

The carbonate saturation index, SI, is simply expressed as $SI = \log_{10}\Omega_c$, and the change in SI with respect to the reaction progress, m, can be written as:

$$\frac{dSI}{dm} = \frac{1}{\ln 10} \cdot \frac{1}{\Omega} \cdot \frac{d\Omega}{dm}. \qquad \text{(A65)}$$

Combining Equations A64 and A65 yields:

$$\frac{dSI}{dm} = \frac{d[CO_3^{2-}]}{\ln 10 \cdot [CO_3^{2-}] \cdot dm}, \quad \text{(A66)}$$

where values for $[CO_3^{2-}]$ and $d[CO_3^{2-}]/dm$ are obtained from the pH model above (Equations A57-A63). For the case of hydrogenotrophic methanogenesis, the change in SI with respect to the change in the reaction progress, m, can be written as:

$$\frac{dSI}{dm} = \frac{1}{\ln 10 \cdot CT} + (2\alpha_{H2CO3} + \alpha_{HCO3-}) \cdot \frac{dpH}{dm}. \quad \text{(A67)}$$

These values of SI can be obtained under circumstances with and without clay minerals present in the system. Thus, for both circumstances we are able to predict SI as a function of the amount of CH_4 produced. Equations A19-A22 are used to simplify Equations A61 and A63.

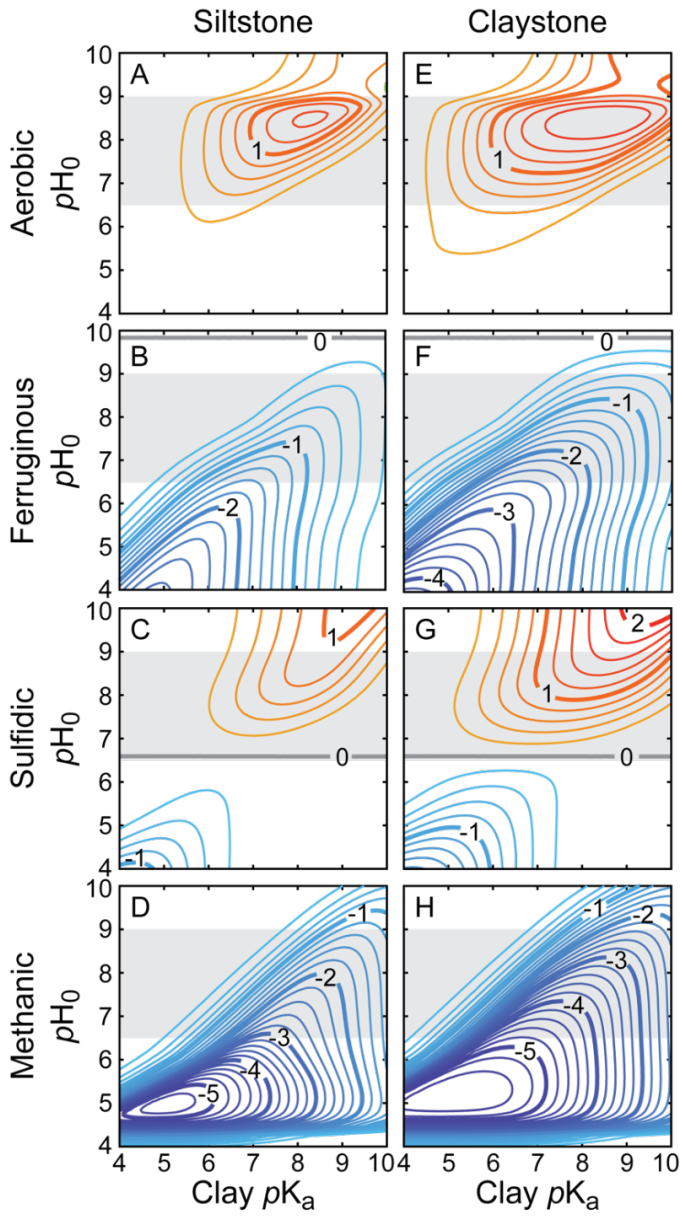

Figure A2. Effects of initial pH and clay pK_a on pore fluid evolution. Siltstone (A-D; ~10 wt.% clay minerals) and claystone (E-H; ~70% clay minerals) sediments could buffer pore fluid pH at a wide range of initial pH (pH_0) and clay mineral pK_a values under aerobic, ferruginous, sulfidic, and methanic conditions. The contour lines represent the greatest ΔpH values for a set of particular pK_a and pH_0 values used as initial conditions. The shaded areas represent the typical pore fluid pH values found in marine sediments (6.5-9; Ben-Yaakov, 1973) and clay mineral pK_a values found in nature (4-10; Duc et al., 2005). ΔpH is the difference between the pH curves with and without a clay buffer, where positive values (red) indicate increased pH and negative values (blue) indicate decreased pH.

Appendix A References

ASTM D7928-17, Standard test method for particle-size distribution (gradation) of fine-grained soils using the sedimentation (hydrometer) analysis, West Conshohocken, PA, 2017, www.astm.org.

Avena, M. J., Mariscal, M. M., and De Pauli, C. P., 2003, Proton binding at clay surfaces in water: Applied Clay Science, v. 24, p. 3-9, https://doi.org/10.1016/j.clay.2003.07.003.

Ben-Yaakov, S., 1973, pH buffering of pore water of recent anoxic marine sediments: Limnology and Oceanography, v. 18, p. 86-94, https://doi.org/10.4319/lo.1973.18.1.0086.

Boggs, S., 2009, Petrology of Sedimentary Rocks, New York, NY, Cambridge University Press, 600 p.

Canfield, D. E., Thamdrup, B., and Hansen, J. W., 1993, The anaerobic degradation of organic matter in Danish coastal sediments: Iron reduction, manganese reduction, and sulfate reduction: Geochimica et Cosmochimica Acta, v. 57, p. 3867-3883, http://dx.doi.org/10.1016/0016-7037(93)90340-3.

Davranche, M., Lacour, S., Bordas, F., and Bollinger, J.C., 2003, An easy determination of the surface chemical properties of simple and natural solids: Journal of Chemical Education, v. 80, p. 76-78, https://doi.org/10.1021/ed080p76.

Duc, M., Gaboriaud, F., and Thomas, F., 2005, Sensitivity of the acid–base properties of clays to the methods of preparation and measurement: 1. Literature review: Journal of Colloid and Interface Science, v. 289, p. 139-147, https://doi.org/10.1016/j.jcis.2005.03.060.

Flemings, P.B., Behrmann, J.H., John, C.M., and the Expedition 308 Scientists, 2006, Gulf of Mexico Hydrogeology, Proceedings of the IODP, 308: College Station, TX, Integrated Ocean Drilling Program Management International, Inc., https://doi.org/10.2204/iodp.proc.308.2006.

Froelich, P. N., Klinkhammer, G. P., Bender, M. L., Luedtke, N. A., Heath, G. R., Cullen, D., Dauphin, P., Hammond, D., Hartman, B., and Maynard, V., 1979, Early oxidation of organic matter in pelagic sediments of the eastern equatorial Atlantic: Suboxic diagenesis: Geochimica et Cosmochimica Acta, v. 43, p. 1075-1090, https://doi.org/10.1016/0016-7037(79)90095-4.

Lovley, D. R., 1991, Dissimilatory Fe(III) and Mn(IV) reduction: Microbiological Reviews, v. 55, p. 259-287.

Mitchell, J. K., and Soga, K., 2005, Fundamentals of Soil Behavior, 3rd Edition, John Wiley & Sons, Inc., 592 p.

Osipov, V.I., 2012, Density of clay minerals: Soil mechanics and foundation engineering, V. 48, p. 231-240, https://doi.org/10.1007/s11204-012-9153-0.

Reece, J.S., Flemings, P.B., and Germaine, J.T., 2013, Data report: permeability, compressibility, and microstructure of resedimented mudstone from IODP Expedition 322, Site C001, in Saito, S., Underwood, M.B., Kubo, Y., and the Expedition 322 Scientists, eds., Proceedings of the IODP, 322: Tokyo, Integrated Ocean Drilling Program Management International, Inc., https://doi.org/10.2204/iodp.proc.322.205.2013.

Stumm, W., 1992, Chemistry of the Solid-Water Interface: Processes at the Mineral-Water and Particle-Water Interface in Natural Systems, John Wiley & Sons, Inc., 448 p.

Tucker, M. E., 2001, Sedimentary Petrology, 3rd Edition, Malden, MA, Blackwell Science Ltd., 262 p.

Zeng, Z., and Tice, M. M., 2014, Promotion and nucleation of carbonate precipitation during microbial iron reduction: Geobiology, v. 12, p. 362-371, https://doi.org/10.1111/gbi.12090.

APPENDIX B

PYTHON CODE FOR CHAPTER 2 MODEL

Python Code

@author: Mike Tice and Tanner Mills

Redox profile model (daisy-chains models for aerobic respiration, iron reduction, sulfate reduction, and methanogenesis)

Slow model assumes that carbonate precipitation and dissolution are slow relative to respiration; carbonate mineral saturation index therefore varies maximally and Ca concentration is constant.
"""

```
import matplotlib.pyplot as plt
import numpy as np
from scipy.integrate import odeint
import pandas as pd

'''Definition of equilibrium constants. Select seawater or freshwater, or enter constants appropriate to your system.'''

system = 'seawater' # May be seawater or freshwater
mineral = 'calcite' # May be calcite or aragonite

if system == 'seawater':
    pKw = 14
    pKc1 = 5.9
    pKc2 = 8.9
    pKs1 = 6.9
    pKs2 = 12.9
    pKclay1 = 6.6
    pKclay2 = 8.7
    pKb = -2.0 # Complexation constant for FeHCO3+
    pKc = -2.83 # Complexation constant for FeCO3
    pb1 = 9.4 # Beta for FeOH+
    pb2 = 20.5 # Beta for Fe(OH)2
    pb3 = 29.0 # Beta for Fe(OH)3-
    if mineral == 'aragonite': pKsp = 6.19
    elif mineral == 'calcite': pKsp = 8.22
```

```
elif system == 'freshwater':
    pKw = 14
    pKc1 = 6.3
    pKc2 = 10.3
    pKs1 = 6.9
    pKs2 = 12.9
    pKb = -2.0 # Complexation constant for FeHCO3+
    pKc = -2.83 # Complexation constant for FeCO3
    pb1 = 9.4 # Beta for FeOH+
    pb2 = 20.5 # Beta for Fe(OH)2
    pb3 = 29.0 # Beta for Fe(OH)3-
    if mineral == 'aragonite': pKsp = 6.19
    elif mineral == 'calcite': pKsp = 8.22

'''Definition of functions returning chemical species and speciation fractions'''

def ten(x): return np.exp(x*np.log(10))

def H(pH): return ten(-pH)

def OH(pH): return ten(pH - pKw)

def aH2CO3(pH):
    alpha = 1/(1 + ten(pH - pKc1) + ten(2*pH - pKc1 - pKc2))
    return alpha

def aHCO3(pH):
    alpha = ten(pH - pKc1)*aH2CO3(pH)
    return alpha

def aCO3(pH):
    alpha = ten(pH - pKc2)*aHCO3(pH)
    return alpha

def aClayOH1(pH):
    alpha = ten(pKclay1-pH)/(ten(pKclay1-pH)+1)
    return alpha

def aClayOH2(pH):
    alpha = ten(pKclay2-pH)/(ten(pKclay2-pH)+1)
    return alpha
```

```
def aH2S(pH):
    alpha = 1/(1 + ten(pH - pKs1) + ten(2*pH - pKs1 - pKs2))
    return alpha

def aHS(pH):
    alpha = ten(pH - pKs1)*aH2S(pH)
    return alpha

def aS(pH):
    alpha = ten(pH - pKs2)*aHS(pH)
    return alpha

def Ab(pH):
    coeff = (ten(pKc1 - pH) + 1 + ten(pH - pKc2))*(ten(-pKb - 3*pH) + ten(-pKc - pKc2 -
2*pH))
    return coeff

def Bb(pH, CT, FeT):
    coeff = (FeT - CT)*(ten(-pKb - 3*pH) + ten(-pKc2 - pKc - 2*pH))
    coeff += (ten(-3*pH) + ten(-pb1 - 2*pH) + ten(-pb2 - pH) + ten(-pb3))*(ten(pKc1 -
pH) + 1 + ten(pH - pKc2))
    return coeff

def Cb(pH, CT):
    coeff = -CT*(ten(-3*pH) + ten(-pb1 - 2*pH) + ten(-pb2 - pH) + ten(-pb3))
    return coeff

def HCO3(pH, CT, FeT=0):
    if FeT > 0:
        A, B, C = Ab(pH), Bb(pH, CT, FeT), Cb(pH, CT)
        conc = (-B + np.sqrt((B**2) - 4*A*C))/(2*A)
        return conc
    else:
        return CT*aHCO3(pH)

def H2CO3(pH, CT, FeT=0): return HCO3(pH, CT, FeT)*ten(pKc1 - pH)

def CO3(pH, CT, FeT=0): return HCO3(pH, CT, FeT)*ten(pH - pKc2)

def H2S(pH, ST): return ST*aH2S(pH)

def HS(pH, ST): return ST*aHS(pH)

def S(pH, ST): return ST*aS(pH)
```

```
def ClayO1(pH): return Clay01/(ten(pKclay1-pH)+1)

def ClayOH1(pH): return ClayO1(pH)*ten(pKclay1-pH)

def ClayO2(pH): return Clay02/(ten(pKclay2-pH)+1)

def ClayOH2(pH): return ClayO2(pH)*ten(pKclay2-pH)

def aFe(pH, CT, FeT):
    alpha = ten(-3*pH)/(ten(-3*pH) + (ten(-pKb - 3*pH) + ten(-pKc - pKc2 -
    2*pH))*HCO3(pH, CT, FeT) + ten(-pb1 - 2*pH) + ten(-pb2 - pH) + ten(-pb3))
    return alpha

def aFeHCO3(pH, CT, FeT):
    alpha = aFe(pH, CT, FeT)*HCO3(pH, CT, FeT)*ten(-pKb)
    return alpha

def aFeCO3(pH, CT, FeT):
    alpha = aFe(pH, CT, FeT)*HCO3(pH, CT, FeT)*ten(pH - pKc - pKc2)
    return alpha

def aFeOH(pH, CT, FeT):
    alpha = aFe(pH, CT, FeT)*ten(pH - pb1)
    return alpha

def aFeOH2(pH, CT, FeT):
    alpha = aFe(pH, CT, FeT)*ten(2*pH - pb2)
    return alpha

def aFeOH3(pH, CT, FeT):
    alpha = aFe(pH, CT, FeT)*ten(3*pH - pb3)
    return alpha

def Beta(pH, CT, FeT):
    res = FeT*(-2*aFe(pH, CT, FeT) - aFeOH(pH, CT, FeT) + aFeOH3(pH, CT,
    FeT))*(aFeHCO3(pH, CT, FeT) + aFeCO3(pH, CT, FeT))
    res += FeT*aFeCO3(pH, CT, FeT)*(aFe(pH, CT, FeT) + aFeOH(pH, CT, FeT) +
    aFeOH2(pH, CT, FeT) + aFeOH3(pH, CT, FeT))
    res += -HCO3(pH, CT, FeT) - 2*CO3(pH, CT, FeT)
    return res
```

```
def Gamma(pH, Ca, CT, FeT):
    res = 2*Ca + 2*FeT*aFe(pH, CT, FeT)*(aFeCO3(pH, CT, FeT) + aFeOH(pH, CT,
    FeT) + 2*aFeOH2(pH, CT, FeT) + 3*aFeOH3(pH, CT, FeT))
    res += FeT*aFeHCO3(pH, CT, FeT)*(aFeCO3(pH, CT, FeT) + aFeOH(pH, CT, FeT)
    + 2*aFeOH2(pH, CT, FeT) + 3*aFeOH3(pH, CT, FeT))
    res += -FeT*aFeOH(pH, CT, FeT)*(1 - aFeCO3(pH, CT, FeT) -aFeOH(pH, CT, FeT)
    -2*aFeOH2(pH, CT, FeT) - 3*aFeOH3(pH, CT, FeT))
    res += FeT*aFeOH3(pH, CT, FeT)*(3 - aFeCO3(pH, CT, FeT) -aFeOH(pH, CT, FeT)
    -2*aFeOH2(pH, CT, FeT) - 3*aFeOH3(pH, CT, FeT))
    res += 2*CO3(pH, CT, FeT) + H(pH) + OH(pH)
    return res

def Delta(pH, Ca, CT, FeT):
    res = -2*Ca -2*FeT*aFe(pH, CT, FeT)*(aFeHCO3(pH, CT, FeT) + aFeCO3(pH, CT,
    FeT))
    res += FeT*aFeHCO3(pH, CT, FeT)*(1 - aFeHCO3(pH, CT, FeT) - aFeCO3(pH, CT,
    FeT))
    res += -FeT*(aFeOH(pH, CT, FeT) - aFeOH3(pH, CT, FeT))*(aFeHCO3(pH, CT,
    FeT) + aFeCO3(pH, CT, FeT))
    res += -HCO3(pH, CT, FeT) - 2*CO3(pH, CT, FeT)
    return res

def Epsilon(pH, Ca, CT, FeT):
    res = Ca + FeT*aFeCO3(pH, CT, FeT) + CO3(pH, CT, FeT) - H2CO3(pH, CT, FeT)
    res += -FeT*(aFeHCO3(pH, CT, FeT) + aFeCO3(pH, CT, FeT))
     *(aFeCO3(pH, CT, FeT) + aFeOH(pH, CT, FeT) + 2*aFeOH2(pH, CT, FeT) +
     3*aFeOH3(pH, CT, FeT))
    return res

def Zeta(pH, Ca, CT, FeT):
    res = FeT*(aFeHCO3(pH, CT, FeT) + aFeCO3(pH, CT, FeT))*(1 - aFeHCO3(pH,
    CT, FeT) - aFeCO3(pH, CT, FeT))
    res += H2CO3(pH, CT, FeT) + HCO3(pH, CT, FeT) + CO3(pH, CT, FeT) + Ca
    return res

'''Definition of useful constants'''

M = 1
mM = 0.001*M
uM = 0.001*mM
```

```
'''Set boundary conditions'''

zone = 'aerobic' # Can be aerobic, ferruginous, sulfidic, or methanic
pH0 = 8 # Initial pH
DIC0 = 2.2*mM # Initial dissolved inorganic carbon
Clay01 = 10*mM #  Initial clay concentration, i.e., Clay0 = [clay:O-]+[clay:OH]
Clay02 = 10*mM
O2_consumed = 1*mM # Total oxygen respired at end of reaction
Fe_consumed = 2*mM # Total iron respired at end of reaction
SO4_consumed = 15*mM # Total sulfate respired at end of reaction
CH4_produced = 5*mM # Total methane produced at end of reaction
SI0 = 0.3 # Initial carbonate mineral saturation (for no precipitation model)
sp = 0 # Fraction of sulfate used to make pyrite

'''Calculating pH and SI'''

if (zone=='aerobic')==False :
    O2_consumed = 0*mM
    if (zone=='ferruginous')==False : Fe_consumed = 0*mM

N = 501
Ca0 = ten(-pKsp)/CO3(pH0, DIC0, 0)
f0 = [pH0, SI0, DIC0]
if zone=='aerobic' : x = np.linspace(0, O2_consumed, N)
else: x = [0]

def aer(y, x):
    pH, SI, CT = y
    F = -aHCO3(pH) - 2*aCO3(pH)
    beta = H(pH) + OH(pH) + HCO3(pH, CT)*(aH2CO3(pH) - aCO3(pH))
    + 2*CO3(pH, CT)*(2*aH2CO3(pH) + aHCO3(pH))
    beta += ClayO1(pH)*aClayOH1(pH)
    beta += ClayO2(pH)*aClayOH2(pH)
    dpHdx = F/(beta*np.log(10))
    dSIdx = (2*aH2CO3(pH) + aHCO3(pH))*dpHdx + 1/(CT*np.log(10))
    return [dpHdx, dSIdx, 1]

if zone=='aerobic' :
    oxygen = odeint(aer, f0, x)
else: oxygen = f0
```

```
if zone=='aerobic' :
   pHslow, SI0, DICslow = oxygen[-1, 0], oxygen[-1, 1], oxygen[-1, 2]
else:
   pHslow, SI0, DICslow = pH0, SI0, DIC0
f0 = [pHslow, SI0, DICslow, 0]
if (zone=='aerobic') | (zone=='ferruginous') : y = np.linspace(0, Fe_consumed, N)
else: y = [0]

def fered(y, x):
   pH, SI, CT, FeT = y
   F = 2*aFe(pH, CT, FeT) + aFeHCO3(pH, CT, FeT)
   + aFeOH(pH, CT, FeT) - aFeOH3(pH, CT, FeT)
   F += Beta(pH, CT, FeT)*(0.25 - aFeHCO3(pH, CT, FeT) - aFeCO3(pH, CT,
   FeT))/(CT - FeT*(aFeHCO3(pH, CT, FeT) + aFeCO3(pH, CT, FeT)))
   beta = H(pH) + OH(pH) + 2*CO3(pH, CT, FeT)
   beta += 2*FeT*aFe(pH, CT, FeT)*(aFeCO3(pH, CT, FeT) + aFeOH(pH, CT, FeT) +
   2*aFeOH2(pH, CT, FeT) + 3*aFeOH3(pH, CT, FeT))
   beta += FeT*aFeHCO3(pH, CT, FeT)*(aFeCO3(pH, CT, FeT)
   + aFeOH(pH, CT, FeT) + 2*aFeOH2(pH, CT, FeT))
   beta += FeT*aFeOH(pH, CT, FeT)*(aFe(pH, CT, FeT)
   + aFeOH(pH, CT, FeT) - aFeOH2(pH, CT, FeT) - 2*aFeOH3(pH, CT, FeT))
   beta += FeT*aFeOH3(pH, CT, FeT)*(3*aFe(pH, CT, FeT) + 3*aFeOH3(pH, CT,
   FeT) + 2*aFeCO3(pH, CT, FeT) + 2*aFeOH(pH, CT, FeT) + aFeOH3(pH, CT, FeT))
   beta += Beta(pH, CT, FeT)*(CO3(pH, CT, FeT) - H2CO3(pH, CT, FeT) +
   FeT*aFeCO3(pH, CT, FeT)*(aFe(pH, CT, FeT) + aFeHCO3(pH, CT, FeT) -
   aFeOH2(pH, CT, FeT) - 2*aFeOH3(pH, CT, FeT)) - FeT*aFeHCO3(pH, CT,
   FeT)*(aFeCO3(pH, CT, FeT) + aFeOH(pH, CT, FeT) + aFeOH2(pH, CT, FeT) +
   aFeOH3(pH, CT, FeT)))/(CT - FeT*(aFeHCO3(pH, CT, FeT) + aFeCO3(pH, CT,
   FeT)))
   beta += ClayO1(pH)*aClayOH1(pH)
   beta += ClayO2(pH)*aClayOH2(pH)
   dpHdx = F/(beta*np.log(10))
   dSIdx = 0
   return [dpHdx, dSIdx, 0.25, 1]

if (zone=='aerobic') | (zone=='ferruginous') :
   iron = odeint(fered, f0, y)
   for i in range(0, N): iron[i, 1] = np.log10(CO3(iron[i, 0], iron[i, 2],
   iron[i, 3])/CO3(iron[0, 0], iron[0, 2], iron[0, 3])) + SI0
else: iron = f0
```

```
if (zone=='aerobic') | (zone=='ferruginous') :
   pHslow, SI0, DICslow = iron[-1, 0], iron[-1, 1], iron[-1, 2]
else:
   pHslow, SI0, DICslow = pH0, SI0, DIC0

f0 = [pHslow, SI0, DICslow]
if (zone=='aerobic') | (zone=='ferruginous') | (zone=='sulfidic') :
z = np.linspace(0, SO4_consumed, N)
else: z = [0]

def sulf(y, x):
   pH, SI, CT = y
   F = -(2 - 0.125*sp)*aHCO3(pH) - 2*(2 - 0.125*sp)*aCO3(pH)
   - (1 - sp)*aHS(pH) - 2*(1 - sp)*aS(pH) + 2
   beta = H(pH) + OH(pH) + HCO3(pH, CT)*(aH2CO3(pH) - aCO3(pH))
   + 2*CO3(pH, CT)*(2*aH2CO3(pH) + aHCO3(pH)) + HS(pH, x)*(aH2S(pH)
   - aS(pH)) + 2*S(pH, x)*(2*aH2S(pH) + aHS(pH))
   beta += ClayO1(pH)*aClayOH1(pH)
   beta += ClayO2(pH)*aClayOH2(pH)
   dpHdx = F/(beta*np.log(10))
   dSIdx = (2*aH2CO3(pH) + aHCO3(pH))*dpHdx + (2 - 0.125*sp)/(CT*np.log(10))
   return [dpHdx, dSIdx, 2]

if (zone=='aerobic') | (zone=='ferruginous') | (zone=='sulfidic') :
sulfate = odeint(sulf, f0, z)
else: sulfate = f0

if (zone=='aerobic') | (zone=='ferruginous') | (zone=='sulfidic') :
   pHslow, SI0, DICslow = sulfate[-1, 0], sulfate[-1, 1], sulfate[-1, 2]
else:
   pHslow, SI0, DICslow = pH0, SI0, DIC0

f0 = [pHslow, SI0, DICslow]

if (zone=='aerobic') | (zone=='ferruginous') | (zone=='sulfidic') | (zone=='methanic') :
m = np.linspace(0, CH4_produced, N)
else: m = [0]
```

```
def meth(y, x):
    pH, SI, CT = y
    F = aHCO3(pH) + 2*aCO3(pH)
    beta = H(pH) + OH(pH) + HCO3(pH, CT)*(aH2CO3(pH) - aCO3(pH))
    beta += 2*CO3(pH, CT)*(2*aH2CO3(pH) + aHCO3(pH))
    beta += ClayO1(pH)*aClayOH1(pH)
    beta += ClayO2(pH)*aClayOH2(pH)
    dpHdx = F/(beta*np.log(10))
    dSIdx = (2*aH2CO3(pH) + aHCO3(pH))*dpHdx + 1/(CT*np.log(10))
    return [dpHdx, dSIdx, -1]

methanic = odeint(meth, f0, m)
```

APPENDIX C

SEDIMENT SAMPLE COLLECTION

Ursa Sediment

Table C1 Stratigraphic locations and weights (kg) of sediments used to prepare the Ursa sediment, which were collected from Integrated Ocean Drilling Program Expedition 308 cores at Site U1324 Hole B. This site is located at 28d4.785'N, 89d8.344'W and under a water depth of 1056.8 m.

Core	Work Section	Interval (cm)	Depth below sea floor (m)	Weight (kg)
2H	3W	1-11	6.81-6.91	0.073
2H	4W	102-113	9.32-9.43	0.123
2H	5W	11-18	9.91-9.98	0.080
2H	6W	92-102	12.22-12.32	0.193
4H	3W	22-30	26.02-26.10	0.192
4H	3W	30-38	26.10-26.18	0.195
4H	4W	76-83	28.06-28.13	0.164
4H	6W	39-49	30.69-30.79	0.216
62X	3W	29-33	496.27-496.31	0.097
62X	3W	107-117	497.05-497.15	0.231
62X	4W	6-9	497.54-497.57	0.030
62X	4W	25-30	497.73-497.78	0.101
62X	4W	97-103	498.45-498.51	0.116
62X	5W	23-29	499.21-499.27	0.136
62X	5W	105-108	500.03-500.06	0.030
62X	5W	133-136	500.31-500.34	0.058
Total Weight				2.035

Brazos-Trinity Sediment

Table C2 Stratigraphic locations and weights (kg) of sediments used to prepare the Brazos-Trinity sediment, which were collected from Integrated Ocean Drilling Program Expedition 308 cores at Site U1319 Hole A. This site is located at 27d15.975'N, 94d24.191'W and under a water depth of 1429.6 m.

Core	Work Section	Interval (cm)	Depth below sea floor (m)	Weight (kg)
2H	1W	77-84	5.27-5.34	0.113
2H	1W	89-100	5.39-5.5	0.148
2H	1W	115-120	5.65-5.70	0.071
2H	2W	66-75	6.66-6.75	0.077
2H	2W	127-136	7.27-7.36	0.157
2H	3W	63-74	8.13-8.24	0.169
2H	3W	88-99	8.38-8.49	0.149
2H	3W	114-124	8.64-8.74	0.131
2H	3W	127-140	8.77-8.90	0.207
2H	4W	115-125	10.15-10.25	0.109
2H	4W	125-140	10.25-10.40	0.153
2H	5W	42-51	10.92-11.01	0.193
2H	6W	78-85	12.78-12.85	0.100
2H	7W	46-57	13.96-14.07	0.117
Total Weight				1.894